Electronic properties of microstructured surfaces:
Photoemission for pulsed electron beams in a microdiode; and pressure effects on resistance in silicon nanowires

Hákon Örn Árnason

January 26, 2023

Thesis Committee:

Ágúst Valfells, Supervisor
Professor, Reykjavík University, Iceland

Halldór G. Svavarsson, Co-supervisor
Professor, Reykjavík University, Iceland

Kristján Leósson, Associate supervisor
Chief Scientific Officer, DTE, Iceland

Einar Örn Sveinbjörnsson, Examiner
Professor, University of Iceland, Iceland

Electronic properties of microstructured surfaces: Photoemission for pulsed electron beams in a microdiode; and pressure effects on resistance in silicon nanowires

Short title: Electronic properties of microstructured surfaces

 SVANSPRENT

I dedicate this to lost knowledge.

Contents

vi

List of Figures

List of Publications

[1] H. Ö. Árnason, K. Torfason, A. Manolescu, and Á. Valfells, "Simulation of short pulse photoemission in a micro-diode with implications for optimal beam brightness," Jan. 2023, arXiv:2301.06123 [physics]. DOI: 10 . 48550 / arXiv.2301.06123.

[2] M. T. Sultan, H. Ö. Árnason, M. Kateb, A. Manolescu, H. G. Svavarsson, and Á. Valfells, "Enhanced photoemission from surface modulated GaAs:Ge," en, *Nano Select*, vol. 2, no. 12, nano.202100012, May 2021, ISSN: 2688-4011, 2688-4011. DOI: 10.1002/nano.202100012.

[3] M. T. Sultan, H. Ö. Árnason, S. Ingvarsson, *et al.*, "Facile formation of self-assembled Ga droplets on GaAs (001) substrate," en, in *2021 International Semiconductor Conference (CAS)*, Romania: IEEE, Oct. 2021, pp. 35–38, ISBN: 978-1-66543-571-0. DOI: 10.1109/CAS52836.2021.9604129.

[4] E. Fakhri, R. Plugaru, M. T. Sultan, *et al.*, "Piezoresistance Characterization of Silicon Nanowires in Uniaxial and Isostatic Pressure Variation," en, *Sensors*, vol. 22, no. 17, p. 6340, Aug. 2022, ISSN: 1424-8220. DOI: 10.3390/s22176340.

[5] R. Plugaru, E. Fakhri, C. Romanitan, *et al.*, *Structure and electrical behavior of silicon nanowires prepared by MACE process*, en, Oct. 2022. DOI: 10.1016/j.surfin.2022.102167.

List of Symbols

Symbol	Description	Value/Units
A_Ω	Cross-sectional area	m^2
Br	Brightness	$A\,m^{-2}\,rad^{-2}$
D	Diode gap distance	m
ΔQ	Total emitted charge	C
ΔE	Total absorbed energy	eV
Δt	Time step	s
E	Photon energy	eV
E_K	Kinetic energy	eV
E_F	Fermi energy level	eV
E_{Vac}	Vacuum energy	eV
ε_0	Vacuum Permittivity	$8.854 \times 10^{-12}\,F\,m$
ϵ	Emittance	m rad
F	Force	N
F_λ	Scattering factor	
G	Geometric constant (Child-Langmuir)	
h	Planck's constant	$4.135 \times 10^{-15}\,eV\,Hz^{-1}$
$\hbar$	Reduced Planck's constant	$6.582 \times 10^{-16}\,eV\,s$
η	Geometric factor (Brightness)	
I	Current	A
I_λ	Laser intensity	$W\,m^{-2}$
J	Current density	$A\,m^{-2}$
J_{crit}	Critical injection current density	$A\,m^{-2}$
l	Characteristic length	m
l_Ω	Length of resistor	m
L	Side length of a square emitter	m
m_e	Mass of electron	$9.11 \times 10^{-31}\,kg$
N_e	Number of electrons	#
N_p	Number of photons	#
ν	Photon frequency	Hz
p_1	Point on emitter	m
$p_{1\alpha}$	Point above emitter	m
$P(\hbar\omega)$	Emission factor	
q_e	Charge of electron	$1.601 \times 10^{-19}\,C$

q_{Ar}	Mass flow of Argon	sccm
Q	Charge	C
QE	Quantum efficiency	%
r	Electron location	m
R	Radius of emitter	m
R_Ω	Resistance	Ω
$R(\omega)$	Reflectivity	
ρ	Charge density	$C\,m^{-3}$
ρ_Ω	Electrical resistivity	$\Omega\,m$
σ	Surface charge density	$C\,m^{-2}$
σ_N	Pulse width in time steps	s
σ_E	Standard deviation of photon energy	eV
τ_p	Pulse width	s
τ_n	Normalized pulse width traverse time	
τ_v	Single electron traverse time	s
τ_{pulse}	Pulse of constant ejection current	s
ϕ	Potential	V
υ	Velocity	$m\,s^{-1}$
υ_z	Velocity normal to emitter	$m\,s^{-1}$
V	Electrostatic potential	V
W_e	Work function (of emitter)	eV
x	Position	m
x'	Deviation angle at position x	rad
X_{CL}	Normalized pulse length (Capacitor model)	
Z_c	Elevation of the center of charge	m
ω	Angular frequency	$rad\,s^{-1}$

Acronyms

AFM Atomic Force Microscope.

CFA Conventional Furnace Annealing.

EDX Electron Dispersive X-ray spectroscopy.

LED Light-Emitting Diodes.

MACE Metal-Assisted Chemical Etching.

MD Molecular Dynamics.

NEA Negative Electron Affinity.

PE PhotoEmission.

QCL Quantum Cascade Laser.

RTA Rapid Thermal Annealing.

SEM Scanning Electron Microscope.

SiNW Silicon NanoWire.

SSD Solid-State Device.

UV Ultra-Violet.

VED Vacuum Electronic Device.

Electronic properties of microstructured surfaces:
Photoemission for pulsed electron beams in a microdiode;
and pressure effects on resistance in silicon nanowires

Hákon Örn Árnason

January 18, 2023

Abstract

Numerical simulations done at the Nanophysics Center at Reykjavík University indicate that under constant illumination from a sufficiently energetic monochromatic light source, a space-charge limited photoemission can cause current modulation in a vacuum microdiode. The period of this modulation can be tuned by the potential applied to the diode, and is comparable to the transit time of electrons across the diode gap that can be as small as hundreds of femtoseconds. This thesis presents work on gallium-arsenide-germanium photocathodes that were fabricated and tested as a possible component for such a tunable microdiode oscillator.

A second topic of this thesis is the investigation of photoemission in microdiodes from laser pulses that are shorter than the characteristic transit time of the diode. This was done using a molecular dynamics code developed at RU. The transition from source-limited emission to space-charge limited emission is studied and compared to commonly used models. It is also shown how to obtain optimal brightness for such an electron pulse, an important issue for time resolved electron microscopy, free-electron lasers and other applications.

Lastly, random pattern silicon nanowires were fabricated and studied with regard to piezoresistance, with pressure-sensing applications in mind. They were found to exhibit resistance-dependant behavior both under isostatic and uniaxial pressure.

Acknowledgments

Journey's End

In western lands beneath the Sun
The flowers may rise in Spring,
The trees may bud, the waters run,
The merry finches sing.
Or there maybe 'tis cloudless night,
And swaying branches bear
The Elven-stars as jewels white
Amid their branching hair.

Though here at journey's end I lie
In darkness buried deep,
Beyond all towers strong and high,
Beyond all mountains steep,
Above all shadows rides the Sun
And Stars for ever dwell:
I will not say the Day is done,
Nor bid the Stars farewell.

- J.R.R.Tolkien [6]

xvi

As I am closing this chapter of my life and starting the next one there are a few thanks that need to put to paper for proper closure. I am indebted to so many people that have been with me in this chapter that lasted more then four years, too many to count here in full, so this list is in no specific order.

I would like to thank my supervisors, Ágúst Valfells, who was always ready to talk science and ideas even if taking on the mantle of Dean at the start of my project, and Sensei Halldór G. Svavarsson for keeping me mentally and physically sharp throughout the whole ordeal. To the main driving force in the group, Andrei Manolescu, I am grateful for his guidance and inspiring optimism in research, this work would not have come to fruition without him. The department office deserves a praise, and especially Sigrún Þorgeirsdóttir for moving mountains of paper and cutting through the forrest of red tape, always with a smile and laughter.

My fellow PhD and Postdoc travelers, Elham A. Fakhri, Hákon V. Haraldsson, Kristinn Torfason, and M. Taha Sultan, in cooperation and company, who made this journey a success. Not forgetting the stimulating theoretical discussions with Kristján Ó. Klausen, Þorsteinn Hanning K., and Brynjar I. Óðinsson, that were a welcome break and kept this interesting and enjoyable through out the whole time.

Last but not least, my loving family for supporting me throughout this whole chapter, for their endless patience, help and encouragement, my mother Súsanna Jónsdóttir & my fathers Árni Kr. Einarsson, Gylfi Sigurðsson, & Ómar Ellertsson, my wonderful aunt Gyða Jónsdóttir, as well as Elísabet Stefánsdóttir, Úlfhéðinn Ullur Jónþórsson, and of course Skaði Hákonardóttir my daughter, who has been waiting impatiently for her father to finish so she can get all the attention she deserves.

The untold secret is that all this started with good wine on summer solstice with Jón Ásgeir Einarsson, but that is a story for another time.

Chapter 1

Introduction

This thesis is based on three different research projects, with a common theme being nanostructured surfaces of metals and semiconductors. Two of the projects are related to high-frequency (towards THz) pulsed photoemitted electrons from nanostructured metallic/semiconducting surfaces, while the third one is focused on pressure sensing based on piezoresistance of silicon nanowires (SiNW). With respect to this, the thesis is divided into three distinct main subjects.

The first subject, in chapter 3, is molecular dynamics simulations of Gaussian pulsed photoemission in a microdiode, investigating the effects of space-charge on the magnitude and coherency of the pulsed electron beam using metrics such as current and brightness. This work is motivated by interest in generation of moderately large current pulses with periods ranging from tens of femtoseconds to picoseconds. The effects of size of the emitting area, laser intensity, pulse-width, and voltage applied to the diode are studied and compared to existing models for current and charge. An optimal operating point with regard to brightness is identified and found to be when the total charge in the beam pulse is roughly 40 % of the critical charge for virtual cathode formation.

The second subject, in chapter 4, is heat treatment of GaAs with a thin film of Ge through both conventional furnace annealing (CFA) and rapid thermal annealing (RTA) with a reported enhancement of photoemission characteristics. A low-power commercial ultraviolet light-emitting diode is used to induce photoemission in the nanostructured material. The responsible nanostructures, chemical composition and the ultimate effect on photoemission properties are explored. This work is part of a larger study looking at spontaneous formation of space-charge driven oscillations at THz frequency in microdiodes. The motivation was to find inexpensive photoemitters that can produce sufficient current over comparatively long time, to

generate the predicted space-charge oscillation, without damaging the cathode.

The third subject, in chapter 5, is piezoresistance in arrays of silicon nanowires (SiNW). While the effect is neither unknown nor new, there is a distinct lack of research on the effects of isostatic pressure change on arrays of wires. With reference to surface effects and electrical conduction, the emphasis is put on measuring the change in characteristics with regards to vacuum level and pressure higher than atmospheric. This is followed by depositing electrodes and measuring the electrical characteristics in both vacuum and overpressure conditions. Starting with sample preparation using a metal-assisted chemical etching (MACE) method, creating SiNW forests or bundles in single-crystalline Si wafers.

Terahertz radiation and picosecond current pulses.
Terahertz (THz) radiation is an active field of research with applications in security screenings, molecular spectroscopy, medicine, deep-space research and communications like sixth generation mobile system to name a few examples [7]–[17] The motivation behind this work is a creation of vacuum microdiode that would utilize photoemission to generate THz modulated beams of electrons. The term Terahertz radiation refers to electromagnetic waves of frequency from 0.3 THz to 3 THz, as defined by the International Telecommunication Union. The radiation designation refers to the wavelength that is from 1 mm to 0.1 mm, which places it in a transition region between microwaves and far infrared. This region has been called the "terahertz gap" due to problems and limitations with technology that generates and manipulates this frequency [11].

Developing a practical table-top device that operates at room temperature, producing THz radiation of sufficient power is the main goal, with several viable approaches. The recent quantum cascade lasers (QCL), an optical source, capable of sourcing watts of power in the THz range are still very limited by their nature. Those that operate at temperatures above 300 K can only produce higher than 15 THz, while the lower frequencies produced by QCLs having to be cryogenically or thermoelectrically cooled [7], [14], [18].

Vacuum microelectronic devices (VED) are capable of operating in the THz regime [13]. The inherent superiority of VED to solid-state devices (SSD) at producing high-power, high frequency radiation efficiently, indicates a direction where exploration should be fruitful [19], [20]. The primary obstruction for making such devices is the size and cost as high power VED are both extremely large and expensive. With advances in nanoscale manufacturing methods, the possibility of compact VED THz source superior to those of QCL and SSDs is becoming more realistic [11], [13], [20]–[24].

Advantages of using photoemission in VED are the ease of creating short pulses of electrons with photoinjection, reaching space-charge limiting conditions and driving the maximum current density higher than the critical current density [25]. This can

be used to create transient behavior in a microdiode where a virtual cathode is formed and oscillates with the frequency of electron transit time [26].

Piezoresistance

Piezoresistivity, it is a well-known effect in silicon and even more so in p-doped SiNWs [27]–[29]. It has been debated from where the effect originates in SiNW, and it has been referred to as anomalous piezoresistance [30]. The effect has been attributed to quantum confinement effects, surface charge effects, strain-induced bandgap shift, and even changes to the charge carrier effective mass [31]–[36]. The controversy has been analyzed by Rowe [37] in order to quantify the effect in silicon.

Contemporary studies have focused on the effects of gas types while applying directional pressure on silicon nanowires and ignored the response under isostatic pressure change [34], [38]. This work reports on piezoresistivity in SiNW obtained by MACE, under isostatic load in a vacuum chamber.

Chapter 2

Theory

In 1887, Heinrich Hertz was working on experiments with electromagnetic waves. One curious byproduct from one of the experiments, involving a Tesla transformer creating a spark in a gap caused a premature fire of spark in a second gap close by. His investigations concluded that light from the main spark initiated the spark in the second gap. This phenomenon was explored further by his assistant, Philipp Lenard, earning him a Nobel prize in 1905. The experiment was expanded with a theory by Einstein, using Planck's theory of light, in a famous paper in 1905 and earned him a Nobel prize in 1921 [39].

About the same time, 1903, Richardson and Thomson were working on thermal emission which laid the groundwork for a more complete theory of electron emission [40], [41]. Starting with Child and Langmuir in 1913, formulating the space-charge limitation on electron emission, with Langmuir continuously developing the theory with Blodgett for the next decade [42]–[44] Then in 1928, Fowler and Nordheim working with Sommerfelds theory on metals worked out both the separate experimental basis for field and photoemission [45]–[47] This work yielded significant results in the following two decades when DuBridge and Roehr demonstrated through experiments the energies required in thermal and photoemission [48]–[52]. The complete work by DuBridge, Hergenrother and Roehr on the effect of temperature on energies and total yield of electrons, resulted in a definition of quantum efficiency, which is a very important parameter for photodetectors [53], [54].

There are five distinct electron emission modes; thermal emission, field emission, photoemission, secondary electron emission, and space-charge limited emission. The thermal emission mode originates from heating, field emission from tunneling and high electric fields, photoemission from high energy photons, secondary electrons as primary electrons kick others around them out, and last but not least, space-charge limited emission where electrons start hindering those coming behind them.
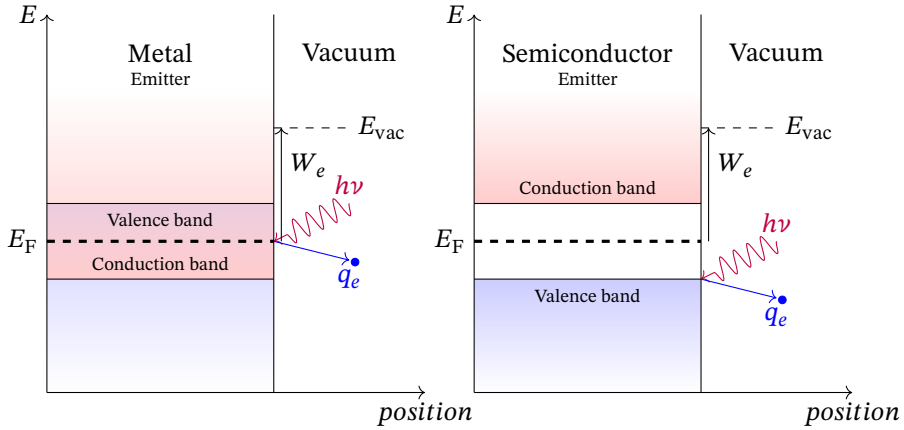
Figure 2.1: Work function (W_e) is a surface property of the material. Photoemission ejects electrons from the Fermi level (E_F) in metals, however, in semiconductors it can be from the top of the valence band.

2.1 Work function

The work function is a property of the surface of the material, indicating the minimum energy required to eject an electron from the surface. The work function is comprised of the electron affinity of the material and its Fermi-level. Since it is a surface property, it can be affected both by surface treatment and doping. The former does affect the electron affinity while the latter does affect the Fermi level. The work function, electron affinity, vacuum energy and ionization energy can be considered as surface properties. At the same time, the Fermi level, conduction band minimum, valence band maximum, and gap-energy are rather material properties Figure 2.1 [55]. These properties can be affected by thermal treatments and doping levels. The work function for a given material is

$$W_e = E_{\text{vac}} - E_F \,, \tag{2.1}$$

where E_{vac} is the energy of an electron at rest in the vacuum nearby the surface, and E_F is the Fermi level inside the material. For intrinsic semiconductors at absolute zero temperature, the energy of the photon needed to eject an electron would correspond to the top of the valence band as the Fermi-level does not have any electron states.

2.2 Photoemission

Light or photons are electromagnetic waves, carrying quanta of energy proportional to the frequency of the electromagnetic wave. This energy quantum can be used to eject an electron from a material if the energy is higher than its binding energy. For bulk material, this binding energy is referred to as the material's work function. This is formulated as

$$E_K = h\nu - W_e \,, \tag{2.2}$$

where E_K is the kinetic energy of the electron, h the Plank constant, ν the frequency of the photon, and W_e the work function. The threshold frequency for emission to occur, ν_{W_e}, is equal to $W_e = h\nu_{W_e}$. Any frequency of light below this will not eject an electron, no matter the intensity. When the kinetic energy imparted on the electron is positive, it is ejected, with any excess energy translating to a higher initial velocity.

2.2.1 Quantum efficiency

The ratio of emitted electrons to absorbed incident photons of a certain wavelength is called quantum efficiency [56], defined as

$$QE = \frac{\Delta Q/q_e}{\Delta E/h\nu} = \left(\frac{h\nu}{q_e}\right)\frac{\Delta Q}{\Delta E} \,, \tag{2.3}$$

where ΔQ is the total emitted charge and ΔE is the total absorbed energy. With $\Delta Q/q_e$ being the number of electrons emitted and $\Delta E/h\nu$ the number of photons absorbed. This is known to scale proportionally to the kinetic energy squared or

$$QE = \frac{h\nu}{q_e}\left(\frac{J}{I_\lambda}\right) \propto (h\nu - W_e)^2 \,, \tag{2.4}$$

where J is current density and I_λ is the intensity of incoming photons (f.ex. by a laser). Equation (2.4) shows that quantum efficiency has to be evaluated at a certain wavelength. Quantum efficiency is a measure of longitudinal momentum distribution while thermal emittance is a transverse momentum distribution. They are orthogonal to each other while interlinked in such a way that only electrons with low transverse momentum are ejected. For metals, the transverse momentum is usually high, resulting in very low quantum efficiency for metals, 10^{-4}, over the possible spectrum while some semiconductors can reach unity, those with negative electron affinity targets exhibiting significantly higher efficiency. It should be noted that this effect is stochastic in nature.

2.2.2 Transit time

The transit time in a diode is the time it takes an electron to cross from the cathode to the anode. The transit time is affected by the magnitude and shape of the applied

electric field and space-charge field. A good estimate of the transits time is that for a single electron traversing a planar diode. This can be shown to be

$$\tau_{\text{v}} = \sqrt{\frac{2m_e}{q_e V}} D. \tag{2.5}$$

2.3 Space Charge limit

The space-charge limit refers to a phenomenon when the current becomes self-limiting due to the presence of charged particles in the diode gap that reverse the electric field at the cathode, hindering the charged particle flow [42]. The classic Child-Langmuir Law describes this for a steady state current density in a 1D, planar, vacuum diode with gap distance D, gap voltage V, no magnetic field, zero initial velocity $v_{xyz} = 0$, with only electrons as charge carriers using classical mechanics and electrostatic approximations. The law is derived by solving the Poisson equation

$$\nabla^2 \phi = \rho / \varepsilon_0 \ , \tag{2.6}$$

using the following constraints

$$\nabla \phi \Big|_{x=0} = 0 \ , \tag{2.7}$$

$$\phi(0) = 0 \ , \tag{2.8}$$

$$\phi(D) = V \ , \tag{2.9}$$

and the following relations connecting current density, electron velocity and potential.

$$J = \rho v \ , \tag{2.10}$$

$$v = \sqrt{\frac{2q_e \phi}{m_e}} \ , \tag{2.11}$$

where ϕ is the potential, ρ is the charge density, J is current density, v is velocity of the electrons, ε_0 is the permittivity of free space, and m_e the mass of the electrons, which when reordered gives the one-dimensional Child-Langmuir law

$$J_{\text{CL(1D)}} = \frac{4}{9} \varepsilon_0 \frac{V^{3/2}}{D^2} \sqrt{\frac{2q_e}{m_e}} \ . \tag{2.12}$$

$J_{\text{CL(1D)}}$ describes the maximum steady-state current density achievable in a one-dimensional diode. This equation applies to a one-dimensional parallel plate diode, there are extensions for different geometries, quantum effects in nanodiodes, relativistic effects in high energy beams, limited emission areas, and transient emission [57]–[61].
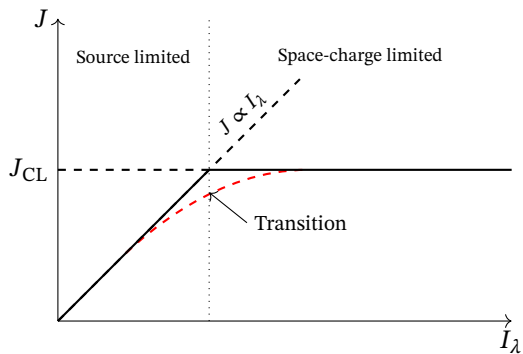
Figure 2.2: The ideal photoemission curve relating current density with light intensity for one-dimensional system. The dashed red line shows the transition curve for a higher dimensional system.

2.3.1 Source limited to space-charge limited current

In the absence of space-charge, the emission is described by governing equations appropriate to emission mechanism, e.g. for thermal emission it is

$$J_{\text{RLD}} = A_{\text{RLD}}T^2 \exp\left(-\frac{\varphi}{k_{\text{B}}T}\right) \tag{2.13}$$

for field emission

$$J_{\text{FN}}(F) = \frac{q_e}{2\pi\hbar}\left(\frac{m_e}{\pi\hbar^2 C}\right)P(\mu)e^{-B/F}\int_0^{C\mu} xe^{-x}\,dx \tag{2.14}$$

and for photoemission

$$J(\hbar\omega) = \frac{q_e}{\hbar\omega}[1 - R(\omega)]F_\lambda I_\lambda P(\hbar\omega)\,, \tag{2.15}$$

where I_λ is the intensity of light at wavelength λ, $R(\omega)$ is reflectivity factor, F_λ is scattering factor, and $P(\hbar\omega)$ is emission factor. Note that the Child-Langmuir limit is independent of material properties and emission mechanism. This is visualized in Figure 2.2, showing an idealized curve relating current density to the light intensity for photoemission in a diode.

2.3.2 Limited emitter area

It has been shown that the space-charge limited current can be considerably different when the emitter area is finite, unlike the infinite emitter area assumed in the Child-

Langmuir law [57], [62]. Lau [57] constructed a simple theoretical model for steady-state space-charge limited current from a finite emitter area assuming no beam expansion, uniform current density across the emitter, and the characteristic length l of the emitting area is much larger than the gap spacing D. This was extended by Koh and Ang [59] with a geometric factor to a general equation relating two dimensional current density with the one-dimensional current density for various geometries

$$J_{\text{CL(2D)}} = J_{\text{CL(1D)}}(1 + G)\,, \tag{2.16}$$

where the geometric correction factor G depends on the emitter, f.ex. the factor for circle is $D/(4R)$ with radius R, and for a square $(\sqrt{2}D)/(\pi L)$ with side length L. This has been shown to be very accurate for ratios $l/D > 0.5$. In most real cases the current density at the edge of the emitter is considerably greater than on the interior. It has been shown that for microscopic emitters the edge emission and transverse beam expansion can cause considerably higher current than predicted by Equation (2.16) [63].

2.3.3 Space-charge limit for short pulse emission

For many important applications, the duration of the electron emission is less than the transit time of the diode and the steady state model is no longer applicable. A simple one-dimensional model for short pulse τ_{p} injection relates the length of the current pulse to the critical injection current J_{crit} before the formation of a virtual cathode occurs [25]:

$$J_{\text{crit}} = \frac{\varepsilon_0 V}{\tau_{\text{p}} D}\,, \tag{2.17}$$

for very short pulses or more generally

$$J_{\text{crit}} = 2\frac{1 - \sqrt{1 - \frac{3}{4}X_{\text{CL}}^2}}{X_{\text{CL}}^3}J_{\text{CL}}\,, \tag{2.18}$$

where $X_{\text{CL}} = 2\tau_{\text{p}}/(3\tau_{\text{v}})$ is normalized pulse length, ranging from zero to one. Equation (2.17) describes accumulation of charge near the cathode surface that is sufficient to reverse the electric field disrupting further emission. In the limit of vanishing pulse length, this becomes a sheet of charge with surface charge density

$$\sigma = \varepsilon_0 \frac{V}{D}\,. \tag{2.19}$$

For an infinite planar diode, the so-called capacitive model of transit for this sheet across the diode is described with

$$J_{\text{CL}} = \frac{8}{9}\frac{\sigma}{\tau_v}\,. \tag{2.20}$$

Chapter 3

Simulated photoemission pulse in a microdiode

Short pulse electron beams are important in many applications, e.g. high power microwave sources for hundreds of GHz and THz [11], time resolved electron microscopy [64], [65], and free electron lasers [66]. Ideally these bunches should be coherent and have high current, a characteristic which can be quantitatively measured in terms of the beam brightness. In this thesis the following definition of brightness from Reiser [67] is used,

$$Br = \frac{\eta I}{\epsilon_x \epsilon_y} \propto \frac{I}{\epsilon^2} \, , \qquad (3.1)$$

where η is a geometric constant equal to $2/\pi^2$, I is the current along the beam direction, z, and $\epsilon_{x,y}$ are the emittances in the transverse directions, x and y, describing the lateral spread of the beam in the phase space [56], [68], which are expected to be equal for a beam with transverse symmetry.

High current and low emittance are somewhat competing goals, as high current beams are subject to space-charge forces that lead to increased emittance [69]. This trade-off between current and emittance suggests that an optimal value of brightness exists. In fact, this has been observed for pulsed photoemission, both experimentally [70], and from simulations [71]. Optimal brightness is not limited to pulsed photoemitted beams. For instance, it has been observed in simulations of thermal emission in microdiodes, that optimal brightness is obtained during the transition from source-limited emission to space-charge limited emission [72]. The work presented in this chapter was initiated as a study of the corresponding transition to space-charge limited photoemission from a planar cathode.

For that purpose, a high-fidelity molecular dynamics code, called Reykjavik University Molecular Dynamics for Electron Emission and Dynamics (RUMDEED) [72],

[73] is used. It includes discrete particle emission, scattering, and space-charge effects on electron emission and propagation, to model the physics of electron beamlets near the cathode. The transition from source-limited to space-charge limited emission is investigated and it is shown how optimal brightness can be obtained with regard to nonlinear physics in the vicinity of the cathode.

There are a number of sources of emittance growth that can diminish the brightness of a beam as it propagates through a device due to effects such as misalignment of focusing and accelerating components, beam mismatch, nonlinear forces etc. [67], but it is useful to look carefully at what is happening at the cathode and in its immediate neighborhood for better understanding of ultimate limits to brightness. This will be executed through isolation of space-charge and discrete particle effects on photoemission of electrons and their propagation in the immediate vicinity of the cathode, how the transition from source-limited emission to space-charge limited emission happens, and how that affects the beam brightness. The model used does not incorporate cathode temperature, surface protuberances, or variable work function on the cathode surface. The results on the transition from source-limited emission to space-charge limited emission will be compared to commonly used models.

3.1   Code methodology

Here the molecular dynamics computer simulation method is being used to investigate how the electron beam evolves with regards to emitter size, width and amplitude of the photon pulse, and the applied potential. The method uses a direct particle-to-particle interaction to calculate the Coulomb force between each and every particle, numerically solving the Newtonian equations of motions, collisions, and image charge partners with high fidelity. Two decades ago this method would have been computationally too costly, however with advancements in CPU technology the run time for such simulations is no longer prohibitive, making it possible to run large systems with electrons in the thousands multiple times to get a statistical result.

3.1.1   Electron emission

The system is an infinitely wide vacuum diode, with the anode-cathode gap spacing denoted by D, zero voltage at the cathode, and applied voltage V at the anode. The emission area is a disk with radius R which is assumed to be smaller than D. The work function of the emitter W_e is uniform over the area and equal to the average energy of the photons. The photons in a pulse have energies E, with a Gaussian distribution, with average $\langle E \rangle = h\nu$, and with a very small standard deviation $\sigma_E \ll h\nu$. The number of photons N_p within the pulse also have a Gaussian distribution, but as a function of time. The time is discretized in small steps Δt, the width of the pulse is σ_N time steps, and in practice the total duration of the pulse τ_p is assumed equal to
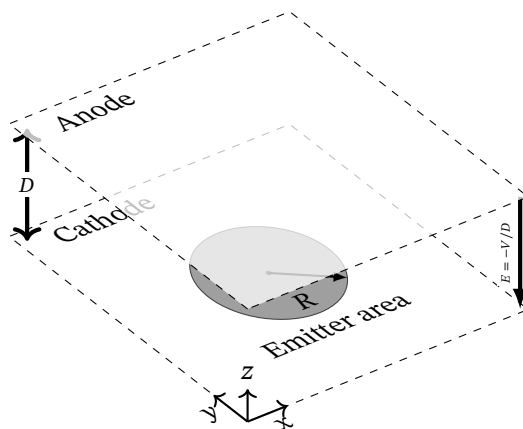
Figure 3.1: Simulated vacuum diode system model, circular emitter area with radius R, gap size D is 2500 nm and gap electrostatic potential V.

$16\sigma_N \Delta t$. Electron emission is carried out using a Monte Carlo approach. In each time step, the algorithm selects an emission site randomly. The computational method is the following: A random point within the circular emitter area of the cathode, $p_1 = (x_1, y_1, 0)$, is selected. First, the energy of the photon is compared to the work function at the site to see if emission is possible. To determine if this point is viable the z-component of the electric field is calculated at the point, adding the contribution from the applied electric field and the contributing electric field from each of the N_e electrons already present in the diode gap. Then, if the electric field at p_1 favors the emission, i.e. it is oriented such that the force on the electron would accelerate it towards the anode, a second check is made at 1 nm above p_1, should that be favorable an electron is placed at the point, $p_{1\alpha} = (x_1, y_1, 1\,\text{nm})$, increasing the number of electrons in the gap by one, $N_e + 1$. If neither the work function or the local electric field at p_1 or $p_{1\alpha}$ is favorable, no electron is placed outside the cathode, and a failure of the emission event is recorded. This process is repeated until either the maximum number of emitted electrons allowed by the Gaussian pulse at that time step, or 100 recorded failures to place, have been reached [74]. With the Gaussian limit not being reached, or ultimately with no favorable site for emission, will indicate the space-charge limited regime. This mode of electron placement ensures a self-consistent current density over the emitter cathode, whether source limited or space-charge limited.

The electrons are emitted with the initial velocity v_{z0} corresponding to the excess energy transferred by the incoming photon, assuming the emission occurs in
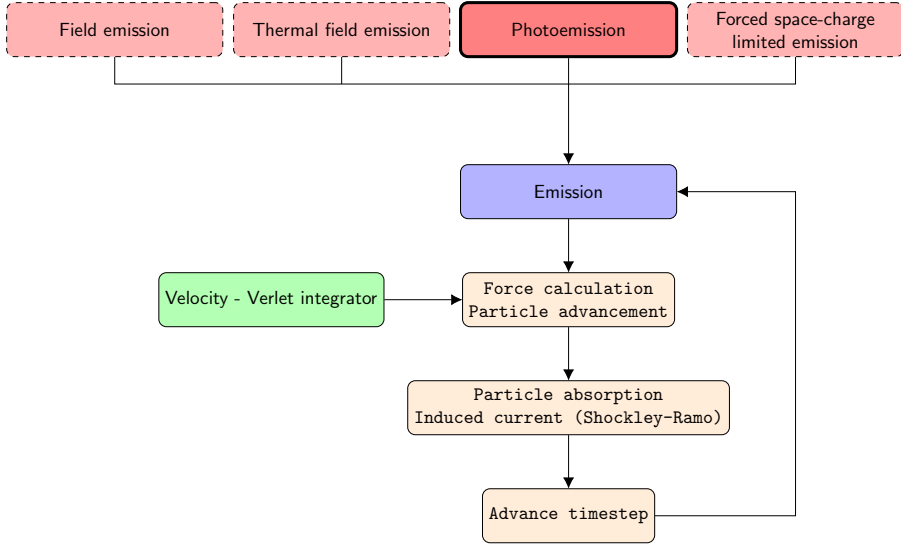
Figure 3.2: Basic code structure

the direction normal to the surface of the emitter,

$$v_{z0} = \sqrt{2(E - W_e)/m_e}\ . \tag{3.2}$$

The dispersion of v_{z0}, due to the small dispersion of the photon energy, is obviously also small. The number of emitted electrons is a function of time, and it follows the Gaussian photon pulse. At each time step the theoretical (or virtual) number of electrons that could possibly be emitted is modeled as a Poisson random variable, with an expected value given by the quantum efficiency (QE) multiplied by the number of incoming photons during that time step, which in fact is the average number of emitted electrons in the absence of an electric field and space-charge effects. Although the pulse duration is short, below 1 ps, the possible multiphoton emission events are neglected. In this numerical implementation the pulse intensity is described by the amplitude of the virtual electron pulse emitted by the cathode (i.e. the mean value at the middle of the pulse), which is an input parameter, referred to as the scaled laser amplitude.

3.1.2   Advancement

The next step of the simulation is to calculate the net forces acting on every electron due to the direct Coulomb interaction within the other electrons in the system, in-

cluding the image charge partners outside the boundaries of the simulation box, and due to the accelerating field created by the anode. At a given time, $t = t_i = i \times \Delta t$ there are N_e electrons in the gap. The position of an electron at this time is given by $r_{ni} = (x_{ni}, y_{ni}, z_{ni})$, where n ranges from 1 to N_e. The force acting upon the electron at this time is $F_{ni} = (F_{xni}, F_{yni}, F_{zni})$, and is the sum of the force due to the applied electric field, the electrostatic force between electron n and all the other $N_e - 1$ electrons as well as their image charge partners are calculated from their positions at time t_i. Then the time step is advanced and the velocity-Verlet algorithm is used to calculate the new positions and velocities of the electrons at time $t_i + 1 = t_i + \Delta t$ [75]–[77]

$$x_{n(i+1)} = 2x_{ni} - x_{n(i-1)} + \frac{F_{xni}}{m}(\Delta t)^2 , \tag{3.3}$$

The same method is used to calculate $y_{n(i+1)}$ and $z_{n(i+1)}$ positions. For the electrons injected at t_i there is no previously defined position at time t_{i-1}, instead the follwing is used:

$$x_{n(i+1)} = x_{ni} + \frac{F_{xni}}{2m}(\Delta t)^2 . \tag{3.4}$$

The position of electrons are calculated in this manner as long as they are in the gap. Electrons that pass the boundaries, $x-y$ plane at either $z = 0$ or $z = D$, of the anode or cathode are recorded and removed from the system. Thus it is possible that a recently injected electron is pushed back into the cathode due to the evolving electric field. The simulation works through the process of electron emission and advancement for each time step until a user selected end point. The total current through the diode is calculated using the Ramo-Shockley theorem [78], [79],

$$I = \frac{q}{D} \sum_i v_{iz} , \tag{3.5}$$

where q is the electron charge, and v_{iz} the component of the instantaneous velocity of the electron i, that is normal to the cathode surface (i.e. in the z direction). In order to observe the effect of pulse relative to the entire system size, the pulse width τ_p is normalized with the transit time of a single electron from the cathode to the anode,

$$\tau_v = D\sqrt{\frac{2m}{qV}} , \tag{3.6}$$

yielding $\tau_n = \tau_p/\tau_v$, or

$$\tau_n = \frac{16\sigma_N \Delta t}{D}\sqrt{\frac{Vq}{2m}} . \tag{3.7}$$

Thus, if the duration of the laser pulse is equal to the time it takes for a single electron to be accelerated from the cathode to the anode then $\tau_n = 1$. In the interest of calculating the brightness defined in Equation (3.1), the maximum value of the Ramo-Shockley current given by Equation (3.5), and the statistical emittance, appropriate
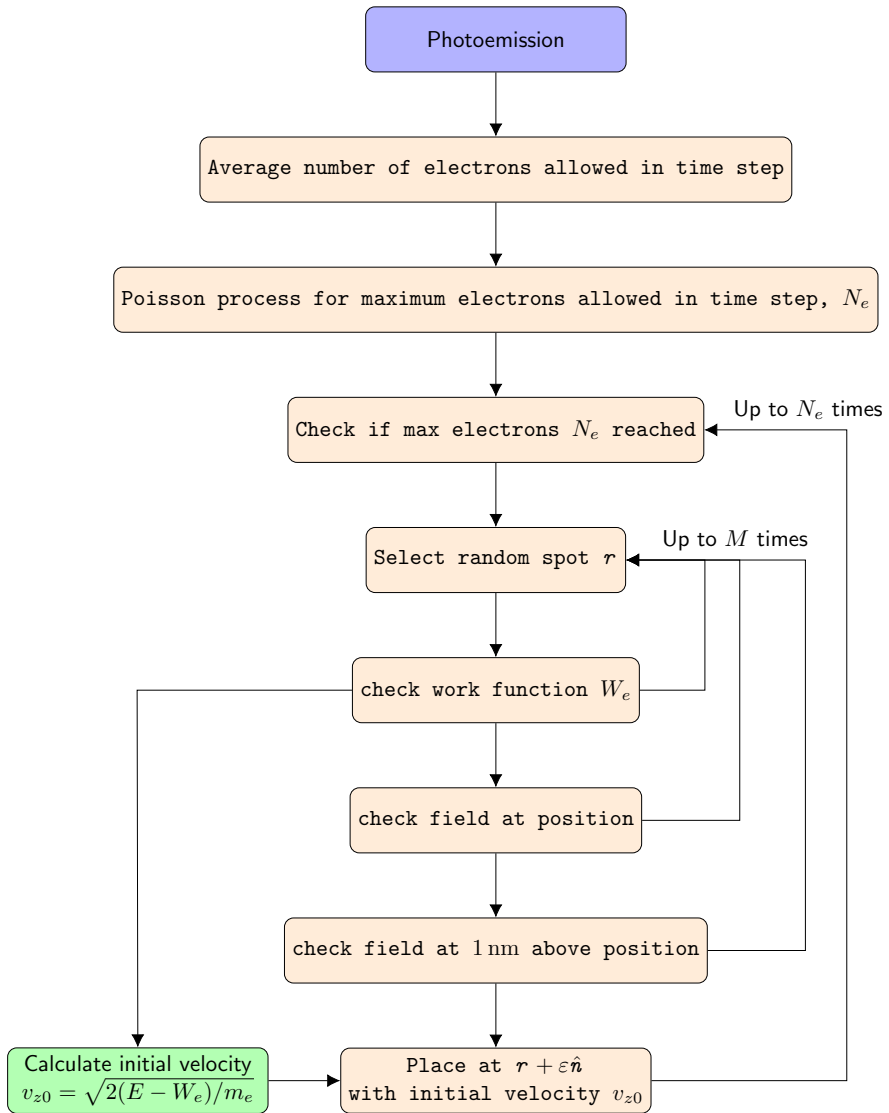
Figure 3.3: Photoemission module

for this computational approach was used [80],

$$\epsilon_x = \sqrt{\langle x^2 \rangle \langle x'^2 \rangle - \langle xx' \rangle^2} \tag{3.8}$$

with x denoting the position and $x' = dx/dz = v_x/v_z$ being the deviation angle of the particle in the x direction. The angular brackets represent averages over all electrons when they pass through the anode. The corresponding similar formula is used for the y direction.

3.1.3 Photoemission simulation parameters

The numerical values of the parameters used in the simulations are: The radius of the disk-shaped emission area of 125 nm, 187.5 nm and 250 nm; the distance between the cathode and the anode $D = 2500$ nm; the anode-cathode potential difference of 50 V, 75 V and 100 V; the simulation time step $\Delta t = 0.25$ fs with the total running time of 15 ps; the center of the emission pulse 5 ps with amplitude (1, 2.5, 5 and 10), the average number of electrons at emission peak and pulse-width from 4 fs to 4000 fs; 10 simulation runs per point; mean energy of photons 4.7 eV with a standard deviation of 0.02 eV; the work function of the material was chosen to be 4.7 eV, approximating copper as cathode material. With amplitude of 1.0, the laser intensity corresponds to 1.5 MW cm^{-2} to 6.1 MW cm^{-2} depending emitter size and assuming 100% QE, this would of course increase with lower QE. This might be high in real terms, however, in the interest of simulating these space-charge limited effects this parameter is intentionally kept high.

3.2 Results and discussions

Looking at the current induced in the diode as a function of time, Figure 3.4, with two different values for the pulse width, τ_p, fixed gap voltage at 75 V, and the emitter radius and amplitude of the laser pulse are held constant as well. The peak of the laser pulse is located at time $t = 5$ ps, and note that the transit time for a single electron across the diode gap for the given voltage is 0.97 ps. In the case of $\tau_p = 60$ fs, emission is source limited and the charge is emitted in a tight bunch at approximately 5 ps. This bunch of charge is subsequently accelerated across the gap by a nearly constant applied electric field, resulting in an induced current that grows linearly with time until the foremost electrons in the bunch are absorbed by the anode, at which time the induced current begins to drop due to absorption of charge. In the case of $\tau_p = 400$ fs, emission is space-charge limited and begins slightly prior to the 5 ps mark but nonetheless manifests as a bunch of electrons that are accelerated across the diode gap leading to linear growth of the induced current in time until the leading electrons are absorbed at the anode. From the figure it is apparent that the bunch length is greater for the wider laser pulse as would be expected.

Figure 3.4: Temporal profile of induced current for two different laser pulse-widths (400 fs in blue, and 60 fs in red). Gap voltage is 75 V, emitter radius of 250 nm, Scaled laser amplitude of 10. Dashed and dashdot lines indicate when first and last electrons cross anode.

In the conventional analysis of the Child-Langmuir current it is implicit that the current is constant in time for fixed external parameters [26]. As the width of the laser pulse is increased so as to exceed the transit time across the gap, there is a transition in the current profile as a function of time when looking at Figure 3.5. For long values of the pulse length the rise in the current is no longer linear, as would be expected for a short electron bunch, but has a steadily increasing gradient due to the fact that the number of electrons being emitted from the cathode increases gradually with time. Observe, there is a plateau in the current which occurs once the diode gap has been filled with a steady current. This plateau corresponds to the steady-state space-charge limited current in the diode. Before looking in more detail at how the normalized pulse length affects the current it is worthwhile to look at some common models for analysis of space-charge limited emission from finite area emitters and for short pulses. Lau [57] devised a simple and elegant theory for steady-state space-charge limited current from a finite emitting area which was later extended by Koh and Ang [59]. From Koh and Ang's work it is expected that the current density from a circular emitter of radius, R, and diode gap spacing, D, when the emission energy is negligible should be:

$$J_{\mathrm{CL(2D)}} = J_{\mathrm{CL}} \left(1 + \frac{D}{4R} \right), \tag{3.9}$$
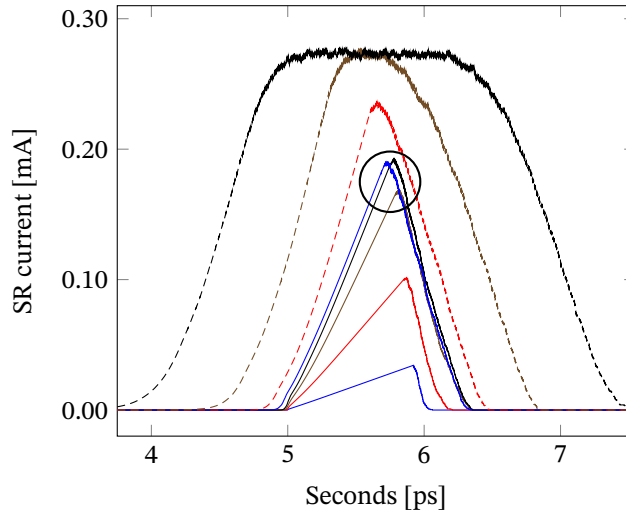
Figure 3.5: Temporal profile of induced current for a number of different laser pulse-widths ranging from 20 fs to 4000 fs. Gap voltage is 75 V, emitter radius of 250 nm, Scaled laser amplitude of 10. The lowest peak current is on the trace for smallest pulse-width. The circle surrounds peaks of traces for pulse widths ranging from 120 fs to 400 fs.

where J_{CL} is the classical Child-Langmuir current for an infinite planar diode, given by

$$J_{CL} = \frac{4\pi}{9}\varepsilon_0\sqrt{\frac{2q_e}{m_e}}\frac{V^{3/2}}{D^2} \ . \tag{3.10}$$

From this the expected steady state current in the system can be calculated

$$I_{CL(2D)} = \frac{\pi}{9}\varepsilon_0\sqrt{\frac{2q_e}{m_e}}V^{3/2}\left(\frac{4R^2}{D^2} + \frac{R}{D}\right) \ . \tag{3.11}$$

For short-pulse emission a one-dimensional model (assuming a planar diode of infinite extent) predicts that for a pulse of constant injected current of duration τ_{pulse} there is a critical current density, J_{crit} that is the maximum allowed to ensure that a virtual cathode does not form. In its simplest form, where the bunch of charge is approximated as a single sheet, this critical current density is given by [25]

$$J_{\text{crit}} = \frac{\varepsilon_0 V}{\tau_{\text{pulse}}D} \ . \tag{3.12}$$
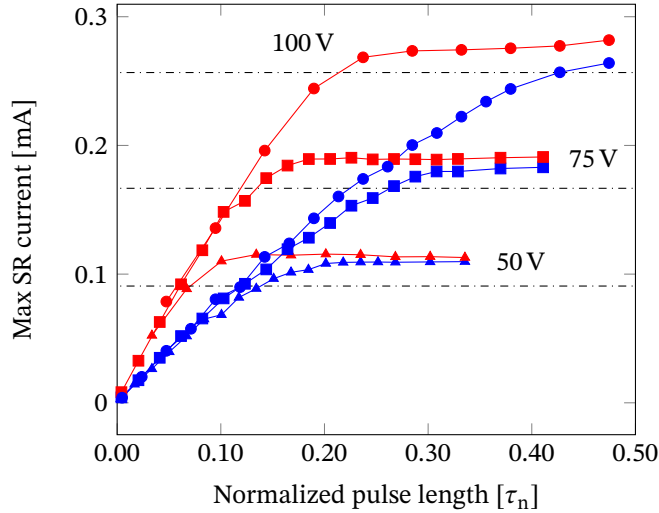
Figure 3.6: Induced current vs. normalized pulse length for three different gap voltages: 50 V, 75 V and 100 V, 250 nm emitter radius with curves for scaled laser amplitudes of 5 (blue) and 10 (red). The current from Equation (3.11) is represented by the horizontal dash-dotted lines for 50 V, 75 V and 100 V.

This model essentially assumes that for a short bunch, approximated as a single sheet, a virtual cathode will form when the surface-charge density of the sheet is equal to the surface-charge density of the cathode surface due to the applied electric field, namely $\sigma = \varepsilon_0 V/D$. The approximation that, under space-charge limited conditions, the charge may considered to be a single sheet, of the aforementioned surface-charge density, transiting the gap in the appropriate time, is called the capacitive model and has been used successfully to derive the classic Child-Langmuir law [81]. The capacitive model for charge density has also been used for analysis of short beam bunches of finite diameter [70]. Looking at the current as a function of the width of the laser pulse. Figure 3.6 shows how the maximum value of the induced current varies with the normalized pulse length (the ratio of the laser pulse width to the transit time of a single electron across the diode gap). It is noted that for very short pulse width the maximum current increases proportionally with the normalized pulse length. This is indicative of source limited emission where charge can continually be added to the diode gap in proportion to the rate of photoemission and pulse duration. The growth rate is independent of applied voltage but dependant on the amplitude of the laser pulse. For slightly longer pulses, that are nonetheless short compared to the transit time, the accumulation of space-charge is sufficient to block further emission of photo-electrons and the current reaches a plateau indica-
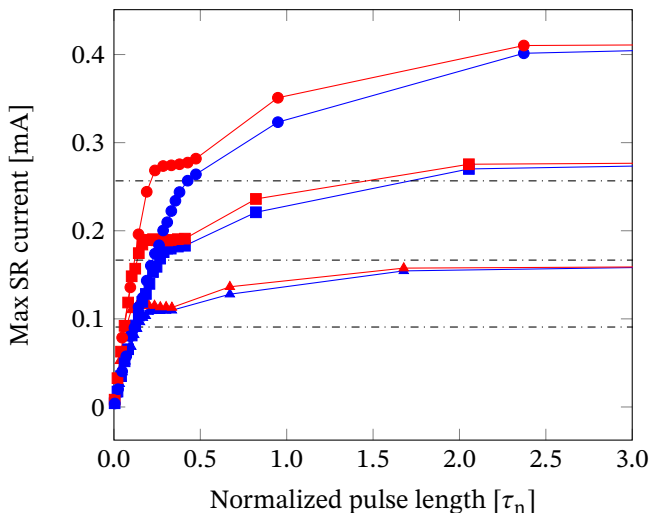
Figure 3.7: 50 V, 75 V and 100 V, 250 nm emitter for scaled laser amplitude of 5 (blue) and 10 (red).: the CL limit from Equation (3.11) is drawn in black for the different gap voltages.

tive of space-charge limited emission. This current limit is determined by the applied voltage, but note that for lower laser amplitude a greater normalized pulse length is needed to reach the critical amount of charge in the electron bunch. It can also be seen that the space-charge limited current is somewhat higher than that predicted by Equation (3.11). The space-charge limited current observed here corresponds to the maximum current shown within the circle in Figure 3.5 for laser pulse width ranging from 120 fs to 400 fs. In Figure 3.7 the abscissa has been extended to show values of the normalized pulse width that extend beyond unity. This figure shows the transition from the plateau that corresponds to space-charge limited current for a short bunch to another, higher, plateau that corresponds to the space-charge limited steady-state current. Here the steady-state space-charge limited current is considerably higher than predicted by Equation (3.11). It has previously been observed [63] that the steady-state space-charge limited current from microscopic emitters can deviate considerably from what is predicted by the simple 2D Child-Langmuir law, due to the relatively high contribution to the current from the edge of the emitting area, the so-called wing-structure of the emission profile [62], [82], transverse beam expansion, and discrete particle effects. Hence, the underestimation of Equation (3.11) for the steady-state, space-charge limited current is not unexpected.

What may seem unexpected, in light of previous work on short-pulse emission, is that the space-charge limited current for a short pulse is less than the space charge-

limited current for the steady-state. This is not a discrepancy. In part the explanation lies within the fact that in the previous work on the short-pulse space-charge limit the maximum injection current allowed so as not to form a virtual cathode over the duration of a given pulse length, whereas in this model is looking at the induced current (which is due to the transit of the critical bunch of charge, once formed, across the diode gap). Thus the inverse scaling of the critical current with pulse length is not appropriate. However, the reason that the space-charge limited current in the steady-state is higher than that of a short bunch has a physical reason associated with the mechanics of space-charge limited current from a microscopic emitter, as will be described when the total charge of the pulse is examined in the following paragraphs. Since it is apparent that, for short pulses, it is the single sheet model that is most appropriate for the amount of charge in the electron bunch as a function of laser pulse width for different values of laser amplitude, emitter area and gap voltage. Figure 3.8 shows how the laser amplitude affects total charge as a function of the normalized pulse length. Greater amplitude corresponds to a higher rate of photo-electrons being produced at the cathode. The space-charge limit shows up as a plateau in the total charge in the pulse. For low laser amplitudes the space-charge charge limit can not be reached, whereas it is obtained at shorter pulse lengths for larger amplitudes.

From Figure 3.9 it can be seen how the gap voltage affects the total charge. From the simple, single sheet model where the charge density of the sheet is given by $\sigma = \varepsilon_0 V/D$, and emitter radius of 250 nm, the expected total charge is 0.35 fC, 0.52 fC, and 0.70 fC for gap voltages of 50 V, 75 V and 100 V respectively. The measured charge is 2 to 3 times higher. The reason for this difference is that the estimation for the charge density of the sheet does not take into account the effects of limited emitter area that are implicit in the 2D Child-Langmuir law. Note for instance that the space-charge limited current density from Equation (3.11) with values of $R = 250$ nm and $D = 2500$ nm is 3.5 times higher than the space-charge limited current density for an emitter of infinite extent. From the single sheet model a linear relationship between the critical charge and the gap voltage would be anticipated, however the charge increases at a lower rate with voltage, e.g. the total charge for the pulse at 100 V is only 60 percent greater than the total charge at 50 V. This can not be explained.

Looking next at how the total charge is affected by the radius of the emitting area. There is a linear rise in the pulse charge with pulse length until a plateau due to space-charge limitation is reached. For the single sheet, capacitive, model it is expected that the charge at the plateau scales with the area of the emitter (the emitter radius to the second power). This is not the case as the current from the 250 nm radius emitter is roughly three times higher than the 125 nm radius emitter, instead of four times higher as might be expected for a single sheet of uniform charge density. This can probably be explained by the fact that edge emission has a larger contribution to the total charge for the emitter of smaller radius. It should also be noted that for larger values of the normalized pulse, the total charge increases again as the transition from the single-sheet regime to the steady-state filled cathode regime be-
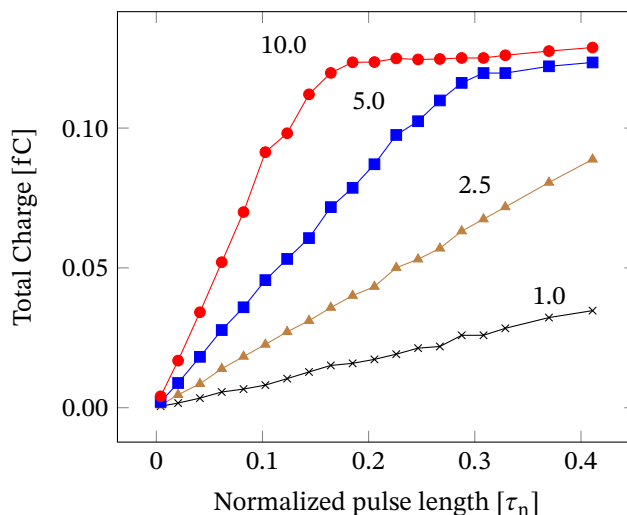
Figure 3.8: Total charge vs. normalized pulse length for scaled laser amplitude of 1, 2.5, 5 and 10. Gap voltage of 75 V, 250 nm radius emitter. The lowest amplitude (black) will not reach the space-charge limit before saturating the gap with constant current.

gins. Recalling that the steady-state space-charge limited current is greater than that anticipated by Equation (3.11) due to a large fraction of the emission coming from the edge of the emitter and due to transverse expansion of the beam [63]. This effect becomes more prominent as the ratio Z_c/R increases, where Z_c denotes the elevation of the center of charge above the cathode and R is the emitter radius. As a result of this, the single-sheet current transition to the steady-state regime for larger area emitters begins when the beam bunch has propagated further along the diode than for smaller emitters. Hence, the transition between regimes occurs earlier for smaller emitters. Lastly, the brightness of the electron beam, looking at the data underlying Figure 3.8 and plotting the brightness of the beam as a function of normalized pulse length for different values of the laser amplitude. This can be seen in Figure 3.11 and Figure 3.12 where a peak value of the brightness is readily apparent. The peak value it self is roughly constant, though the peak becomes sharper as the laser amplitude increases. Note that the peak brightness is achieved when the charge in the electron bunch corresponds to roughly 40 percent of the critical charge for the short-pulse space-charge limit, which holds true for all voltages and emitter radii that were simulated.
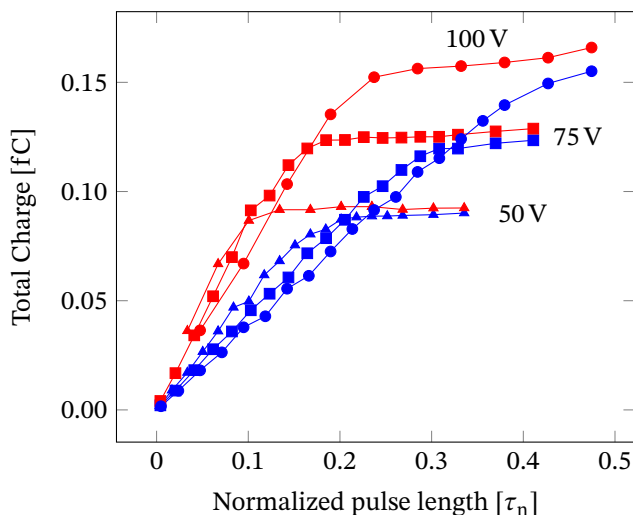
Figure 3.9: Total charge vs. normalized pulse length for three different voltages. 50 V, 75 V and 100 V, 250 nm emitter, scaled laser amplitude of 5 (blue) and 10 (red). Increased voltage affects the space-charge limit with respect to pulse length while slope is related to amplitude.

3.2.1   Emittance

Looking exclusively at the emittance and displaying it for different values of amplitude, emitter size, pulse width, and voltage, a few notable observations can be made. In Figure 3.13d can be seen that the general trend is for higher voltage reduce emittance, with 100 V in red, 75 V in yellow, and 50 V in blue. While in Figure 3.13b for larger emitter size the emittance increases while variance is slightly reduced. For both pulse width and amplitude in Figure 3.13c and Figure 3.13a respectively, the relationship is not as clear, with only increased emittance observed for increase in both. For the shortest pulse width, the emittance is very low with high variance, this can be explained by the small number of electrons in the pulse. Namely low scattering leads to low emittance, while small numbers lead to high statistical fluctuation.

Looking exclusively at 250 nm emitter in Figure 3.14 with pulse widths 160 fs and 4000 fs. There is an interesting trend with regards to amplitude, when the diode is in steady-state space-charge limited regime i.e. the long pulse, the emittance is very tightly focused with very little variance (Figure 3.14c), however as the amplitude is increased the emittance is slightly reduced (Figure 3.14a). This is completely opposite to short pulse, seen in Figure 3.14a, where with increased amplitude the emittance is drastically increased. Another observation, in Figure 3.14d, is that the voltage has no effect on the steady-stage space-charge limited pulse, this is in agreement with
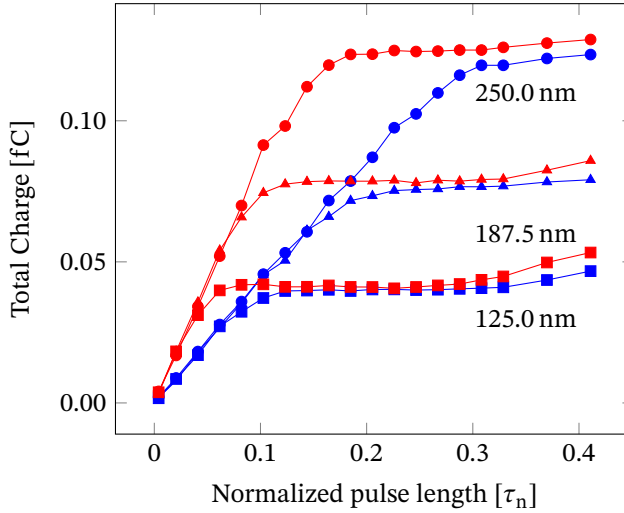
Figure 3.10: 75 V, 125 nm, 187.5 nm and 250 nm radius emitters, scaled laser amplitude of 5 (blue) and 10 (red). Emitter size increases the space-charge limit with respect to pulse length while again the slope is related to amplitude.

sheath formulation by Lieberman and Lichtenberg [83].

3.3   Conclusions

Using MD-Simulations the transition from source limited emission to space-charge limited emission in photo-emitted electron beams in a microscopic diode for different values of laser pulse-width, intensity, emitter area (or spot size) and accelerating potential was examined. The conventional capacitive models of short-pulse electron bunches may considerably underestimate their total charge due to neglecting two-dimensional space-charge effects, whereas the estimates for the short-pulse space-charge limited current using the approach of Koh and Ang shown in Equation (3.9) give a reasonably accurate estimate for the maximum current induced by a electron bunch transiting the diode gap. Parameters for optimal brightness of the beam bunch were identified. In the parameter range that was studied, the highest value of brightness was found to occur when the charge in the beamlet is roughly 40 percent of the critical charge for formation of virtual cathode. This result is similar to what has been found for thermal emission in microdiodes, in that optimal brightness is achieved at a point during transition from source-limited to space-charge limited emission. This may have some practical value for designers of electron sources for coherent and time resolved electron beams.

Figure 3.11: Brightness versus normalized pulse length for different scaled laser amplitudes. 75 V gap potential, 250 nm emitter radius: The brightness peak shifts to the left, shorter pulse width, as the amplitude increases. Black, brown, blue, red, correspond to 1, 2.5, 5 and 10 in amplitude respectively.
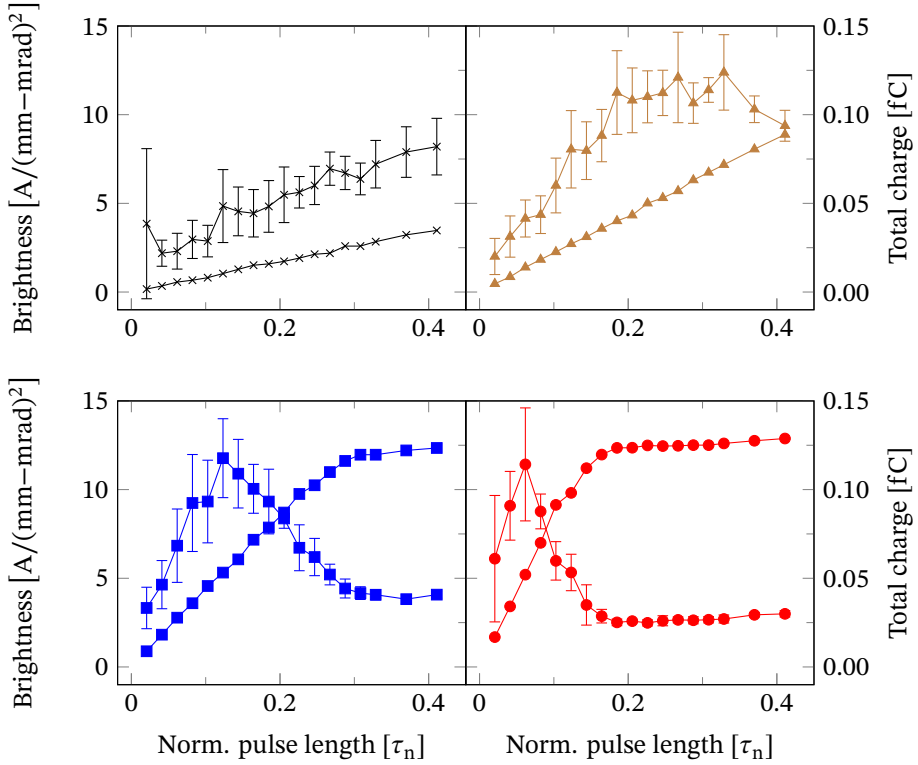
Figure 3.12: Brightness and total pulse charge versus pulse length. 75 V gap potential, 250 nm emitter radius: Charge and brightness lines of rising amplitudes have the same colors, brightness has error bars. Black, brown, blue, red, correspond to 1, 2.5, 5 and 10 in amplitude respectively. The Brightness peak hits at approx. 40% of total charge peak.

(a) Emittance with regards to amplitude

(b) Emittance with regards to emitter size

(c) Emittance with regards to pulse width

(d) Emittance with regards to voltage
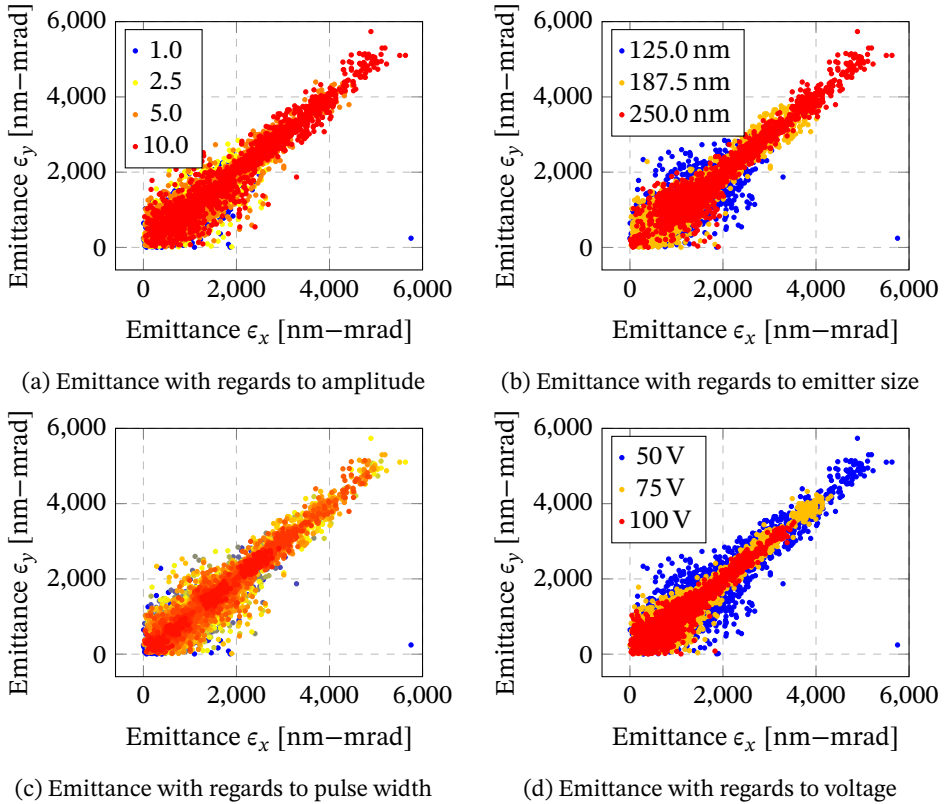
Figure 3.13: Using heat color map, going from blue to red to indicate low to high values, the emittance ϵ_x and ϵ_y is plotted against each other. Note for Figure 3.13c, the range of the heat map is 20 fs to 4000 fs.
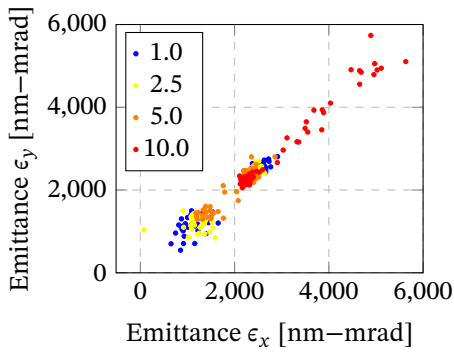
(a) Emittance with regards to amplitude
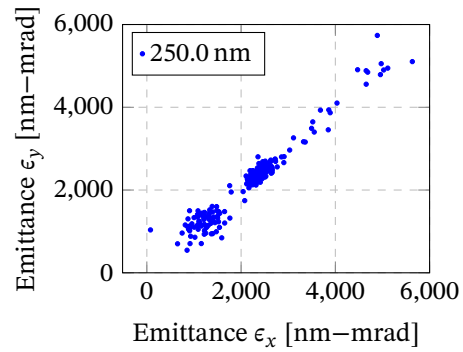
(b) Emittance with regards to emitter radius
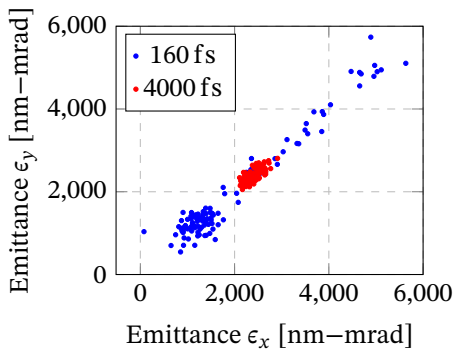
(c) Emittance with regards to pulse width
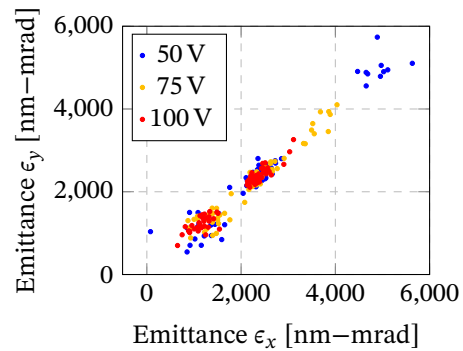
(d) Emittance with regards to voltage

Figure 3.14: Focus on 250 nm emitter, pulse widths 160 fs and 4000 fs, the emittance ϵ_x and ϵ_y is plotted against each other.

30

Chapter 4

Photoemission from GaAs:Ge structures

Initial work on photoemitting cathodes was performed in a vacuum with a custom-made measurement setup consisting of a circular anode and an ultraviolet diode. Preliminary results were inconclusive and no emission was detected. Several different target materials were tested. The main criteria for potential candidates were that their workfunction should be just suitable to allow for emission with the lased-diode used. Ideally, the emitted electrons should have low or zero initial velocity (thus, practically no kinetic energy). The first promising cathodes were annealed p-type GaAs from previous work with SiGe of Sultan *et al.*[84]. This triggered studies on long series of photoemission measurements on annealed n and p-type, GaAs and GaAs:Ge, to determine the relationship between surface structures and photoemission.

4.1 Materials and Methods

The original focus was on cathodes made with deposition of Ge on (100) and (001) p-type (Zn-doped) GaAs wafers to determine which surface structures were the main cause of photoemission characteristics. The samples were approx. 10 mm × 10 mm squares of GaAs wafer. Prior to deposition, the samples were sequentially cleaned with acetone, methanol, isopropanol, rinsed with de-ionized water and blow-dried with nitrogen gas.

The samples in this series were coated with a thin film of Ge, roughly 10 nm, as determined via Xray-reflectometry before the annealing process. The Ge-layer was prepared by sputtering from a Ge-target of 99.999% (5N) purity, using direct current magnetron sputtering (dcMS). Advanced Energy MDX500 power supply was utilized in the dcMS deposition. During deposition, the target was positioned at 45ř relative to
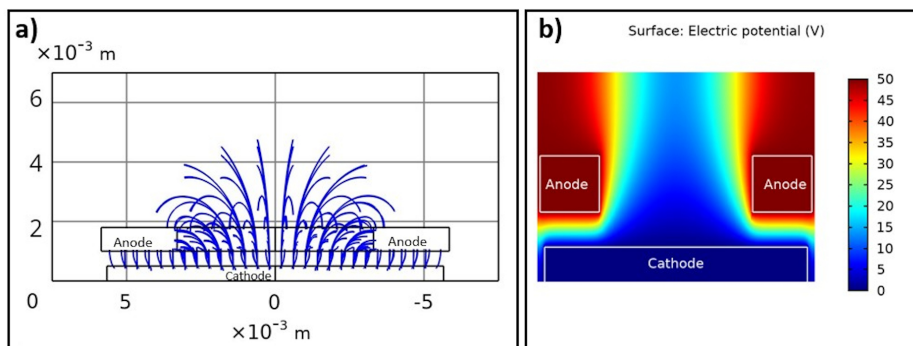
Figure 4.1: Cross-sectional view of the measurement configuration, a) shows projected paths of electrons coming out of the photocathode while b) shows the calculated electric potential around the setup.

the sample with a distance of 200 mm and continuously rotated to maintain uniform deposition. Deposition chamber pressure was set to 5×10^{-7} Pa. Argon (Ar) gas of 6N purity was used as a working gas with a flow rate of $q_{Ar} = 100$ sccm and power was maintained at 30 W.

Two different types of thermal treatment were used after Ge deposition; annealing in a conventional resistance-heated furnace and a rapid thermal annealing (RTA). The former one, conventional furnace annealing (CFA), was done in air ambient using Heraeus D-6450 Hanau furnace. An alumina tube was inserted into the furnace which was then brought to the desired temperature and maintained there for a more uniform temperature. Samples were inserted into the alumina tube using a sliding rod, positioning them in the center of the furnace, for approx. 30 min to 60 min. After annealing, the samples were pulled out from the alumina tube and cooled down at room temperature. The second type of thermal treatment, RTA, is based on flash heating with flash lamps, allowing much faster heating than by a conventional furnace. The time span of the RTA was 10 s to 90 s, performed in a Jipelec™ JetFirst 200 chamber in nitrogen ambient.

4.1.1   Characterization

Microstructures on the samples' surfaces were characterized with scanning electron microscopy (SEM) and atomic force microscopy (AFM), from ZEISS (Supra 35) and Park System (PSIA XE-100) respectively. Elemental analysis was done via electron dispersive X-ray spectroscopy (EDX) by ZEISS Supra 35 add-on.

Photoemission measurements were performed using custom-built equipment, measuring current with an applied bias voltage ranging from −5 V to 250 V. The
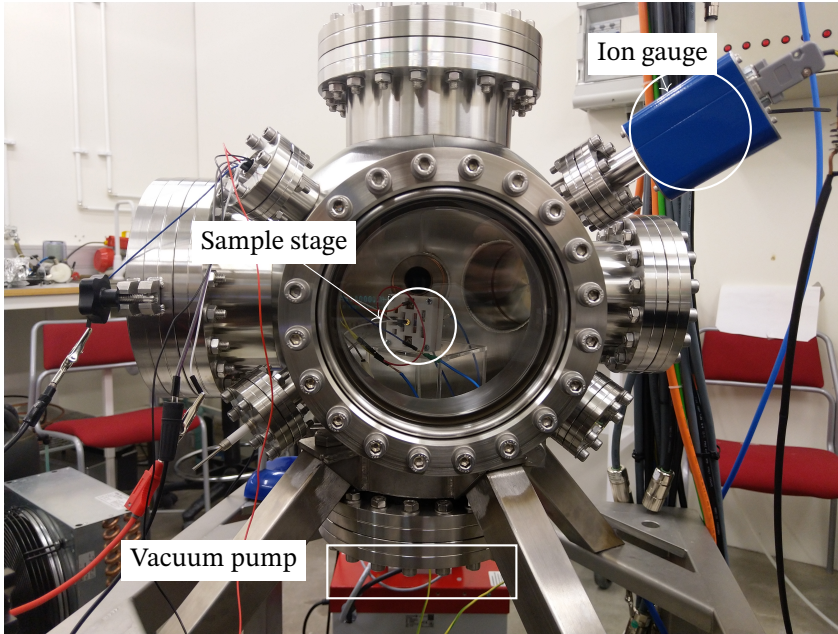
Figure 4.2: Spherical Vacuum chamber, the white box in the center is one of the custom built measurement stages, in the center (golden spot) is a UV LED. Vacuum pump can be seen below the chamber, the Pirani gauge is on the far side.

instruments consisted of a Keithley 2400 source-meter connected to a sample stage, with a cathode-anode distance of approx. 500 ţm. A computer-controlled 16 mW UV-LED from Boston electronics was used as a light source. The UV-LED wavelength of 265 nm, or 4.68 eV, was picked to match the work function of GaAs (4.6 eV), as to minimize the velocity of ejected electrons. During measurements, the samples were placed in a vacuum chamber with 10 mPa pressure or less. The instruments, anode, cathode, UV-LED and source-meter were connected through an 8-point feed-through on the vacuum chamber. Gold (Au) electrode with dimension of 1 mm×3 mm and 150 nm in thickness was deposited on the edge of the GaAs:Ge samples via e-beam evaporation (Polyteknik Cryofox Explorer 500 LT). Connection to the sample's electrode's was made with thin Al wire (25 ţm) attached with Ag-paste, see Figure 4.3.
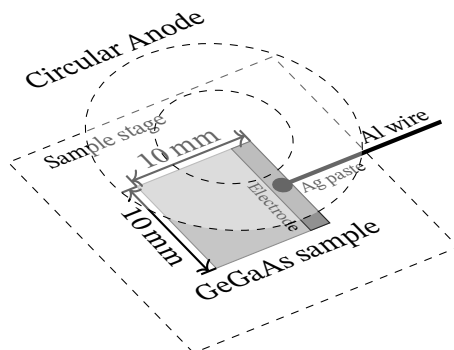
Figure 4.3: Schematic of a typical sample on stage, electrodes on the side, connected to a source-meter with Al wire and Ag paste. The circular anode is directly above with UV-LED illuminating through the center.

4.2   Results and discussions

The main emphasis here is on photoemission, while detailed structural analysis can be found in the related publications [2], [3].

4.2.1   Conventional furnace annealed samples

The photoemission current versus bias voltage from the furnace annealed GaAs:Ge samples can be seen in Figure 4.4. Temperature is increased in steps of 50 °C from 400 °C to 750 °C and the annealing time is kept constant at 60 min. The photoemission curves have the dark-current subtracted from the current measured under illumination as to reduce possible noise. Figure 4.5 shows current vs annealing temperature at bias voltage of 50 V for samples annealed for 10 min and 30 min. The value of 50 V was selected since at this voltage emission has passed the threshold level seen in Figure 4.4 and are in a stable region. With increased annealing temperature, the PE slowly increases with the peak emission occurring at 650 °C, after which it starts to decrease. The sharp rise in the PE curves up to about 15 volts before tapering off is attributed to the illuminated area directly beneath the anode, where the electrons are caught by the potential field immediately. The slow increase after the initial rise can be attributed to the toroidal geometric shape of the anode, where some electrons can escape through its center, and with more of them being pulled in towards the anode as the bias voltage is increased. This is visualized in Figure 4.1 showing electrons escaping through the center of the toroidal anode while those directly underneath will still be captured by the relatively weak electric field.   The origin of the enhanced photoemission is yet unclear, however it is related to the presence of GaAsO islands on the surface. One can not exclude the possibility that the
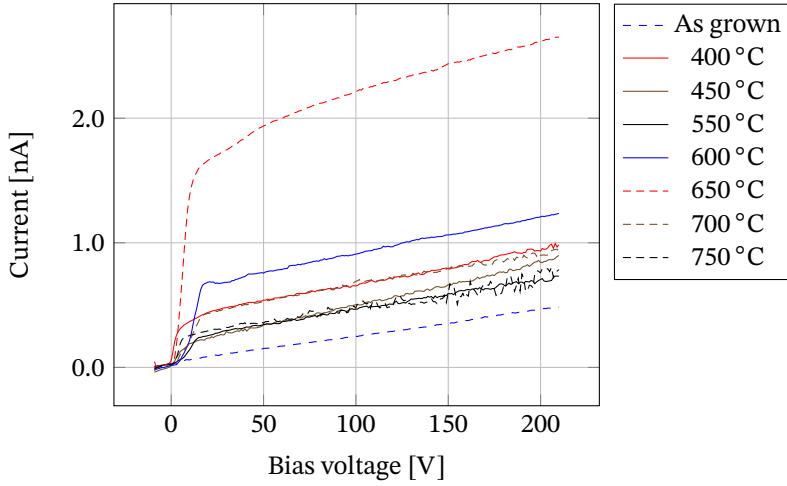
Figure 4.4: Photoemission from CFA GaAs:Ge samples, 60 min annealing time, 400 °C to 750 °C
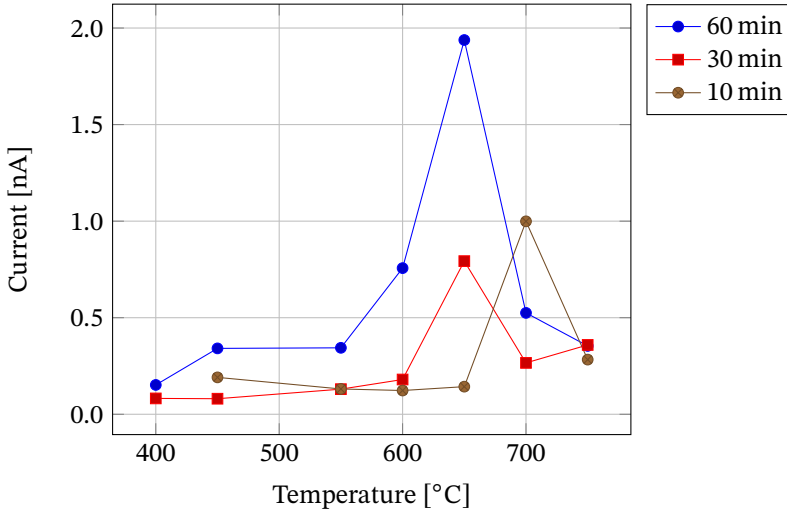
Figure 4.5: Photoemission from CFA GaAs:Ge samples, showing emission at 50 V, note the peak at 650 °C for both 60 min and 30 min that shifts to 700 °C for the shortest annealing time of 10 min

surface properties (defects, dangling bonds) of these GaAsO islands could influence
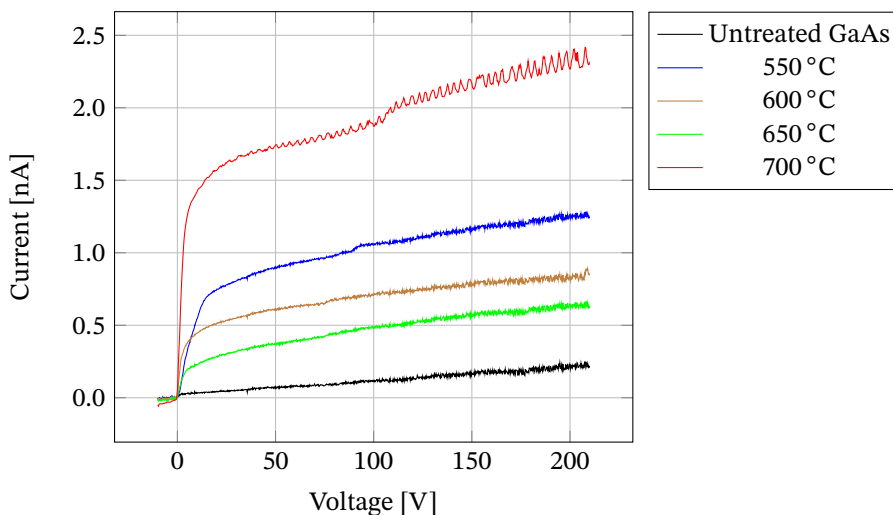
Figure 4.6: Photoemission from RTA GaAs:Ge samples, 1 min annealing time, 550 °C to 700 °C

the photoemission characteristics.

Increasing annealing temperature above 650 °C the effect is reversed. The formation of nanopits, occurring at higher annealing temperature, deteriorated the photoemission characteristics. Increasing annealing time while keeping the temperature constant followed a similar path, resulting in reduced photoemission.

This difference in photoemission can in part be explained by viewing SEM and AFM images of the samples. There is no visible formation of nanostructures on the low end of the annealing temperature scale until 600 °C, where formations of small nanoislands started to appear. At 650 °C the nanoislands are larger in size and higher photoemission current observed. Exceeding this annealing temperature caused a significant drop in emission. It is apparent from the images that nanoislands are larger but with lower density accompanied with higher density of nanopits. This suggests that the emission characteristics is heavily influenced by the nanoisland's sizes and densities [85], [86]. Another factor that may contribute significantly to the emission characteristics is the evaporation of As from the GaAs substrate. Arsenic has much higher vapor pressure than gallium and thus, the ratio of As-vacancies grows with temperature. An increase in As-vacancies ratio on the surface initially contributes to increased emission, increasing temperature above 650 °C results in Ga-droplets turning into nanopits [87]–[89]. This results in reduced carrier mobility, altered band-gap, and increased oxygen contamination, all of which reduce the emission current [90]–[96].
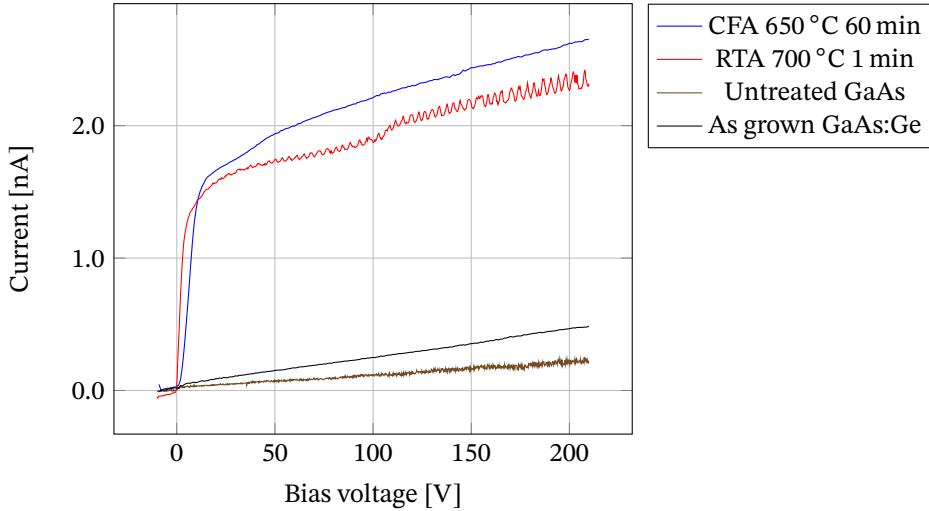
Figure 4.7: Comparing Photoemission from GaAs:Ge samples, 650 °C CFA and 700 °C RTA for 60 min and 1 min annealing time respectively, with that of untreated GaAs and as grown GaAs:Ge

4.2.2 Rapid thermal annealed samples

Furthermore, from experiments with RTA at 550 °C to 700 °C for 60 s on (001) GaAs with Ge coating, it can be seen (Figure 4.6) that it exhibits almost two orders of magnitude higher emission than untreated substrate of GaAs. This can be attributed to formation droplets on the surface, creating Ga protrusions with lower work function [2]. These Ga droplets and the GaAsO islands from the CFA threated samples correlate with higher photoemission. Figure 4.7 compares photoemission of GaAs:Ge samples, furnace annealed and rapid thermally annealed for 60 min at 650 °C, and 1 min at 700 °C, respectively, to that of untreated, bare GaAs substrate and Ge-deposited GaAs. It is apparent that the basic substrate barely shows any emission and the untreated GaAs:Ge shows just marginally higher emission. Investigation of prolonged exposure to heat from the LED on the structural stability of the samples was done by running measurements for four consecutive days. The temperature measured at the sample, using color-changing stripes attached to the sample, was determined to be less than 100 °C. No change in surface morphology and negligible changes in chemical composition was observed, exemplifying the stability of the samples.

Cesium (Cs) metal is the element with the lowest work-function and consequently it is frequently used in commercial photoemission lamps. Cs is also one of the most reactive element in the periodic table, making it very difficult to handle in pure form. It is of interest to compare the emitters made here to such lamps (diodes), for example

cesiated GaAs, which has negative electron affinity (NEA). The quantum efficiency of those is prone to degradation from vacuum poisoning and/or back-bombardment of ions during operation [94], [97]. They furthermore suffer from being volatile, with a limited lifetime and requiring regular renewal of Cs, which is the trade-off for higher energy photons needed for emission, requiring extremely high vacuum to minimize the reaction with residual gases for longer operational time [98]. This is very much in contrast with the photocathodes (photoemitter) presented here as they are operational at low vacuum levels and show little if any deterioration on the photoemission characteristics from storage at room temperature in atmospheric ambient. While NEA sources require complex setups for fabrication and packaging, the nanostructures presented here are simple and cost effective on small scale photoemitters. Further analysis is needed to improve the structural stability and emission output, as well as quantum efficiency measurements over a wider spectrum.

Chapter 5

Piezoresistance and pressure effects in SiNWs

Nano-structured material like silicon nanowires (SiNW) exhibits qualities quite unlike its bulk counterpart. SiNWs have different mechanical, electrical, optical, and thermoelectric properties that makes them valuable in advanced technology such as sensors and heat salvagers [99]–[103]. The well established industry around silicon based electronic devices favors developments in SiNWs as they make use of technology and infrastructure that is already in place. Doped silicon is known to exhibit high piezoresistance effect due to change in electronic band structure and effective mass of charge-carriers [28]. The piezoresistance effect is used in many devices today, for example pressure transducers, atomic force microscope cantilevers, biosensors, and transistors [104]–[108]. Silicon nanowires have specifically shown this effect in greater magnitude when p-doped while n-type shows little additional response over bulk [29], [37], [109]. The origin of the piezoresistance effect has not been firmly established with several theories explaining in part with quantum confinement effects, surface charge effects, strain-induced bandgap shift, or change in effective mass of charge carriers [30]–[36].

Silicon nanowires can be fabricated by several different methods such as vapor-liquid-solid, laser ablation, and metal-assisted chemical etching (MACE). Of these methods, MACE is the simplest and has been widely used [110]–[115]. This method works with wet chemical etching in conjunction with a thin film metal pattern or nanoparticles, usually made of gold or silver, deposited on the silicon wafer, assisting with anisotropic etching of the silicon oxidized surface [5], [116], [117]. There have been very few studies made on SiNW arrays undergoing isostatic pressure change [34], [38].

In this chapter the results from measuring electrical characteristics of SiNWs, fabricated with MACE, in a vacuum and a pressure chamber to perform isostatic
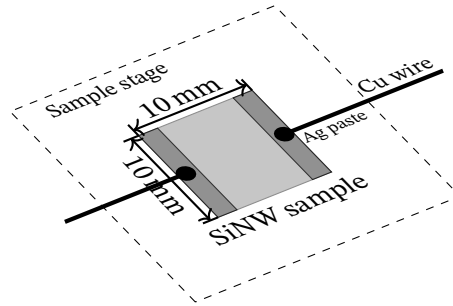
Figure 5.1: Schematic of a typical sample, electrodes on two sides, copper wire and Ag paste on electrodes in overpressure case. Fixed 5 V bias voltage applied.

load distribution on the sample surface will be presented.

5.1 Materials and methods

5.1.1 Fabrication of SiNWs

The MACE method was used to create bundles or forests of interconnected SiNWs with an area of $1\,cm^2$. Silver (Ag) nano-particles were deposited on a polished surface of a p-type, 525 ţm thick silicon wafer, with resistivity of $10\,\Omega\,cm$ to $20\,\Omega\,cm$, by submerging the wafer in a solution of 3 M HF and 1.5 M $AgNO_3$ for 60 s. Directly after, the samples were etched in a $HF:H_2O_2$ (5M:0.4M) solution for 40 min, leaving behind vertical silicon-nanowire bundles. To remove silver particles afterwards, the samples were submerged in 20 % w/v HNO_3.

Two 150 nm thick aluminum (Al) stripes, 2 mm × 10 mm, were deposited with e-beam evaporation (Polyteknik, Cryofox Explorer 600 LT) on top of the samples on each side of the SiNWs area (a co-planar configuration).

A SEM (Zeiss-Supra 35) was used to characterize the SiNWs geometry. The length and average diameter of the wires were estimated from top and cross-sectional SEM images. The Gwyddion software for data visualization and analysis was used to estimate the cross-sectional area of the wires from the SEM images. By using the average number of wires from several line-scans, an estimation of approximately $1.6 \times 10^7\,mm^{-2}$ was obtained, whose cross-section accounted for roughly 28 % of the total cross section. This corresponds to roughly 9.6×10^8 wires on an area of 6 mm × 10 mm exposed to air during the isostatic pressure cycle.

Length of the wires should be relatively homogeneous, with estimated length of around 10 ţm and diameter of approximately 150 nm.

Figure 5.2: The same spherical Vacuum chamber as described in chapter 4, vacuum pump can be seen below the chamber, the Pirani gauge is on the far side.

5.1.2 Measurement setups

Electrical measurements were performed in two separate chambers, a spherical vacuum chamber from Kurt J. Lesker and a custom built pressure chamber. A HiCube 80 Eco vacuum pump from Pfeiffer was used on the vacuum-chamber, and the pressure was measured with combined KJLCő 923 Series Hot Filament Ion Gauge / Convection Enhanced Pirani. A Timbertech air compressor was used on the pressure-chamber and the pressure was measured with a conventional pressure gauge. A Keithley 2400 and 2470 Sourcemeters were used to measure the resistance through the sample as a function of time, at a constant bias voltage of 5 V. The samples were mounted on a fixed platform inside the chambers. For the measurements in vacuum, a tungsten needle-tip kelvin-probes were used while fixed copper wire connections were used to measure in the pressure chamber as shown in Figure 5.1. Pressure-chamber connections were coated with small drop of electrical Ag-paste to insure stability with aluminum electrodes, this point becomes important later. Extra care was made such that the nanowires had maximum surface area exposed to air. All measurements were performed with ambient air as pressure medium.
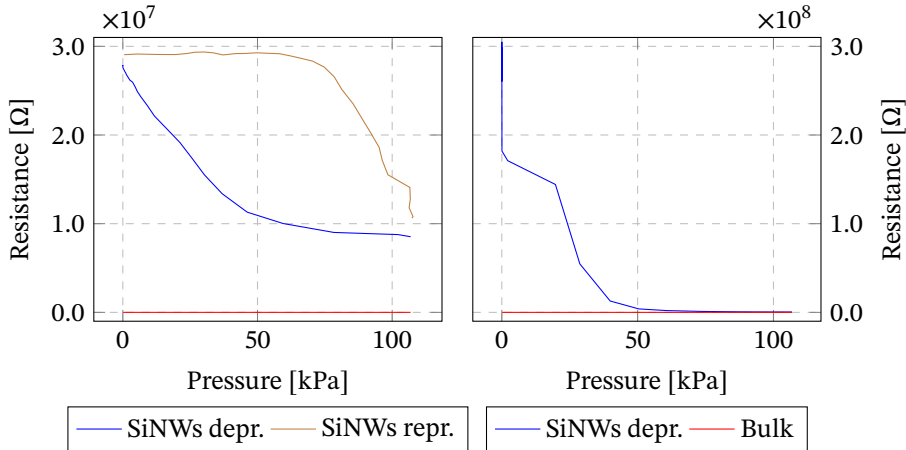
Figure 5.3: Using fixed 5 V and reducing the pressure from 0.1 MPa to 0.1 Pa the resistance increased, with the highest sensitivity from 50 kPa to 20 kPa. The sensitivity is not the same during the pressure cycle, indicating a delay or capacitative effect as the air is removed and added. The graph on the right is from the published paper [4].

5.2   Results and discussions

The piezoresistive effect in silicon and SiNWs is well-known and widely studied [28], [38] but mainly in individual wires and for uniaxial pressure. Collective properties of surface bunches or forests of nanowires during isostatic pressure change is however still unclear. In this section, the measured electrical effects of isostatic pressure change on SiNWs will be presented, both for vacuum and overpressure.

5.2.1   Reduced isostatic pressure effect on resistance

The first measurement was performed in a vacuum chamber, measuring the piezoresistance response to reduced pressure. The pressure was reduced from 100 000 mPa to 10 mPa in the vacuum-chamber under depressurizing condition and then back to 0.1 MPa again, under re-pressurizing condition. Some results are shown in Figure 5.3 along with results presented in related publication [4]. The resistance is plotted as a function of the pressure measured at a fixed bias voltage of 5 V. From the published source, a large increase in resistance, more then two orders of magnitude during the depressurization can be seen (brown line) which is significantly higher than for bulk Si. Moving the needle tip to a different location on the samples yielded a somewhat different resistance, though within the same order of magnitudes as before. This variation indicates that the Al-electrode is not uniform across the wires, creating local electrode "islands" within the SiNW's forest. It should be noted though, that in
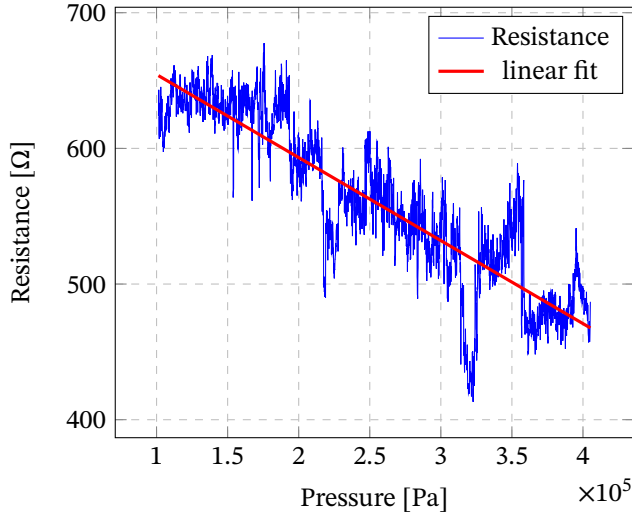
Figure 5.4: With fixed 5 V across the sample, starting at 0.4 MPa and reducing until atmospheric pressure is reached at 0.1 MPa. The resistance increased as the pressure drops, reducing conductivity with lower concentration of ions. The high noise could be attributed to the current finding new paths through the ever changing nanowire forest.

spite of the variation with the needle's position, a clear piezorestive effect was always observed, although its magnitude did vary. The piezoresistance change with pressure can be attributed to mechanical, chemical and physical effects. As the pressure drops, the mechanical stress is reduced and the removal of atmospheric air may affect physi and chemisorption processes. The re-pressurizing line in Figure 5.3 shows the same effect in opposite order; when the air is re-introduced, the pressure or density needs to reach a certain level before the resistance drops back to initial level. This indicates a need for a specific amount of surface adsorption, either physisorption or chemisorption, before conductivity is restored. Such capacitative effect results in time-dependent hysteresis.

5.2.2 Effect of isostatic pressure on resistance

Increasing pressure above atmospheric level (see Figure 5.4), had similar effect as observed in Figure 5.3 only in a more linear fashion, though the effect were not as pronounced, and limited by high noise-level. The observed results of decreased resistivity with increased pressure can be explained on the basis of surface adsorption/desorption.
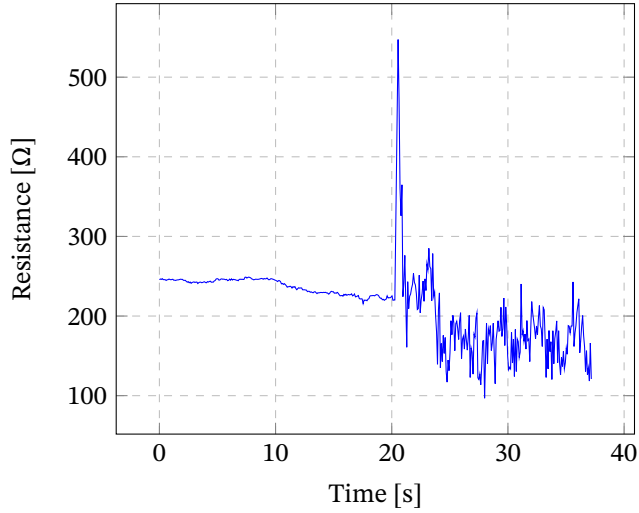
Figure 5.5: Sourcing 5 V for 20 s at atmospheric pressure and then turning off the source. The nanowire pattern, while under voltage bias, shows slight increase in resistivity that disappears when bias is removed, reverting back to substrate resistivity.

Increased pressure should lead to higher density of ions on the surface of the nanowires and consequently the current finds more paths to travel [118]. These constant changes in path-finding significantly increase the noise-level of the current, unlike for the vacuum case where removal of air closes the possible paths.

Noteworthy, one other effect related to the electrode connections was observed; adding a small drop of silver-paste used onto the copper wires at the electrodes, resulted in a significantly higher conductivity at atmospheric pressure. This further confirms that the Al-electrodes, deposited on the wires, are indeed not uniform and that connections to the wires are concentrated at the top, leaving unconnected islands or bundles. With the Ag-paste, connecting now to multiple bundles of wires, the resistance is reduced due to now larger cross-sectional being in contact, as described by

$$R_\Omega = \rho_\Omega \frac{l_\Omega}{A_\Omega} \, , \tag{5.1}$$

where R_Ω is the resistance, ρ_Ω is the electrical resistivity, l_Ω is the length of resistor and A_Ω is the cross-sectional area. Calculating this for the area with given values for the pressure-chamber connection, gives an area of a approximately $7\,\text{mm}^2$ to $15\,\text{mm}^2$, which would fit for a small droplet. Doing the same for the vacuum connection, with the tungsten needle, yields an area of approximately 11 ṭm, which is very close to given specifications of the needle point. This would exclude the electrodes as a cause

of resistance change, leaving adsorption and piezoresistiviy effects as main causes for variation in resistance during the isostatic pressure change. It further supports results from a related study on arrays of periodic nanowires where resistance drops with increased pressure (see Supplementary [4]), even with different configuration of electrodes (top and bottom configuration instead of co-planar as presented here).

5.2.3 Conclusions and suggestions

The SiNWs exhibited high PZR sensitivity to isostatic pressure at low pressure level (below atmospheric pressure) but little sensitivity above atmospheric pressure.

A possible reason is that dangling bonds of the SiNWs surfaces attract atmospheric ions, possibly by physisorption (van der Waals forces), thereby affecting the conductivity. When the air is removed by the vacuum pump, the ions slowly migrate away, leaving the nanowires bare, reducing the conductivity through the nanowire forest. When air is let in again, there is a delay in PZR response as the nanowires require a certain amount of ions in order to reach the same conductivity as before.

By geometrically designing the SiNW, the electrode surface-area and its contact size, the SiNWs, presented here, hold potential as a tunable high sensitivity pressure sensor with further work on memristive and asymmetric sensor development.

46

Chapter 6

Summary

This chapter contain a summary of the three research projects presented in the thesis.

6.1 Photoemission from GaAs:Ge

The effects of nanostructures on photoemission, were studied made by annealing Ge on GaAs surface. Both CFA and RTA methods were used, formation of nanostructures began at 550 °C, both reaching an optimum at 650 °C and 60 min, 1 min, respectively with regards to photoemission. SEM and AFM analysis showed gradual formation of nanoislands enriched in Ga, and nanopits deficient in Ga and As. Ratio of nanopits and nanoislands, with respective elemental composition were one observable factor on photoemission characteristics, high density nanoislands and low density of nanopits giving almost an order of magnitude better outcome, with other possible factors potentially playing a role, the reason remains uncertain. Eventual oxidation at higher temperature deteriorates the photoemission characteristics. Although materials with negative electron affinity can emit electrons using lower energy photons, the volatility, limited lifetime and regular renewal of Cs used, being the trade-off for higher energy photons needed for emission. The Cs-O activated GaAs photocathodes have a limited lifetime due to vacuum poisoning, requiring extremely high vacuum to minimize the reaction with residual gases for longer operational time [98] This is very much in contrast with the photocathodes presented here as they are operational at low vacuum levels and show little if any deterioration on the photoemission characteristics from storage at room-temperature in atmospheric ambient.

6.2   Photoemission Simulations

Using MD-Simulations the transition from source limited emission to space-charge limited emission in photo-emitted electron beams in a microscopic diode for different values of laser pulse-width, intensity, emitter area (or spot size) and accelerating potential was examined. The conventional capacitive models of short-pulse electron bunches may considerably underestimate their total charge due to neglecting two-dimensional space-charge effects, whereas the estimates for the short-pulse space-charge limited current using the approach of Koh and Ang shown in Equation (3.9) give a reasonably accurate estimate for the maximum current induced by a electron bunch transiting the diode gap. Parameters for optimal brightness of the beam bunch were identified. In the parameter range that was studied, the highest value of brightness was found to occur when the charge in the beamlet is roughly 40 percent of the critical charge for formation of virtual cathode. This result is similar to what has been found for thermal emission in microdiodes, in that optimal brightness is achieved at a point during transition from source-limited to space-charge limited emission. This may have some practical value for designers of electron sources for coherent and time resolved electron beams.

6.3   Piezoresistance in Silicon nanowires

The isostatic pressure variation on silicon nanowires shows their sensitivity to vacuum while pressure above atmospheric has limited effect. The proposed reason are surface bonds of the silicon nanowires being saturated by atmospheric ions, possibly by physisorbtion and the van der Waals forces or chemisorption, making them more electrically conductive. When the air is removed by the vacuum pump the ions slowly migrate away, leaving the nanowires isolated, reducing the conductivity through the nanowire forest. Then when air is let in again there is a delay as the nanowires require a certain amount of ions back to reach the same conductivity as before, this would be a function of surface area and mean distance between wires.

   This has potential with deliberate design of electrode surface area and contact size with the silicon nanowires could be used as tunable pressure sensor with further work on high-sensitivity, memristive and asymmetric sensor development.

Paper I

Simulation of short pulse photoemission in a micro-diode with implications for optimal beam brightness

Hákon Örn Árnason, Kristinn Torfason, Andrei Manolescu, and Ágúst Valfells

Department of Engineering, Reykjavik University, Menntavegur 1, IS-102 Reykjavik, Iceland.

Molecular dynamics simulations, with full Coulomb interaction are used to model short-pulse photoemission from a finite area in a microdiode. We demonstrate three emission regimes, source-limited emission, space-charge limited emission for short-pulses, and space-charge limited emission for the steady state. We show that beam brightness is at a maximum during transition from the source-limited emission regime to the space-charge limited emission regime for short pulses. From our simulations it is apparent that the important factor is the emitter spot size when estimating the critical charge density for short-pulse electron emission.

I. INTRODUCTION

Short pulse electron beams are important in many applications, e.g. high power microwave sources for hundreds of GHz and THz [1], time resolved electron microscopy [2, 3], and free electron lasers [4]. Ideally these bunches should be coherent and have high current, a characteristic which can be quantitatively measured in terms of the beam brightness. In this paper we use the following definition of brightness from Reiser [5],

$$Br = \frac{\eta I}{\epsilon_x \epsilon_y} \propto \frac{I}{\epsilon^2} \ ,\tag{1}$$

where η is a geometric constant equal to $2/\pi^2$, I is the current along the beam direction, z, and $\epsilon_{x,y}$ are the emittances in the transverse directions, x and y, describing the lateral spread of the beam in the phase space [6, 7], which are expected to be equal for a beam with transverse symmetry.

High current and low emittance are somewhat competing goals, as high current beams are subject to space-charge forces that lead to increased emittance and also because high current generally implies high electron density near the cathode that leads to increased scattering and consequentially higher emittance [8]. This trade-off between current and emittance suggests that an optimal value of brightness exists. In fact, this has been observed for pulsed photoemission, both experimentally [9], and from simulations [10]. Optimal brightness is not limited to pulsed photoemitted beams. For instance, it has been observed in simulations of thermal emission in microdiodes, that optimal brightness is obtained during the transition from source limited emission to space-charge limited emission [11]. The work presented in this paper was initiated as a study of the corresponding transition to space-charge limited photoemission from a planar cathode.

For that purpose we use a high-fidelity molecular dynamics code we have developed, called Reykjavik University Molecular Dynamics for Electron Emission and Dynamics (RUMDEED) [11, 12], including discrete particle emission, scattering, and space-charge effects on electron emission and propagation, to model the physics of electron beamlets near the cathode. This includes emission, propagation and effects on derived parameters such as pulse charge, emittance, and particularly brightness. We investigate the transition from source limited to space-charge limited emission and show how optimal brightness can be obtained with regard to nonlinear physics in the vicinity of the cathode.

There are a number of sources of emittance growth that can diminish the brightness of a beam as it propagates through a device due to effects such as misalignment of focusing and accelerating components, beam mismatch, nonlinear forces, etc. [5]. However, it is useful to look carefully at what is happening at the cathode and in its immediate neighborhood for a better understanding of ultimate limits to brightness. The purpose of this paper is to isolate space-charge and discrete particle effects on photoemission of electrons and their propagation in the immediate vicinity of the cathode, how the transition from source limited emission to space-charge limited emission happens, and to show how that affects the beam brightness. To do so we use a model that does not incorporate cathode temperature, surface protuberances, or variable work function on the cathode surface. We will also compare our results on the transition from source limited emission to space-charge limited emission to commonly used models.

II. METHODOLOGY

In this paper the molecular dynamics computer simulation (MDCS) method is being used to investigate how the electron beam evolves with regards to emitter size, width and amplitude of the photon pulse, and applied potential. The MDCS method is well suited for a system with a relatively small number of particles. Our system is an infinitely wide vacuum diode, with the anode-cathode gap spacing denoted by D, zero voltage at the cathode, and applied voltage V at the anode. The emission area is a disk with radius R which is smaller than D. The work function of the emitter ϕ is uniform over the area
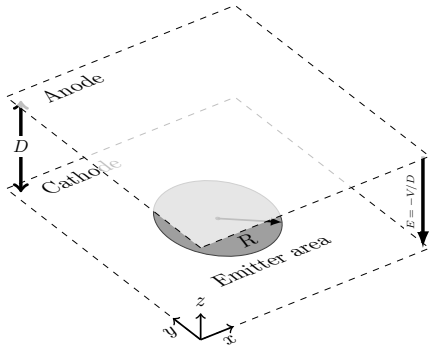
FIG. 1. Simulated vacuum diode system model, circular emitter area with radius R, gap size D is 2500 nm and applied potential V.

and equal to average energy of the photons.

The photons in a pulse have energies E, with a Gaussian distribution, with average $\langle E \rangle = \hbar\omega$, and with a very small standard deviation $\sigma_E \ll \hbar\omega$. The number of photons N within the pulse have also a Gaussian distribution, but as a function of time. The time is discretized in small steps δt, the width of the pulse is σ_N time steps, and in practice the total duration of the pulse τ_p is assumed equal to $16\sigma_N\delta t$.

The electrons are emitted with the initial velocity v_{z0}, corresponding to the excess energy transferred by the incoming photon and the emission occurs in the direction normal to the surface of the emitter,

$$v_{z0} = \sqrt{2(E - \phi)/m} \, , \qquad (2)$$

where m is the electron mass. The dispersion of v_{z0}, due to the small dispersion of the photon energy, is obviously also small. The number of emitted electrons is a function of time, and it follows the Gaussian photon pulse. At each time step the theoretical (or virtual) number of electrons that could possibly be emitted is modeled as a Poisson random variable, with an expected value given by the quantum efficiency (QE) multiplied by the number of incoming photons during that time step, which in fact is the average number of emitted electrons in the absence of an electric field and space-charge effects [13]. Although the pulse duration is short, below 1 ps, we neglect possible multiphoton emission events. In our numerical implementation the pulse intensity is described by the amplitude of the virtual electron pulse emitted by the cathode (i.e. the mean value at the middle of the pulse), which is an input parameter that we refer to as the scaled laser amplitude. The mechanism of electron ejection from the cathode including the space-charge effect due to the already emitted electrons is implemented in our code and was used in previous work [12, 14–18]. The algorithm selects an emission site randomly within the circular emitter area of the cathode. First, the energy of

the photon is compared to the work function at the site to see if emission is possible. Then, if the electric field at that site favors the emission, i.e. it is oriented such that the force on the electron would accelerate it towards the anode, a second check is made at 1 nm above the cathode, and if the field there is also favorable, an electron is placed 1 nm above the cathode surface and given velocity according to eq. (2). If neither the work function or the local electric field at the candidate site is favorable, no electron is placed outside the cathode, and a failure of the emission event is recorded. This process is repeated until either the maximum number of emitted electrons allowed by the Gaussian pulse at that time step, or 100 recorded failures to place, have been reached. With the Gaussian limit not being reached, or ultimately with no favorable site for emission, will indicate the space-charge limited regime. This mode of electron placement ensures a self-consistent current density over the emitter cathode, whether source limited or space-charge limited.

The next step of the simulation is to calculate the net forces acting on every electron due to the direct Coulomb interaction with the other electrons in the system, including the image charge partners outside the boundaries of the simulation box, and due to the accelerating field created by the anode. Then the time step is advanced and the Velocity-Verlet algorithm is used to calculate the new positions and velocities of the electrons. Electrons that pass the boundaries of the anode or cathode are recorded and removed from the system. The simulation works through the process of electron emission and advancement for each time step until a user selected end point. The total current through the diode is calculated using the Ramo-Shockley theorem [19, 20],

$$I = \frac{q}{D} \sum_i v_{iz} \, , \qquad (3)$$

where q is the electron charge, and v_{iz} the component of the instantaneous velocity of the electron i, that is normal to the cathode surface (i.e. in the z direction).

In order to observe the effect of pulse relatively to the entire system size, we normalize the pulse width τ_p with the transit time of a single electron from the cathode to the anode,

$$\tau = D\sqrt{\frac{2m}{qV}} \, , \qquad (4)$$

yielding $\tau_n = \tau_p/\tau$, or

$$\tau_n = \frac{16\sigma_N\delta t}{D}\sqrt{\frac{Vq}{2m}} \, . \qquad (5)$$

Thus, if the duration of the laser pulse is equal to the time it takes for a single electron to be accelerated from the cathode to the anode then $\tau_n = 1$.

In the interest of calculating the brightness defined in eq. (1), we use the maximum value of the Ramo-Shockley

current given by eq. (3), and the statistical emittance, appropriate for our computational approach [21],

$$\epsilon_x = \sqrt{\langle x^2 \rangle \langle x'^2 \rangle - \langle xx' \rangle^2} \qquad (6)$$

with x denoting the position and $x' = dx/dz = v_x/v_z$ being the deviation angle of the particle in the x direction. The angular brackets represent averages over all electrons when they pass through the anode. The corresponding similar formula is used for the y direction.

The numerical values of the parameters used in the simulations are: The radius of the disk-shaped emission area of 125, 187.5, 250 nm; the distance between the cathode and the anode $D = 2500$ nm; the anode-cathode potential difference of 50, 75, 100 Volt; the simulation time step $\delta t = 0.25$ fs with the total running time of 15 ps; the center of the emission pulse 5 ps with amplitude 1, 2.5, 5, 10, the average number of electrons at emission peak and pulse width from 4 fs tp 4000 fs; mean energy of photons 4.7 eV with a standard deviation of 0.02 eV; the work function of the material was chosen to be 4.7 eV, approximating copper as cathode material.

III. RESULTS AND ANALYSIS

We begin by looking at the current induced in the diode as a function of time, as shown in Fig. 2. Here we see different values of the pulse width, $\tau_{\rm p}$, while the gap voltage is fixed at 75 V, and the emitter radius and amplitude of the laser pulse are held constant as well. Recall that the peak of the laser pulse is located at time $t = 5$ ps, and note that the transit time for a single electron across the diode gap for the given voltage is $\tau = 0.97$ ps. In the case of $\tau_{\rm p} = 60$ fs, emission is source limited and the charge is emitted in a tight bunch at approximately 5 ps. This bunch of charge is subsequently accelerated across the gap by a nearly constant applied electric field, resulting in an induced current that grows linearly with time until the foremost electrons in the bunch are absorbed by the anode, at which time the induced current begins to drop due to absorption of charge. In the case of $\tau_{\rm p} = 400$ fs, emission is space-charge limited and begins slightly prior to the 5 ps mark but nonetheless manifests as a bunch of electrons that are accelerated across the diode gap leading to linear growth of the induced current in time until the leading electrons are absorbed at the anode. From the figure it is apparent that the bunch length is greater for the wider laser pulse as would be expected.

In the conventional analysis of the Child-Langmuir current it is implicit that the current is constant in time for fixed external parameters [22]. As the width of the laser pulse is increased so as to exceed the transit time across the gap, we see a transition in the current profile as a function of time when looking at Fig. 3. For long values of the pulse length the rise in the current is no longer linear, as one would expect for a short electron bunch, but has a steadily increasing gradient due to the fact that the number of electrons being emitted from the cathode
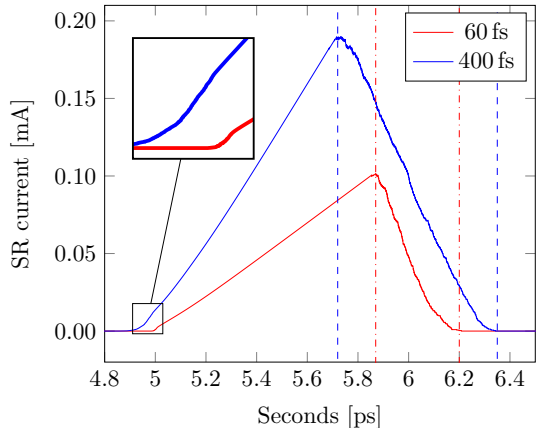
FIG. 2. Temporal profile of induced current for two different laser pulse widths (400 fs in blue, and 60 fs in red). Gap voltage is 75 V, emitter radius of 250 nm, Scaled laser amplitude of 10. Dashed and dashdot lines indicate when first and last electrons cross anode.
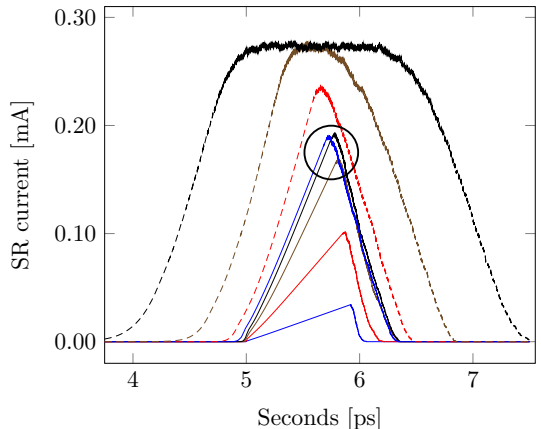
FIG. 3. Temporal profile of induced current for a number of different laser pulse widths ranging from 20 fs to 4000 fs. Gap voltage is 75 V, emitter radius of 250 nm, Scaled laser amplitude of 10. The lowest peak current is on the trace for smallest pulse width. The circle surrounds peaks of traces for pulse widths ranging from 120 fs to 400 fs.

increases gradually with time. We also observe a plateau in the current which occurs once the diode gap has been filled with a steady current. This plateau corresponds to the steady-state space-charge limited current in the diode. Before looking in more detail at how the normalized pulse length affects the current it is worthwhile to look at some common models for analysis of space-charge limited emission from finite area emitters and for

short pulses. Lau [23] devised a simple and elegant theory for steady-state space-charge limited current from a finite emitting area which was later extended by Koh and Ang [24]. From Koh and Ang's work it is expected that the current density from a circular emitter of radius, R, and diode gap spacing, D, when the emission energy is negligible should be:

$$J_{2D} = J_{CL} \left(1 + \frac{D}{4R} \right) , \qquad (7)$$

where J_{CL} is the classical Child-Langmuir current for an infinite planar diode, given by

$$J_{CL} = \frac{4\pi}{9} \varepsilon_0 \sqrt{\frac{2q}{m}} \frac{V^{3/2}}{D^2}. \qquad (8)$$

From this we may calculate the expected steady state current in our system

$$I_{2D} = \frac{\pi}{9} \varepsilon_0 \sqrt{\frac{2q}{m}} V^{3/2} \left(\frac{4R^2}{D^2} + \frac{R}{D} \right). \qquad (9)$$

For short-pulse emission a one-dimensional model (assuming a planar diode of infinite extent) predicts that for a pulse of constant injected current of duration τ_{pulse} there is a critical current density, J_{crit} that is the maximum allowed to ensure that a virtual cathode does not form. In its simplest form, where the bunch of charge is approximated as a single sheet, this critical current density is given by [25]

$$J_{\text{crit}} = \frac{\varepsilon_0 V}{\tau_{\text{pulse}} D}. \qquad (10)$$

This model essentially assumes that for a short bunch, approximated as a single sheet, a virtual cathode will form when the surface-charge density of the sheet is equal to the surface-charge density of the cathode surface due to the applied electric field, namely $\sigma = \varepsilon_0 V/D$. The approximation that, under space-charge limited conditions, the charge may considered to be a single sheet, of the aforementioned surface charge density, transiting the gap in the appropriate time, is called the capacitive model and has been used successfully to derive the classic Child-Langmuir law [26]. The capacitive model for charge density has also been used for analysis of short beam bunches of finite diameter [9].

Let us now look at the current as a function of the width of the laser pulse. Fig. 4 shows how the maximum value of the induced current varies with the normalized pulse length (the ratio of the laser pulse width to the transit time of a single electron across the diode gap). We note that for very short pulse width the maximum current increases proportionally with the normalized pulse length. This is indicative of source limited emission where charge can continually be added to the diode gap in proportion to the rate of photoemission and pulse duration. The growth rate is independent of

applied voltage but dependant on the amplitude of the laser pulse. For slightly longer pulses, that are nonetheless short compared to the transit time, the accumulation of space-charge is sufficient to block further emission of photo-electrons and the current reaches a plateau indicative of space-charge limited emission. This current limit is determined by the applied voltage, but note that for lower laser amplitude a greater normalized pulse length is needed to reach the critical amount of charge in the electron bunch. We can also see that the space-charge limited current is somewhat higher than that predicted by eq. (9). The space-charge limited current observed here corresponds to the maximum current shown within the circle in Fig. 3 for laser pulse width ranging from 120 fs to 400 fs. In Fig. 5 the abscissa has been extended to show values of the normalized pulse width that extend beyond unity. From this figure we can see the transition from the plateau that corresponds to space-charge limited current for a short bunch to another, higher, plateau that corresponds to the space-charge limited steady-state current. Here the steady-state, space-charge limited current is considerably higher than predicted by eq. (9). It has previously been observed [17] that the steady-state space-charge limited current from microscopic emitters can deviate considerably from what is predicted by the simple 2D Child-Langmuir law, due to the relatively high contribution to the current from the edge of the emitting area, the so-called wing-structure of the emission profile [27, 28], transverse beam expansion, and discrete particle effects. Hence, the underestimation of eq. (9) for the steady-state, space-charge limited current is not unexpected. What may seem unexpected, in light of previous work on short-pulse emission, is that the space-charge limited current for a short pulse is less than the space charge-limited current for the steady-state. This is not a discrepancy. In part the explanation lies with the fact that in the previous work on the short-pulse space-charge limit we are looking at the maximum injection current allowed so as not to form a virtual cathode over the duration of a given pulse length, whereas in our model we are looking at the induced current (which is due to the transit of the critical bunch of charge, once formed, across the diode gap). Thus the inverse scaling of the critical current with pulse length is not appropriate for our purpose. However, the reason that the space-charge limited current in the steady-state is higher than that of a short bunch has a physical reason associated with the mechanics of space-charge limited current from a microscopic emitter, as will be described when the total charge of the pulse is examined in the following paragraphs.

Since it is apparent that, for short pulses, it is the single sheet model that is most appropriate, we now turn our attention to the amount of charge in the electron bunch as a function of laser pulse width for different values of scaled laser amplitude, emitter area and gap voltage. Fig. 6 shows how the laser amplitude affects total charge as a function of the normalized pulse length. Greater amplitude corresponds to a higher rate of photo-electrons being
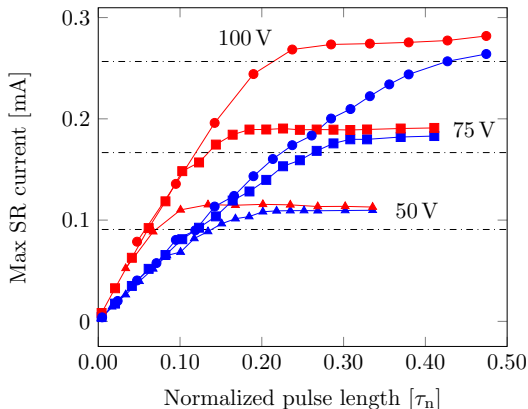
FIG. 4. Induced current vs. normalized pulse length for three different gap voltages: 50, 75, 100 V, 250 nm emitter radius with curves for scaled laser amplitudes of 5 (blue) and 10 (red). The current from eq. (9) is represented by the horizontal dash-dotted lines for 50, 75, 100 V.
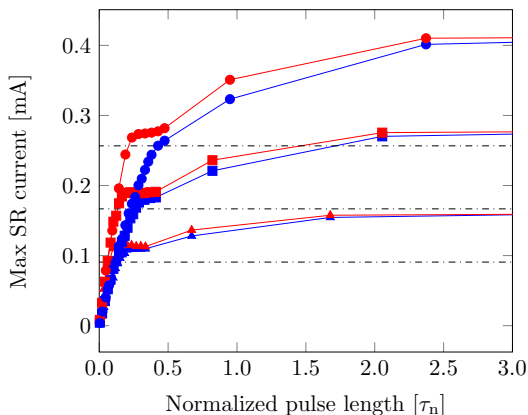

FIG. 5. 50, 75, 100 V, 250 nm emitter for scaled laser amplitude of 5 (blue) and 10 (red).: the CL limit from eq. (9) is drawn in black for the different gap voltages.

produced at the cathode. The space-charge limit shows up as a plateau in the total charge in the pulse. For low laser amplitudes the space-charge limit can not be reached, whereas it is obtained at shorter pulse lengths for larger amplitudes.

From Fig. 7 we can see how the gap voltage affects the total charge. From the simple, single sheet model where the charge density of the sheet is given by $\sigma = \varepsilon_0 V/D$, and the emitter radius is 250 nm we would expect a total charge of 0.35 fC (femto Coulomb), 0.52 fC, and 0.70 fC for gap voltages of 50 V, 75 V, and 100 V, respectively. The measured charge is 2 to 3 times higher. The reason

for this difference is that the estimation for the charge density of the sheet does not take into account the effects of limited emitter area that are implicit in the 2D Child-Langmuir law. Note for instance that the space-charge limited current density from eq. (9) with values of $R = 250$ nm and $D = 2500$ nm is 3.5 times higher than the space-charge limited current density for an emitter of infinite extent. From the single sheet model we would anticipate a linear relationship between the critical charge and the gap voltage, but, in fact the charge increases at a lower rate with voltage, e.g. the total charge for the pulse at 100 V is only 60 percent greater than the total charge at 50 Volt. We do not have an explanation for this.

Next we look at how the total charge is affected by the radius of the emitting area. We see a linear rise in the pulse charge with pulse length until a plateau due to space-charge limitation is reached. For the single sheet, capacitive, model we anticipate that the charge at the plateau scales with the area of the emitter (the emitter radius to the second power). This is not the case as the current from the 250 nm radius emitter is roughly three times as high as that from the 125 nm radius emitter, rather than four times as high as might be expected for a single sheet of uniform charge density. This can probably be explained by the fact that edge emission has a larger contribution to the total charge for the emitter of smaller radius. We also note that for larger values of the normalized pulse, the total charge increases again as the transition from the single-sheet regime to the steady-state filled cathode regime begins. Recall that the steady-state space-charge limited current is greater than that anticipated by eq. (9) due to a large fraction of the emission coming from the edge of the emitter and due to transverse expansion of the beam [17]. This effect becomes more prominent as the ratio Z_c/R increases, where Z_c denotes the elevation of the center of charge above the cathode and R is the emitter radius. As a result of this, the steady-state current transition to the space-charge regime for larger area emitters begins when the beam bunch has propagated further along the diode than for smaller emitters. Hence, the transition between regimes occurs earlier for smaller emitters. Finally, we turn our attention to the brightness of the electron beam. We look at the data underlying Fig. 6 and plot the brightness of the beam as a function of the normalized pulse length for different values of the laser amplitude. This can be seen in Fig. 9 and Fig. 10 where a peak value of the brightness is apparent. The peak value is roughly constant, though the peak becomes sharper as the scaled laser amplitude increases. We note that the peak brightness is achieved when the charge in the electron bunch corresponds to roughly 40 percent of the critical charge for the short-pulse space-charge limit, which holds true for all voltages and emitter radii that were simulated.
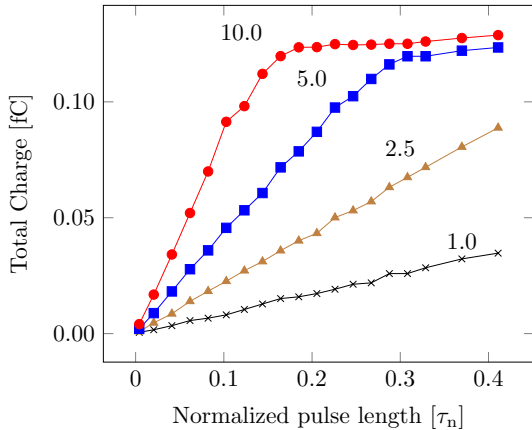
FIG. 6. Total charge vs. normalized pulse length for scaled laser amplitude of 1, 2.5, 5, 10. Gap voltage of 75 V, 250 nm radius emitter. The lowest amplitude (black) will not reach the space-charge limit before saturating the gap with constant current.

FIG. 8. 75 V, 125, 187.5, 250 nm radius emitters, 5, 10 Amplitude. Emitter size increases the space-charge limit with respect to pulse length while again the slope is related to amplitude.
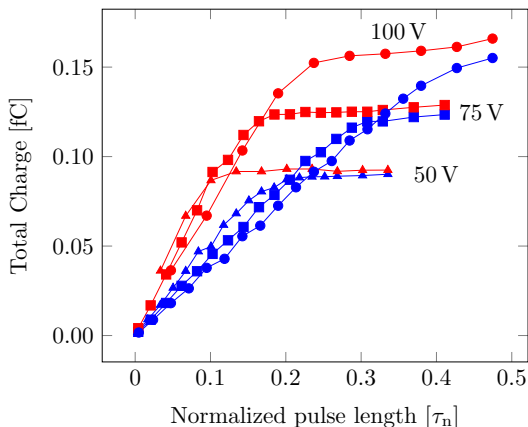
FIG. 7. Total charge vs. normalized pulse length for three different voltages. 50, 75, 100 V, 250 nm emitter, scaled laser amplitude of 5 (blue) and 10 (red). Increased voltage affects the space-charge limit with respect to pulse length while slope is related to amplitude.

FIG. 9. Brightness versus normalized pulse length for different scaled laser amplitudes. 75 V gap potential, 250 nm emitter radius: The brightness peak shifts to the left, shorter pulse width, as the amplitude increases. Black, brown, blue, red, correspond to 1, 2.5, 5, 10 in amplitude respectively.

IV. SUMMARY AND CONCLUSIONS

Using MD-Simulations we examined the transition from source limited emission to space-charge limited emission in photo-emitted electron beams in a microscopic diode for different values of laser pulse width, intensity, emitter area (or spot size) and accelerating potential. We found that conventional capacitive models of short-pulse electron bunches may considerably underesti-

mate their total charge due to neglecting two-dimensional space-charge effects, whereas the estimates for the short-pulse space-charge limited current using the approach of Koh and Ang, shown in eq. (7), give a reasonably accurate estimate for the maximum current induced by a electron bunch transiting the diode gap. We also identified parameters for optimal brightness of the beam bunch. For the parameter range that we studied it is found that the highest value of brightness occurs when the charge in
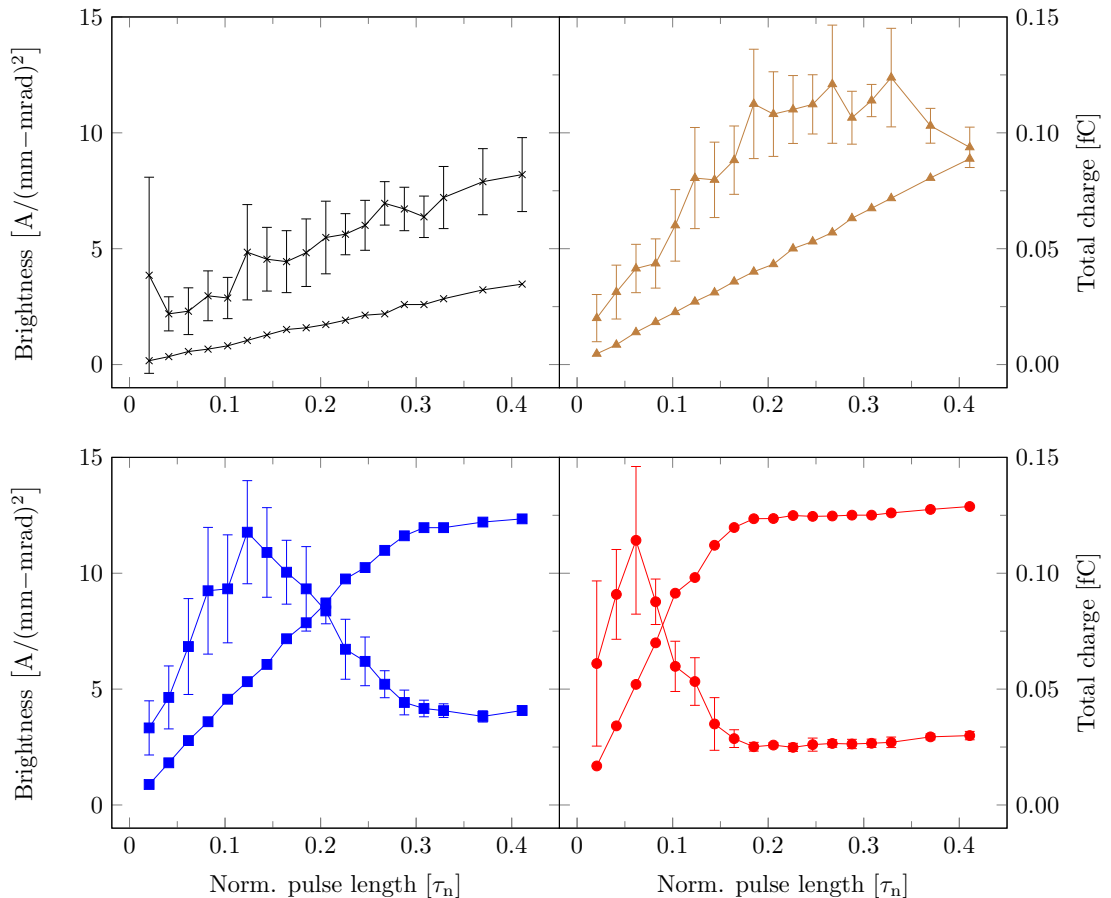
FIG. 10. Brightness and total pulse charge versus pulse length. 75 V gap potential, 250 nm emitter radius: Charge and brightness lines of rising amplitudes have the same colors, brightness has error bars. Black, brown, blue, red, correspond to 1, 2.5, 5, 10 in amplitude respectively. The Brightness peak hits at approx. 40% of total charge peak.

the beamlet is roughly 40 percent of the critical charge for formation of a virtual cathode. This result is similar to what has been found for thermal emission in microdiodes, in that optimal brightness is achieved at a point during transition from source-limited to space-charge limited emission. This may have some practical value for designers of electron sources for coherent and time resolved electron beams.

ACKNOWLEDGMENT

[1] J. H. Booske, "Plasma physics and related challenges of millimeter-wave-to-terahertz and high power microwave generation," *Physics of Plasmas*, vol. 15, no. 5, p. 055502, 2008.

[2] A. H. Zewail and J. M. Thomas, *4D electron microscopy: imaging in space and time.* London : Hackensack, NJ: Imperial College Press ; Distributed by World Scientific Pub, 2010, oCLC: ocn299716296.

[3] S. Sun, X. Sun, D. Bartles, E. Wozniak, J. Williams, P. Zhang, and C.-Y. Ruan, "Direct imaging of plasma waves using ultrafast electron microscopy," *Structural Dynamics*, vol. 7, no. 6, p. 064301, Nov. 2020, publisher: American Institute of Physics. [Online]. Available: https://aca.scitation.org/doi/full/10.1063/4.0000044

[4] W. A. Barletta, J. Bisognano, J. N. Corlett, P. Emma, Z. Huang, K. J. Kim, R. Lindberg, J. B. Murphy, G. R. Neil, D. C. Nguyen, C. Pellegrini, R. A. Rimmer, F. Sannibale, G. Stupakov, R. P. Walker, and A. A. Zholents, "Free electron lasers: Present status and future challenges," *Nuclear Instruments and Methods in Physics Research Section A: Accelerators, Spectrometers, Detectors and Associated Equipment*, vol. 618, no. 1, pp. 69–96, Jun. 2010. [Online]. Available: https://www.sciencedirect.com/science/article/pii/S0168900210005656

[5] M. Reiser, P. O'Shea, S. Bernal, and R. Kishek, *Theory and Design of Charged Particle Beams: Second Edition*, 2nd ed. New York, NY: Wiley, 2008, publication Title: Theory and Design of Charged Particle Beams: Second Edition.

[6] D. A. Edwards and M. J. Syphers, *An introduction to the physics of high energy accelerators*. John Wiley & Sons, Inc, 1993.

[7] K. L. Jensen, *Introduction to the physics of electron emission*. Hoboken, New Jersey: John Wiley & Sons, Inc, 2018.

[8] P. Zhang, Y. S. Ang, A. L. Garner, A. Valfells, J. W. Luginsland, and L. K. Ang, "Space–charge limited current in nanodiodes: Ballistic, collisional, and dynamical effects," *Journal of Applied Physics*, vol. 129, no. 10, p. 100902, Mar. 2021, publisher: American Institute of Physics. [Online]. Available: https://aip.scitation.org/doi/full/10.1063/5.0042355

[9] I. V. Bazarov, B. M. Dunham, and C. K. Sinclair, "Maximum Achievable Beam Brightness from Photoinjectors," *Physical Review Letters*, vol. 102, no. 10, p. 104801, Mar. 2009. [Online]. Available: https://link.aps.org/doi/10.1103/PhysRevLett.102.104801

[10] M. Kuwahara, Y. Nambo, K. Aoki, K. Sameshima, X. Jin, T. Ujihara, H. Asano, K. Saitoh, Y. Takeda, and N. Tanaka, "The Boersch effect in a picosecond pulsed electron beam emitted from a semiconductor photocathode," *Applied Physics Letters*, vol. 109, no. 1, p. 013108, Jul. 2016, publisher: American Institute of Physics. [Online]. Available: https://aip.scitation.org/doi/full/10.1063/1.4955457

[11] A. Sitek, K. Torfason, A. Manolescu, and A. Valfells, "Space-Charge Effects in the Field-Assisted Thermionic Emission from Nonuniform Cathodes," *Physical Review Applied*, vol. 15, no. 1, p. 014040, Jan. 2021, publisher: American Physical Society. [Online]. Available: https://link.aps.org/doi/10.1103/PhysRevApplied.15.014040

[12] K. Torfason, A. Valfells, and A. Manolescu, "Molecular dynamics simulations of field emission from a prolate spheroidal tip," *Physics of Plasmas*, vol. 23, no. 12, p. 123119, 2016, arXiv: 1608.06789 ISBN: 1070-664X, 1089-7674. [Online]. Available: http://aip.scitation.org/doi/10.1063/1.4972821

[13] K. L. Jensen and E. J. Montgomery, "Photoemission Theory and the Development of High Performance Photocathodes," *Journal of Computational and Theoretical Nanoscience*, vol. 6, no. 8, pp. 1754–1769, Aug. 2009.

[14] K. Torfason, A. Valfells, and A. Manolescu, "Molecular dynamics simulations of field emission from a planar nanodiode," *Physics of Plasmas*, vol. 22, no. 3, p. 033109, 2015, iSBN: 1070-664X, 1089-7674. [Online]. Available: http://aip.scitation.org/doi/10.1063/1.4914855

[15] K. Torfason, A. Manolescu, and A. Valfells, "High-fidelity molecular dynamics of vacuum nanoelectronics," in *2018 31st International Vacuum Nanoelectronics Conference, IVNC 2018*. IEEE, 2018, pp. 1–2. [Online]. Available: https://ieeexplore.ieee.org/document/8520287/

[16] H. V. Haraldsson, K. Torfason, A. Manolescu, and A. Valfells, "Molecular Dynamics Simulations of Mutual Space-Charge Effect Between Planar Field Emitters," *IEEE Transactions on Plasma Science*, vol. 48, no. 6, pp. 1967–1973, Jun. 2020. [Online]. Available: https://ieeexplore.ieee.org/document/9093900/

[17] J. B. Gunnarsson, K. Torfason, A. Manolescu, and A. Valfells, "Space-Charge Limited Current From a Finite Emitter in Nano- and Microdiodes," *IEEE Transactions on Electron Devices*, vol. 68, no. 1, pp. 342–346, Jan. 2021, conference Name: IEEE Transactions on Electron Devices. [Online]. Available: https://ieeexplore.ieee.org/document/9266079/

[18] K. Torfason, A. Sitek, A. Manolescu, and A. Valfells, "Dynamics of a field emitted beam from a microscopic inhomogeneous cathode," *IEEE Transactions on Electron Devices*, vol. 68, no. 5, pp. 2461–2466, 2021.

[19] S. Ramo, "Currents Induced by Electron Motion," *Proceedings of the IRE*, vol. 27, no. 9, pp. 584–585, 1939.

[20] W. Shockley, "Currents to conductors induced by a moving point charge," *Journal of Applied Physics*, vol. 9, no. 10, pp. 635–636, Oct. 1938, publisher: American Institute of PhysicsAIP. [Online]. Available: http://aip.scitation.org/doi/10.1063/1.1710367

[21] K. L. Jensen, "General formulation of thermal, field, and photoinduced electron emission," *Journal of Applied Physics*, vol. 102, no. 2, p. 024911, Jul. 2007, publisher: American Institute of Physics. [Online]. Available: https://aip.scitation.org/doi/abs/10.1063/1.2752122

[22] P. Zhang, A. Valfells, L. K. Ang, J. W. Luginsland, and Y. Y. Lau, "100 Years of the Physics of Diodes," *Applied Physics Reviews*, vol. 4, no. 1, p. 11304, 2017, iSBN: 1931-9401. [Online]. Available: http://aip.scitation.org/doi/10.1063/1.4978231

[23] Y. Y. Lau, "Simple Theory for the Two-Dimensional Child-Langmuir Law," *Physical Review Letters*, vol. 87, no. 27, p. 278301, 2001, iSBN: 0031-9007, 1079-7114. [Online]. Available: https://link.aps.org/doi/10.1103/PhysRevLett.87.278301

[24] W. S. Koh, L. K. Ang, and T. J. T. Kwan, "Three-dimensional Child–Langmuir law for uniform hot electron emission," *Physics of Plasmas*, vol. 12, no. 5, p. 053107, 2005. [Online]. Available: https://doi.org/10.1063/1.1913612

[25] A. Valfells, D. W. Feldman, M. Virgo, P. G. O'Shea, and Y. Y. Lau, "Effects of pulse-length and emitter area on virtual cathode formation in electron guns," *Physics of Plasmas*, vol. 9, no. 5, pp. 2377–2382, 2002.

[26] R. J. Umstattd, C. G. Carr, C. L. Frenzen, J. W. Luginsland, and Y. Y. Lau, "A simple physical derivation of Child–Langmuir space-charge-limited emission using vacuum capacitance," *American Journal of Physics*, vol. 73, no. 2, pp. 160–163, Feb. 2005, publisher: Ameri-

can Association of Physics Teachers. [Online]. Available: https://aapt.scitation.org/doi/10.1119/1.1781664

[27] R. J. Umstattd and J. W. Luginsland, "Two-Dimensional Space-Charge-Limited Emission: Beam-Edge Characteristics and Applications," *Physical Review Letters*, vol. 87, no. 14, p. 145002, Sep. 2001, publisher: American Physical Society. [Online]. Available: https:

//link.aps.org/doi/10.1103/PhysRevLett.87.145002

[28] J. W. Luginsland, Y. Y. Lau, R. J. Umstattd, and J. J. Watrous, "Beyond the Child–Langmuir law: A review of recent results on multidimensional space-charge-limited flow," *Physics of Plasmas*, vol. 9, no. 5, pp. 2371–2376, May 2002. [Online]. Available: http://aip.scitation.org/doi/10.1063/1.1459453

Paper II

nano select Open Access WILEY

Enhanced photoemission from surface modulated GaAs:Ge

Muhammad Taha Sultan | **Hákon Örn Árnason** | **Movaffaq Kateb** |
Andrei Manolescu | **Halldór Gudfinnur Svavarsson** | **Ágúst Valfells**

Department of Engineering, Reykjavik
University, Menntavegur 1, 102,
Reykjavík, Iceland

Correspondence
Muhammad Taha Sultan, Department
of Engineering, Reykjavik University,
Menntavegur 1, 102, Reykjavík, Iceland.
Email: muhammads@ru.is

Muhammad Taha Sultan and Hákon Örn
Árnason contributed equally to this work.

Funding information
Icelandic Research Fund (IRF) of the
Icelandic center of Research, Grant/Award
Numbers: 174512-051, 218029–051

Abstract
The present work reports the evolution and growth of GeGaAs(O) polytype
nanoislands over GaAs p-type substrate with photoemission application in mind.
Several morphological transformations from NIs to simultaneously present
nanopits/holes are observed as a function of annealing parameters that is, tem-
perature (350-800°C) and time (5-90 minutes). Structural and elemental analyses
are executed using atomic force microscopy, scanning electron microscopy and
energy dispersive X-ray spectroscopy. Photoemission current of the nanostruc-
tured surfaces, measured upon exposure from 265 nm light emitting diode, is
found to depend on the nanoislands size, which in turn depends on the anneal-
ing parameters. A maximum photoelectric emission is obtained for structure
annealed at 650°C for 60 minutes, upon which an increment of roughly two
orders of magnitude is observed.

KEYWORDS
AFM, GaAsGe, nanostructure, photoemission, SEM

1 | INTRODUCTION

Photoemission (PE) refers to the emission of electrons
from a surface due to excitation by one or more photons
(light). It is commonly used for generating electron beams
for applications such as electron microscopes, free elec-
tron lasers, and other particle accelerators.[1–3] It can also
be used for devices of more modest performance require-
ments such as simple diodes, but then the cost of the photo-
cathodes must be reduced. The energy of the light must be
equal to or higher than the work function Φ of the emitting
material so for many applications, high-energy ultra-violet
(UV) light is required. An exception to this is multiphoton
emission which may occur for exceptionally intense laser
light.[4] For applications where the photoemission is to
be achieved with a lower energy light source (closer to or

overlapping the visible spectral range and thus less expen-
sive), the emitter often contains cesium (Cs), th–e element
with the lowest work function (1.95 eV, corresponding to
636 nm light) of all elements. However, in practice it is not
easy to process Cs, which is very unstable and reactive.
Therefore, a stable material that could substitute Cs for
photoemission is of great practical interest. In general, the
work function, Φ, of semiconductors strongly depends on
their band-gap, the larger the band-gap, the larger is Φ
(i.e., Φ = electron affinity + band-gap energy). For photo-
emission applications, III-V semiconductors like GaAs and
InAs are possible candidates due to their high quantum
yield and direct band-gap, although their work function
is much higher than that of Cs, in the range of 4.7-4.9 eV
(corresponding to wavelength of 264-253 nm). Indirect
band-gap materials like bulk Ge or Si might also become

contenders by nano-modulation of their surfaces. Bringing Ge down to nanoscale, for instance in the shape of nanowires or nanoislands (NIs)[5,6] has resulted in roughly eightfold increase of emitting efficiency compared to its bulk counterparts. This feature can be attributed to higher hole mobility in Ge out of group IV semiconductors[7–9] with the possibility of converting its indirect band-gap into a direct one by incorporating strain within the structure, since there is a very small difference between the indirect and direct band-gap of Ge (i.e. ~136 meV).[10,11]

With the aim of reducing the work function of semiconductor-based emitters, several studies have dealt with incorporating Cs and O,[12–14] or Sb-Cs-O[15] in GaAs. The incorporation of Cs and O, in Si and Ge photoemitters has also been achieved with appreciable emission response.[16] However, the presence of Cs requires delicate fabrication steps and for good adhesion of Cs-O, the GaAs surface needs to undergo in-situ cleaning on atomic level, via either chemical etching, thermal vacuum annealing, or atomic hydrogen cleaning. Even after such intricate pre-processing, the Cs-O layer can be quite flimsy and easily destroyed by chemical agents. Therefore, attempts have been made to obtain efficient PE characteristics using Ge either as a seed layer or as a dopant in GaAs[17,18] rather than using the unstable Cs.

GaAs has been considered a suitable candidate for light emitting diodes (LED), solar cells and photodetectors[7,19,20] due to its favorable electronic properties such as high electron mobility.[20] Its suitability can be further enhanced by alloying with a group IV element of which germanium (Ge) is arguably the best choice. It possesses the highest hole mobility out of group IV semiconductors[7–9] and has a lattice constant and thermal expansion coefficient close to that of GaAs (differences of 0.07% and 0.03%, respectively[21]) and yet the band-gap is different (~1.44 eV for GaAs vs. ~0.67 eV for Ge[19]). In contrast, use of other group IV elements involve some fundamental problems associated with large lattice mismatch (~4% for silicon) and different thermal expansion coefficients. In-diffusion of Ge in GaAs[7,22,23] can results in $GaAs_{1-x}Ge_x$ structures[20,23] exhibiting direct band-gap with superior optical properties.[19]

For semiconductors, bringing the structure down to nanoscale may fundamentally modify the properties of materials by inducing low-dimensional charge carrier confinement[24] and self-assembling, allowing the growth of well-defined random or aligned nano/quantum structures[24] without the need of sophisticated lithography techniques.[24] Nanostructuring processes may be brought about by thermal treatment at temperature below the melting point of the material used.[25] Among challenges faced with integration of Ge and GaAs are[21,26]

formation of anti-phase boundaries (APD) and inter-diffusion of Ge,[27] O,[22] Ga and As at the interfaces or the surface.[28] Ge diffused in GaAs will tend to act as a donor in GaAs.[22,28] where the Ge in-diffusion depth of up to hundreds of nanometers has been reported[7,26,29] and is dependent on annealing time and temperature. Surface modulation on nanoscale may be brought up on a Ge surface by annealing a thin Ge-layer on GaAs substrate. The mechanism behind the formation has been explained on the basis of phase separation and surface segregation of Ga due to low solubility of Ga in Ge,[30] and Ge diffusion into GaAs via Ga vacancies.[27,31,32] Notably, use of high temperature processing of such structure is restricted since Ge forms a eutectic alloy with GaAs at 865°C.[7,29]

Our present paper describes the fabrication and characterization of a GaAs:Ge based photocathode (emitter) with effective PE characteristics under illumination by a simple and low-cost commercially available UV (~265 nm) LED, having low optical power, but sufficient energy to excite the photoelectron from GaAs into vacuum level. In this regard, thermally treated GaAs:Ge structures were taken into consideration and compared with as-grown GaAs:Ge and GaAs. Although studies mentioned above have been carried out over Ge doped GaAs structures and consequent evolution of various nanogeometries, however, most of them have dealt with structural and morphological evolutions and/or diffusion characteristics of Ge. In this study we undertake the application of Ge doped GaAs structures as a photoemitter with Ge deposition directly on GaAs substrate without the need of depositing either Ga and/or As, which would require delicate fabrication methods and parameter controls. This simple easy to fabricate structure overcome the need of utilizing complex fabrication and packaging steps, which as mentioned above would be imperative for Cs doped GaAs based photoemitters.

2 | RESULTS AND DISCUSSION

2.1 | Structural characterization

To study the effect of annealing parameters on surface reconstruction, the samples comprising of Ge being deposited over p-type GaAs substrate (GaAs: Ge), were annealed at temperature T between 350 and 800°C for time t = 5-90 minutes. Table 1 summarizes the list of samples with corresponding annealing parameter.

2.2 | Effect of annealing temperature

Figure 1 and S1 shows atomic force microscope (AFM) micrographs and SEM images of a structure annealed at
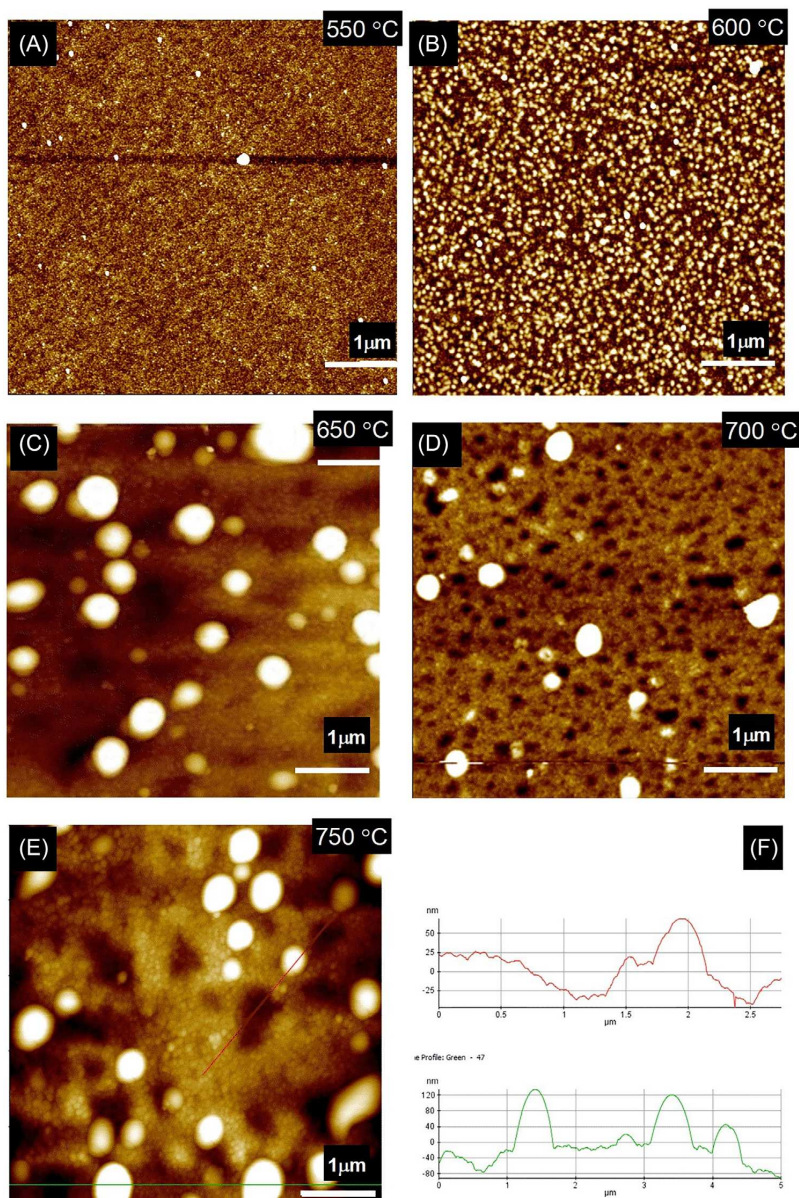
FIGURE 1 AFM micrographs of structures (A-E) annealed at 550, 600, 650, 700, and 750°C for 60 minutes. F, Line scan for AFM micrograph in (E) over nanopits (upper) and NIs (lower), respectively

temperatures of 550 to 750°C for 60 minutes. For temperatures up to 550°C, there was no observed formation of NIs. However, the roughness (R_q) increases from 0.417 to 0.969 nm for as-grown samples to those annealed up to 550°C, respectively. With further increase in T to 600°C, a noticeable presence of closely spaced NIs can be seen (Figure 1B), which when annealed for 650°C

(Figure 1C and 2B), resulted in formation of mildly spaced NIs with increased size. The EDX analysis carried out on structures showed that NIs comprise of Ga, As, Ge and O (Figure 2 and Table S1). The surface next to the islands is comprised of oxidized GaAs and does not contain Ge. Such a presence/incorporation of oxygen in the structure is explained in a detailed study of Wang et al.[22] who

TABLE 1 List of samples prepared

T [°C]	Annealing t [min]				
	5	10	30	60	90
350				X	
400			X	X	
450			X	X	
550	x	X	X	X	
600		X	X	X	X
650	x	X	X	X	X
700		X	X	X	X
750	x	x	X	X	X
800	x	x	X		

The highlighted columns are those samples considered in text for comparison.

FIGURE 2 Elemental analysis carried out via EDS analysis over NIs for structures annealed at T ranging from 600 to 750°C

studied oxygen diffusion of Zn-doped GaAs (001) in the presence of Ge and As_2O_3-rich ambient. The oxygen content can reach appreciable values due to co-incorporation of Ge-O pairs, similar to what has been observed for other trivalent-metal oxide, Al-O, which resulted in high level of oxygen incorporation.[33] This is due to the fact that germanium oxide possesses lower vapor pressure than arsenic oxide.[22] Further, the bond dissociation energy of Ge-O at room temperature is 662 kJmole^{-1} (which is larger

than that of Al-O and slightly lower than of Si-O), thus implying that Ge and O can be strongly coupled together and incorporated in GaAs. Further, it is noteworthy to mention here that the sample annealed at 650 °C, resulted in NIs with narrow size distribution, and that the EDS analysis carried on NIs as highlighted in Figure 2, S1b and Table S1, shows that there is only a marginal difference in composition that is, relative at% ratio between NIs located at different sites and having varying sizes.

For samples annealed at still higher T (700 and 750°C) for 60 minutes (Figure 1D,F) and S1(c)), it is apparent that the size of the NIs increased with increased T, along with the formation of pits randomly distributed over the surface (the size of which also increased with T). This was associated with decreased island population density and increased nanopit density. A similar behavior that is, increased island size and decreased island density was observed by Jin et al.,[26] for structures/samples having Ge on GaAs (100). An exemplary line-scan Figure 1E over the AFM micrograph in Figure 1E shows the width and height of NIs along with the spacing between them. Figure 3A shows the size of NIs and nanopits as a function of annealing T. The AFM micrograph were repeated for each sample on different reference areas in order to validate the reproducibility of these features and obtained micrographs were analyzed via XEI 1.8.0 software by Park Systems Corporation. The size of nanostructure was measured using line scans and the results were additionally scrutinized by Gwyddiom 2.39 software. Additionally, the aspect ratio (shown for review purpose only) and the area covered by NIs and pits over the surface (determi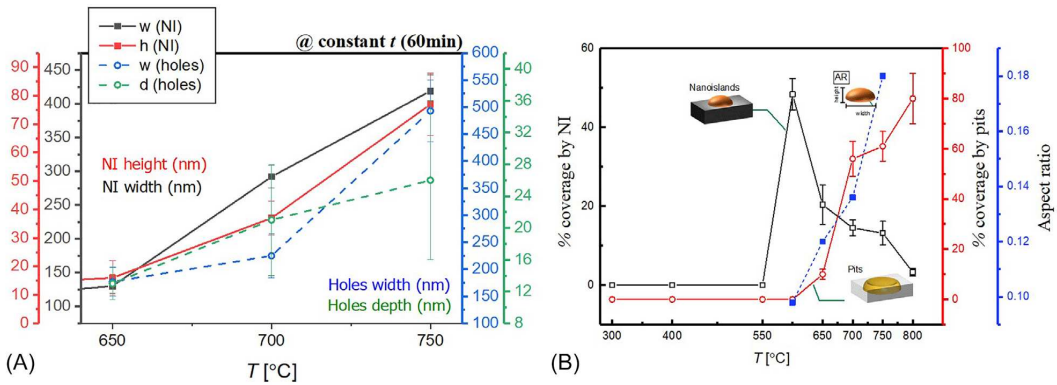ned by using Image-J software) are plotted in Figure 3B as a function of annealing T. The plot with variation in total area covered by NIs, as a function of annealing T complements the findings that the population density of NIs decreases with increased annealing T and t. Furthermore, the root mean square roughness R_q increases as a function of annealing t and T (see supplementary information Figure S2(a,b)). The rise in surface roughness with increased annealing parameters can be attributed to surface oxide formation and evaporation of As (most likely as As_2). A similar observation that is, increase in roughness has also been reported in a study by Rasheed,[9] on Ge(:In)/GaAs structures. EDX analysis carried out on structures (presented in Table S1) depicts that the NIs (and bottom of the pits) are deprived of As while the flat surface is deprived of Ga.

A molecular dynamic (MD) simulation was conducted, using LAMMPS1 program (see experimental section for description), to understand the atomistic mechanism of the process (Figure S3). A GaAs nanoparticle of 5 nm in diameter with the zinc-blend structure was considered in the calculations. The nanoparticle is chosen because its relatively large surface area increases the probability of

FIGURE 3 A, The size of NIs and nanopits as a function of annealing T at constant $t = 60$ minutes. B, Area covered by NIs (black line) and pits (red line), as a function of annealing T (data points shown with error bars). Aspect ratio obtained from AFM analysis for structures annealed at varying anneal T at constant t of 60 m is plotted represented by blue dashed line

surface phenomenon and allows observation of the process in an inexpensive simulation while simulation of a large slab is computation costly and might include extra considerations such as strain effects due to the thermal expansion. Nanoparticle model is widely used to study phase transitions at atomistic resolution.[34,35] We would like to remark that the nanoparticle model still enables to understand whether it is As$_2$ sublimation or pure Ga segregation that motivates Ga nucleation. A detailed description concerning the MD simulation, along with relevant figure (Figure S3) and a movie (Movie S1) is included in the supplementary information. There it is seen that with increasing annealing T, As start to evaporate as dimers, leaving behind excess Ga atoms.[36]

2.3 | Morphological evolution of nanostructures

In general, a formation of self-assembled 3D islands is a consequence of induced strain between lattice mismatched structures like Ge (or Ge$_x$Si$_{1-x}$) on Si[37–39] or (Ga)InAs on GaAs.[40,41] However, in case of small lattice mismatch as in the Ge and GaAs system (~0.07%), the mechanism is different and is typically governed by 2D mechanism.[42] In such case, the tendency of island formation occurs randomly, where the driving force for the formation of NIs is the reduction in total surface energy by minimizing substrate induced strain and electronic effects.[8,26]

The underlying substrate induces strain in the film, which in case of Ge on GaAs is compressive.[19,43] This strain tends to be compensated by Ge segregation[19] and enlargement of Ge lattice in the growth direction.[43] Strong interaction of Ge atom with GaAs, along with Ge segregation and annealing induced atomic diffusion, gives

rise to observed polytype of GaAsGe NIs (Figure 1, S1, and Figure 4) with additional presence of oxygen as mentioned earlier. Such alloying of GaAs and Ge may result in lattice constant larger than that calculated by Vegard's Law.[19,38] A detailed study of Ge interaction and its diffusion in GaAs atomic planes can be found in a paper by Sozen et al..[20]

Furthermore, there is evidence in the literature that Ga vacancies are the most probable source of increased diffusion of Ge[27,42] when grown over GaAs,[22] and that the phenomena is governed by annealing parameters.[19] The Ge film-growth on GaAs proceeds via formation of Ge-Ga bonds which have lower formation energy than Ga-As bonds.[8,21,26] Thus, the nanostructures that is, NIs and nanopits in our study tends to form due to lower mobility of As on the GaAs substrate, as has also been reported by Cheng et al..[21] As mentioned earlier, the nucleation of NIs preferably occurs where the surface energy is at minimum. Thus, considering the study by Liu et al.,[19] if the surface energy is taken into consideration, the strain energy (which is compressive for Ge film on GaAs substrate[19]) is more easily relaxed by the formation of islands because of reduced chemical bond energies and number of neighboring adatoms. In contrast, the pits are caused by the relaxation of tensile strain due to reduction in chemical potential energy. In addition, the As-rich GaAs surface tends to impede the bonding of Ge with Ga,[8,21,26] complementing the EDX results depicting surface being deprived of Ga (i.e. rich in arsenic) and absence of Ge (see Table S1).

2.4 | Effect of annealing time

To elaborate briefly on the effect of annealing time, fixed annealing $T = 750°C$ is considered here (Figure 4), along with a brief discussion for $T = 600$, 650 and 800°C (see
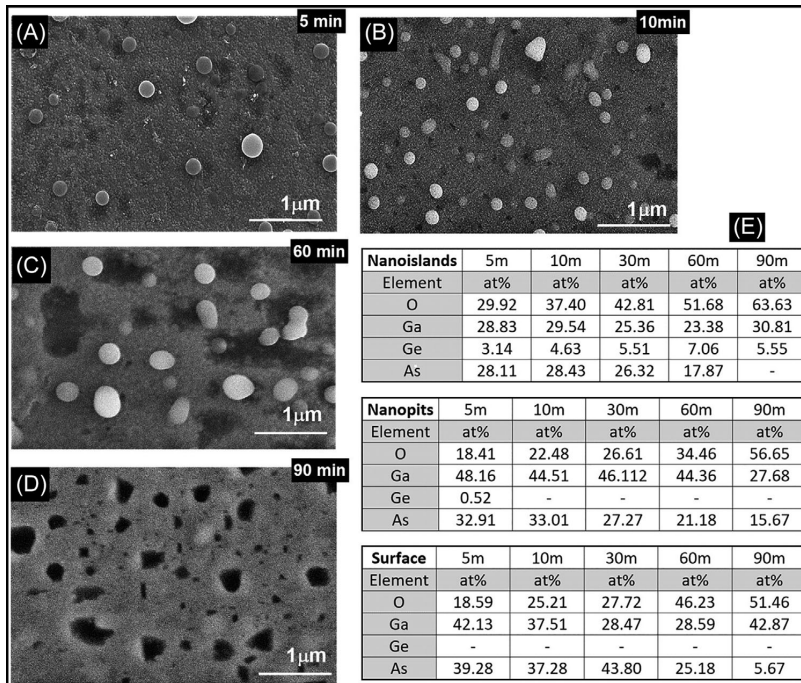
FIGURE 4 Structural analysis via SEM on GaAs:Ge samples annealed at 750°C for (A) 5, (B) 10, (C) 60, and (D) 90 minutes, respectively. E, Element analysis obtained via EDX analysis (at%) for: NIs, nanopits and surface

Figures S4, S5, and S6, respectively in supplementary information). It is evident that with increased time from 5 to 90 minutes, the population density of NIs decreases (Figure 3B) whereas the density of pits increases (similar to what was observed in case of increasing annealing T at fixed t). The islands are originally comprised of Ga, As, Ge and O but the As ratio varies with increased annealing time. Such a variation can be explained based on congruent temperature (T_c) for GaAs,[44] and the morphological evolution of nanostructures. For lower annealing t, that is, 5 minutes the As concentration is lower than the Ga,[44,45] as what was expected for structures above T_c, where the As evaporation is higher than that of Ga. Further, increasing the annealing T tends to increase initially the As concentration. This can be supported by the fact that with increasing annealing t the nanopits are formed that is, etching caused by Ga droplets.[44] In such a case the As flux leaving the nanopits will be accumulated by the neighboring NIs or the surface[24,46,47] (see Figure 4E), thereby increasing the relative ratio of As to that of Ga compared to that in nanopits where the Ga amount increased. As the t increases further the etching that is, nanopits depth increases thereby increasing the Ga quantity in the NIs and decreasing the As proportion due to increased evaporation. However, when annealed for longer time, the Ge and O ratios increases while As completely evaporates.

2.5 | Photoemission characterization

Figure 5A shows room-temperature photoemission (PE) current versus applied bias-voltage from GaAs:Ge samples annealed for constant t (~60 minutes), at T ranging from 400-750°C. The photocurrent curves were acquired by subtracting the dark current from the current measured under illumination. Figure 5B, represents the plot for PE current extracted at 14 V as a function of annealing T (at constant t of 60 minutes (black line, Figure 5A) and 30 minutes (red line, see Figure S7), respectively). The bias voltage of 14 V is selected considering sample annealed at 650°C for 60 minutes as a reference, where a sharp transition in current/intensity value was observed. It was observed that the PE current grew with increased annealing T, up to T of 650°C, after which it decreased. It was observed that the PE curve rises rapidly with increased bias voltage up to roughly 14 V, after which is flattens out, slowly approaching saturation Figure 5A. This slow increase can be attributed to geometric shape (toroidal) of the anode in which some electrons can escape through its center as the
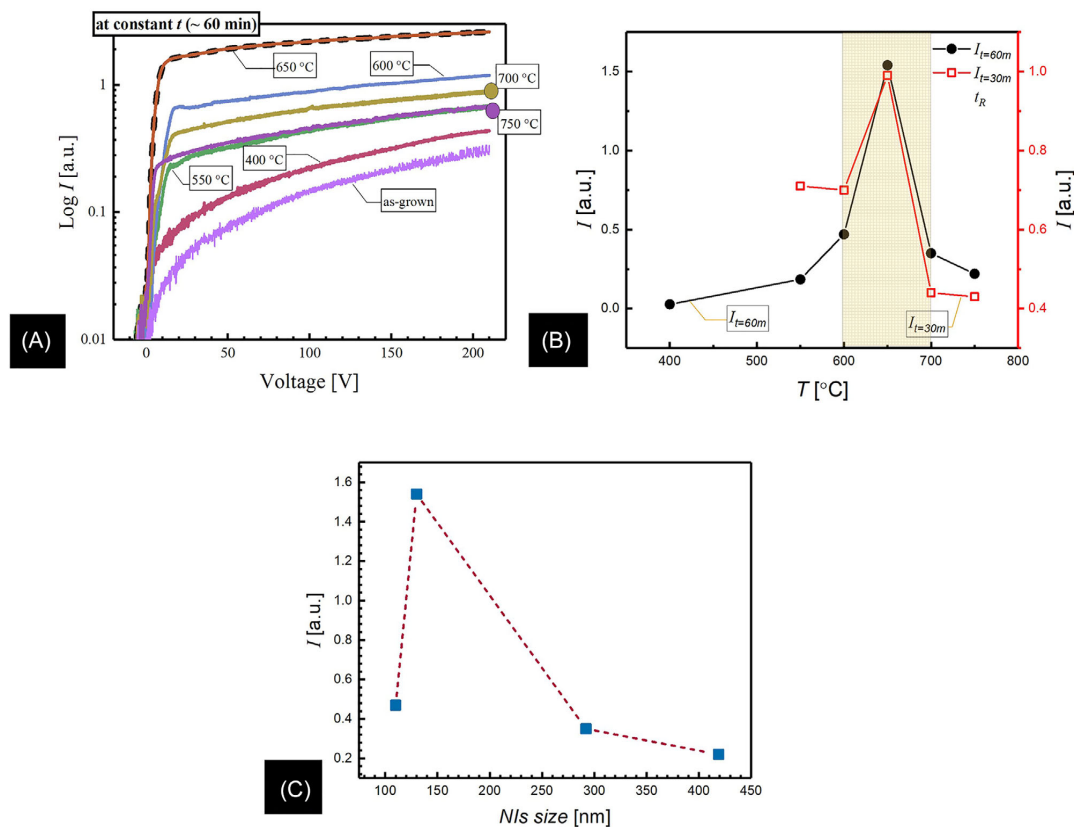
FIGURE 5 A, Photoemission current (I [a.u.]) characteristics of GaAs:Ge structures in as-grown state and that of annealed from 400 to 750°C for fixed t (60 minutes). B, Current [a.u.] values determined at $\sim$ 14 V from I-V plots obtained for structures at various T at constant t of 60 minutes (black line, derived from (A)) and 30 minutes (red line, derived from Figure S6). C, PE current compared with size of NIs, small size and high density of islands results in significantly higher photoemission

electric field between the electrodes is not strong enough to capture them. With increased bias voltage, more electrons will experience enough pull by the electric field to be caught by the adjacent electrode (anode). This strongly indicates that the PE is source limited. A schematic illustration of this in Figure 6 helps visualize how electrons escaping to the vacuum right underneath the anode will be captured while those entering vacuum in the center will not reach the anode due to insufficient electric field strength.

The main source of photoemission appears to be NIs (experiencing quantum confinement due to their relatively small size) which under illumination, excite electrons from the valence band which has lower emission barrier.[6] Thus, electrons are being emitted at a much higher rate. Figure 5C takes the account of PE current as a function of NIs size. Although one would expect an increase in PE current with increased annealing T, however, formation

of largely populated nanopits tends to deteriorate the PE characteristics thereby, reducing the PE current intensity and will be further elaborated later in section. The effect of annealing time at constant temperatures (Figure S8) is included in supplementary information and follows the similar explanation for alteration in PE characteristics.

As mentioned previously a maximum of PE current was observed for sample annealed at 650 °C for 60 minutes, compared to samples annealed at lower and higher temperature edge. Such an alteration in PE current can be explained on the basis that for sample annealed at lower T edge the sample showed no evident formation of nanostructures, except that for sample annealed at 600 °C, where the formation of small NIs can be observed. With further increase in T to 650 °C relatively larger NIs can be seen (Figure 1C and S1(b)), evincing increased PE current. However, a drastic change over in PE current to lower values was observed with increase anneal T. This can be
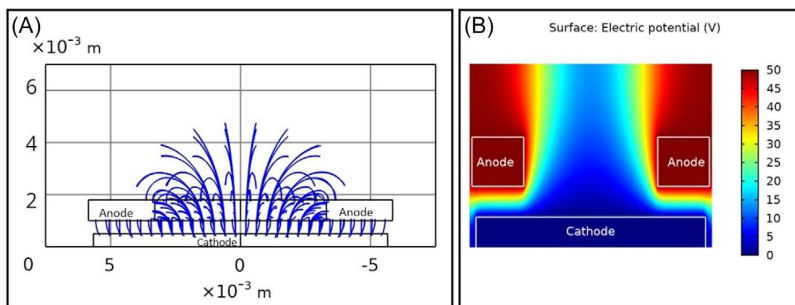
FIGURE 6 A, Computed cross-sectional trajectories of photo-emitted electrons (blue lines) using COMSOL Multiphysics software. Note that the electrons from the center will not reach the anode. B, Cross-sectional view of the electrostatic potential surrounding the electrodes, visualizing the center gap where electrons may escape

explained by the formation and increased NIs sizes along with increased As-content on the surface and formation of densely populated nanopits (i.e. ≥ 700°C), not present at lower annealing T. This can be explained by the previously mentioned fact that annealing above T_c that is ∼ 650°C[44] will initially tend to increase the evaporation rate of As leaving Ga droplets which in turn forms these nanopits due to etching by Ga droplets, in addition to a reduction in As proportions in the NIs. Therefore, an increase in naopits density and variation in NIs stoichiometry with increased annealing parameter will deteriorate the emission characteristics. This is accompanied with a large alteration in composition, that is, reduced Ga and As content, resulting in reduced carrier mobility[48][49] and altered band-gap[50] energy. In addition, reduction of emission current can be further attributed to an increased ratio of oxygen[51][13] with increased annealing temperature,[52] as evident by the EDX analysis (see Table S1).

In order to validate the significance of nanostructured GaAs:Ge, a comparison of the PE characteristics (Figure 7) for annealed GaAs:Ge structures at 650 °C for 60 minutes, were made to that with:

- untreated-GaAs
- as-grown GaAs:Ge
- annealed GaAs

For the untreated GaAs, a weak emission was observed which slightly increased upon deposition of Ge on GaAs (Figure 7, plot 1 and 2). Annealed GaAs had less PE than the annealed GaAs:Ge (Figure 7, plot 3 and 4). The above-mentioned surface analysis is in good agreement with previous studies,[19,21] reporting possible formation of islands and pits for structure with Ge on GaAs, due to lower mobility of As on GaAs substrate and relaxation of local strain potential.
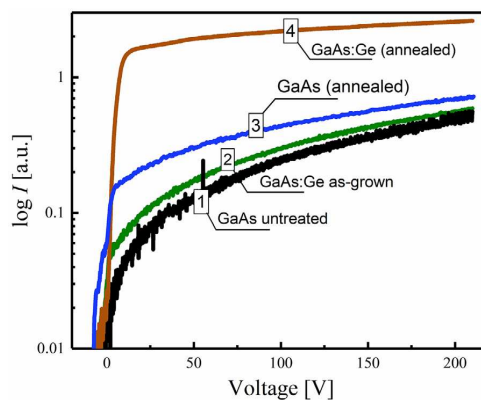

FIGURE 7 Room temperature PE characteristics of: (1) untreated GaAs substrate, (2) as-grown GaAs:Ge structure, (3, 4) GaAs substrate and GaAs:Ge structure annealed at 650°C for 60 minutes, respectively

Validating the structural stability of the proposed method, the samples were tested by running the measurement for four consecutive days. Running the LED for such a long duration would include a higher probability of sample heating. The temperature measured over the sample after running LED for few hours using color changing stripes, was determined to be < 100°C. Figure 8. shows the SEM analysis of sample (annealed for 650 °C, 30 minutes) before and after long run measurements. Negligible variation in surface morphology or compositional analysis (not shown here) was observed for the structures. Further, the PE characteristics have shown insignificant or no change in the current intensity. Thus, illustrating the structural stability of the samples.

Briefly summarized, a morphological analysis of annealed GaAs substrate was conducted. The SEM
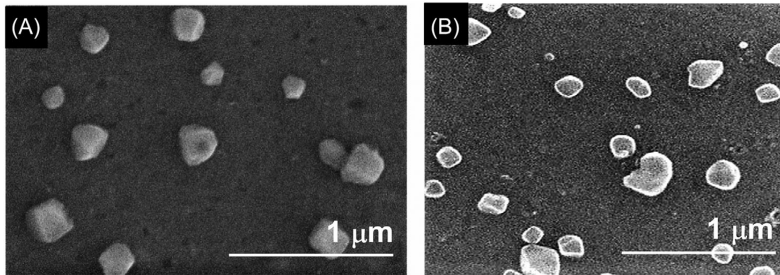
FIGURE 8 SEM images of structure annealed at 650°C, 30 minutes (A) before long run measurement and (B) after long run measurement
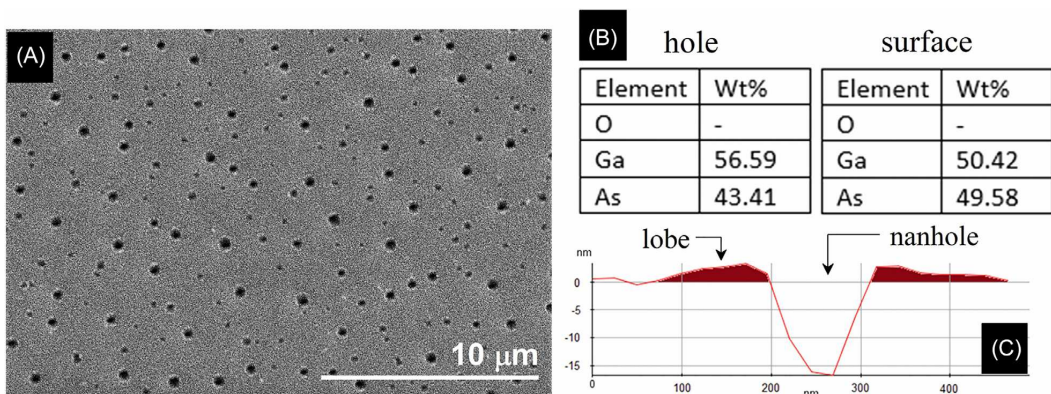

FIGURE 9 A, SEM image of GaAs substrate annealed at 650°C for 60 minutes, and (B) EDX analysis over a typical nanopit and surface, respectively. C, Linescan obtained by AFM analysis for the structure in (A)

analysis revealed formation of nanopits (Figure 9A) with anisotropic lobe around it (Figure 9C) without any evident formation of NIs. However, the As ratio for nanopits determined by EDX (Figure 9B) was similar to that obtained for GaAs:Ge structures. Such formation of nanopits have already been well-documented in studies[24,46,53] and is attributed to electrochemical etching of GaAs by initial formation of Ga droplets.

3 | CONCLUSION

The effect of annealing parameters over the restructuring of Ge on GaAs surface was studied. SEM and AFM analysis revealed various nanopits and NIs morphology. Annealing temperature below 550°C showed no formation of nanostructures. However, annealing temperatures between 600-800°C resulted in emergence of various nano morphologies that is, NIs, enriched in Ge, and nanopits deficient in Ge and As. The size and density of these nanostructures vary as a function of annealing

parameters, which in turn affected the photoemission characteristics.

To conclude the PE characteristic feature and current observed are studied in light of surface morphological changes and are briefly bulleted as follows:

- Annealing parameters affect the surface configuration ratio of nanopits and islands, along with variation in elemental composition which in turn affect the PE characteristics.
- Samples with densely populated (and relatively large) NIs and low density of pits showed enhanced photoelectric emission.
- The elemental composition of nanostructures that is, of Ga, Ge and As plays a vital role in altering the PE characteristics, along with the degree of oxidation that tends to deteriorate the optical and electrical characteristics.
- An optimal photoemission current was achieved for samples annealed at 650°C for 60 minutes.
- A comparison was made between: untreated GaAs substrate; as-grown GaAs:Ge; and annealed GaAs and

GaAs:Ge. It was discerned that annealed GaAs:Ge shows up to ~1-order of magnitude higher PE current than that observed for both untreated and annealed GaAs substrate.

With this method, that is, by annealing Ge on GaAs, the current of electrons extracted with a commercially available low-cost UV-LED of 265 nm increased by up to one order of magnitude compared to that of annealed, untreated GaAs and as-grown GaAs:Ge.

Although, the state-of-the-art Cs negative electron affinity materials are more powerful electron emitters over a wider spectrum while the GaAsGe in our study is only tested for emission from wavelength of 300 nm and shorter. The point made in the manuscript for a specific emitter that does not have the volatility of Cs and could potentially have longer lifetime (opposed to Cs emitters that have to be renewed periodically), trade-off being shorter wavelengths needed for emission.

It has been widely studied that the Cs-O activated GaAs photocathodes have a limited lifetime because of highly sensitive Cs-O oxidant layer. The major cause of degradation in quantum efficient is related to vacuum positioning and ion-back-bombardment during beam operation .[54] In a study by Chanlek et al. [55] it was shown that the QE decreases predominantly due to adsorption of oxygen and oxygen containing species (CO_2 and CO). It was found that the CO degraded the QE by up to 90% and re-caesiating was required to restore the QE up to certain level. Thus, extremely high vacuum environments were needed to minimize the reaction of residual gases with the Cs-O activation layer as to operate reliably for longer time. In contrast, the studied structure in this work was operational at low vacuum levels. Additionally, the ex-situ characterization and storing them at room-temperature in atmospheric ambient for long periods had little if any effect on the PE characteristics of the samples.

4 | EXPERIMENTAL

The current study of Ge on (100) GaAs p-type (Zn doped) wafer was executed to determine the effect of surface reconstruction on photoemission characteristics as a function of annealing parameters. The investigated samples of ~ 10×10 mm² GaAs substrate was initially cleaned using acetone, methanol and isopropanol and later rinsed with de-ionized water followed by blow drying with nitrogen gas. The samples were then deposited with thin Ge film (~10 nm) prior to annealing (thermal treatment).

The deposition of Ge layer (~10 nm as determined via Xray-reflectometry) was carried out by sputtering from an individual target of 99.999% (5N) Ge, using direct current magnetron sputtering (dcMS). For dcMS deposition, Advanced Energy MDX500 power supply was utilized. The targets were positioned at 45° with respect to a flat sample holder at a distance of 200 mm. The substrate was rotated continuously while sputtering to maintain uniform deposition. Prior to deposition, the chamber pressure was throttled to $5×10^{-7}$ Pa. Argon (Ar) gas of 6N purity was used as a working gas. The flow rate for Ar (qAr = 100 sccm) was controlled by mass flow controller and throttle valves were adjusted to stabilize growth pressure of 0.7 Pa during deposition with power maintained at 30 W. The samples were then annealed in air ambient using Heraeus D-6450 Hanau furnace. First an alumina tube was inserted into the furnace which was brought to desired temperature and held there for ~30-60 minutes in order to obtain uniform temperature. The sample was then inserted into the center region of the alumina tube, using a sliding rod. After the desired time of heating, the sample was retracted from the alumina tube and allowed to cool down to room temperature.

4.1 | Characterization

For structural and elemental analysis, the samples were characterized by scanning electron microscopy (SEM) along with electron dispersive X-ray spectroscopy (EDX) by ZIESS Supra 35 and atomic force microscopy (AFM) from Park System (PSIA XE-100). Photoemission measurements were performed by measuring the current over the anode-cathode gap for an applied bias voltage range of -5-210 V. The instrumental setup consisted of Keithley 2400 electrometer, a custom build sample stage assembly, having cathode and an anode on top separated by a distance of ~ 500 μm, along with a computer-controlled UV-LED (~265 nm, 16 mW) from Boston electronics as an illumination source. The sample stage was positioned inside a vacuum chamber and held at vacuum ($< 10^{-5}$ mbar) during measurements. The anode and cathode along with UV-LED were connected to 8-point feedthrough via in-build connectors. The samples, comprising of GaAs:Ge, were coated with gold (Au)- contact (1×3 mm² and ~150 nm in thickness) and a thin aluminum (Al)-wire was attached to it via Ag-paste (Figure 10A). The Au-contacts were deposited via e-beam evaporation (CryoFox 500). A schematic of measurement setup is shown in Figure 10B and is over-drawn for elaboration purpose.

4.2 | Software acquisition

Molecular dynamics (MD) simulations[56] were performed with spherical GaAs nanoparticle using the LAMMPS1,
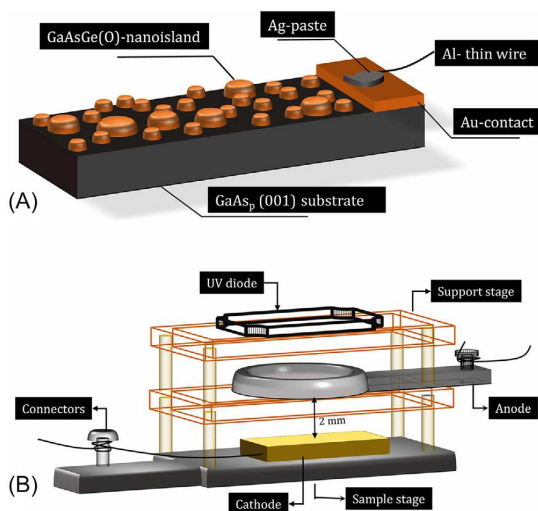
FIGURE 10 Schematic representation of: (A) structure having GaAsGe(O) NIs, coated with Au contact. A thin Al wire is glued to the Au contacts using Ag paste. B, Sample stage incorporated with circular anode and UV-LED. The anode and cathode are fastened to connectors via thin Ag wires which are attached to feedthrough

distribution 7-Aug-2019 open source code available at http://lammps.sandia.gov,[57,58] as to present arsine sublimation at high temperatures. A detailed description regarding MD simulations is provided in supplementary information. Additionally, COMSOL Multiphysics® was utilized, AC/DC module with emphasis on charge conserved electrostatics in anode-cathode electron absorption modeling, used to further elaborate on electron behavior in the system.

ACKNOWLEDGMENTS

CONFLICTS OF INTEREST

We have no conflict of interest to disclose.

DATA AVAILABILITY STATEMENT

Research data are not shared.

REFERENCES

1. D.H. Dowell, I. Bazarov, B. Dunham, K. Harkay, C. Hernandez-Garcia, R. Legg, H. Padmore, T. Rao, J. Smedley, W. Wan, *Nucl. Instruments Methods Phys. Res. Sect. A Accel. Spectrometers, Detect. Assoc. Equip.* **2010**, *622*, 685.
2. C.S. Feigerle, D.T. Pierce, A. Seiler, R.J. Celotta, *Appl. Phys. Lett.* **1984**, *44*, 866.
3. B. Dong, A. Afanasev, R. Johnson, M. Zaghloul, *Sensors* **2020**, *20*, 2419.
4. P. Musumeci, L. Cultrera, M. Ferrario, D. Filippetto, G. Gatti, M.S. Gutierrez, J.T. Moody, N. Moore, J.B. Rosenzweig, C.M. Scoby, G. Travish, C. Vicario, *Phys. Rev. Lett.* **2010**, *104*, 084801.
5. C. Kang, J.W. Leem, I. Maeng, T.H. Kim, J.S. Lee, J.S. Yu, C.S. Kee, *Appl. Phys. Lett.* **2015**, *106*, 261106.
6. O. Steblova, A. Evtukh, O. Yilmazoglu, V. Yukhymchuk, H. Hartnagel, H. Mimura, *Opto-electronics Rev.* **2018**, *26*, 19.
7. K. Sarma, R. Dalby, K. Rose, O. Aina, W. Katz, N. Lewis, *J. Appl. Phys.* **1984**, *56*, 2703.
8. G.-L. Luo, Z.-Y. Han, C.-H. Chien, C.-H. Ko, C. H. Wann, H.-Y. Lin, Y.-L. Shen, C.-T. Chung, S.-C. Huang, C.-C. Cheng, C.-Y. Chang, **2009**, https://doi.org/10.1149/1.3246000
9. H.K. Rasheed, *Appl. Phys. A Mater. Sci. Process.* **2019**, *125*, 1.
10. M.T. Sultan, A. Manolescu, J.T. Gudmundsson, K. Torfason, G. Alexandru Nemnes, I. Stavarache, C. Logofatu, V.S. Teodorescu, M.L. Ciurea, H.G. Svavarsson, *Appl. Surf. Sci.* **2019**, *469*, 870.
11. H. Ye, J. Yu, *Sci. Technol. Adv. Mater.* **2014**, *15*, 024601.
12. V.S. Khoroshilov, D.M. Kazantsev, A.G. Zhuravlev, *J. Phys. Conf. Ser.* **2019**, *1410*, 12128.
13. N. Chanlek, J. D. Herbert, R. M. Jones al -, Z. Jun-Ju, C. Ben-Kang, F. Xiao-Qian, G. photocathodes Zhang Yi-Jun, Z. Ji-Jun, W. Xiao-Hui, *J. Phys. D Appl. Phys* **2014**, *47*, 55110.
14. N. Chanlek, R. J. Cash, B. D. Fell, L. B. Jones, J. W. McKenzie, K. J. Middleman, B. L. Militsyn, *Conf.Proc.C* **2011**, *110904*, 3187.
15. L. Cultrera, A. Galdi, J. K. Bae, F. Ikponmwen, J. Maxson, I. Bazarov, *Phys. Rev. Accel. Beams* **2020**, *23*, 023401.
16. G.A. Mulhollan, J.C. Bierman, *J. Vac. Sci. Technol. B, Nanotechnol. Microelectron. Mater. Process. Meas. Phenom.* **2010**, *28*, 495.
17. W.A. Gutierrez, H.L. Wilson, E.M. Yee. United States Army, US-4286373-A, **1981**
18. H. Schade, H. Nelson, H. Kressel, *Appl. Phys. Lett.* **1971**, *18*, 121.
19. H. Liu, Y. Jin, M. Lin, S. Guo, A.M. Yong, S. Bin Dolmanan, S. Tripathy, X. Wang, *J. Mater. Chem. C* **2018**, *6*, 13059.
20. Y. Sozen, I. Eren, S. Ozen, M. Yagmurcukardes, H. Sahin, *Appl. Surf. Sci.* **2020**, *505*, 144218.
21. Y.B. Cheng, C.K. Chia, Y. Chai, D.Z. Chi, In *Thin Solid Films*, Elsevier, **2012**, pp. 340.
22. W.F. Wang, K.Y. Cheng, K.C. Hsieh, *AIP Adv.* **2018**, *8*, 015230.
23. H.F. Liu, Y.J. Jin, C.G. Li, S.B. Dolmanan, S. Guo, S. Tripathy, C.C. Tan, *RSC Adv.* **2016**, *6*, 52575.
24. C. Heyn, T. Bartsch, S. Sanguinetti, D. Jesson, W. Hansen, *Nanoscale Res. Lett.* **2015**, *10*, 67.
25. Q. Wei, J. Lian, W. Lu, L. Wang, *Phys. Rev. Lett.* **2008**, *100*, 076103.
26. Y.J. Jin, C.K. Chia, H.F. Liu, L.M. Wong, J.W. Chai, D.Z. Chi, S.J. Wang, *Appl. Surf. Sci.* **2016**, *376*, 236.
27. M. Bosi, G. Attolini, C. Ferrari, C. Frigeri, M. Calicchio, F. Rossi, K. Vad, A. Csik, Z. Zolnai, In *J. Cryst. Growth*, North-Holland, **2011**, pp. 367.
28. B. Galiana, I. Rey-Stolle, C. Algora, K. Volz, W. Stolz, *Appl. Phys. Lett.* **2008**, *92*, 152102.
29. L. Kavanagh, C.W. Magee, *Can. J. Phys.* **1987**, *65*, 987.
30. H. Liu, Y. Jin, C. Yang, *CrystEngComm* **2016**, *18*, 4499.
31. A.V Nezhentsev, V.E. Zemlyakov, V.I. Egorkin, V.I. Garmash, *IOP Conf. Ser. J. Phys. Conf. Ser.* **2017**, *917*, 92003.
32. I. Riihimäki, A. Virtanen, H. Kettunen, P. Pusa, J. Räisänen, *J. Appl. Phys.* **2008**, *104*, 123510.
33. J.M. Ryan, J.W. Huang, T.F. Kuech, K.L. Bray, *J. Appl. Phys.* **1994**, *76*, 1175.

34. M. Kateb, M. Azadeh, P. Marashi, S. Ingvarsson, *J. Nanoparticle Res.* **2018**, *20*, 251.

35. M. Azadeh, M. Kateb, P. Marashi, *Comput. Mater. Sci.* **2019**, *170*, 109187.

36. V.P. LaBella, M.R. Krause, Z. Ding, P.M. Thibado, *Surf. Sci. Rep.* **2005**, *60*, 1.

37. J.N. Aqua, I. Berbezier, L. Favre, T. Frisch, A. Ronda, *Phys. Rep.* **2013**, *522*, 59.

38. P. Granitzer, K. Rumpf, K. Rumpf, *Nano Structured Semi Conductors Thesis*, Pan Stanford Publishing, **2014**.

39. C.W. Liu and L.J. Chen, *SiGe/Si Heterostructures in Encyclopedia of Nanoscience and Nanotechnology* (Eds: H. S. Nalwa), American Scientific, New York, NY, *9*, **2004**.

40. S. Kiravittaya, R. Songmuang, A. Rastelli, H. Heidemeyer, O.G. Schmidt, *Nanoscale Res. Lett.* **2006**, *1*, 1.

41. P. Girard, A.N. Titkov, M. Ramonda, V.P. Evtikhiev, V.P. Ulin, *Appl. Surf. Sci.* **2002**, *201*, 1.

42. G. Dushaq, M. Rasras, *Sci. Rep.* **2019**, *9*, 1.

43. A. Navarro-Quezada, A.G. Rodríguez, M.A. Vidal, G. Hernández-Sosa, H. Navarro-Contreras, *Superficies y Vacío*, **2004**, *16*(4), 42–44

44. C. Heyn, D.E. Jesson, *Appl. Phys. Lett.* **2015**, *107*, 161601.

45. Z.Y. Zhou, C.X. Zheng, W.X. Tang, D.E. Jesson, J. Tersoff, *Appl. Phys. Lett.* **2010**, *97*, 121912.

46. Z.M. Wang, B.L. Liang, K.A. Sablon, G.J. Salamo, *Appl. Phys. Lett.* **2007**, *90*, 113120.

47. A.A. Spirina, A.G. Nastovjak, N.L. Shwartz, In *J. Phys. Conf. Ser.*, Institute Of Physics Publishing, **2018**, p. 12011.

48. R. Fornari, C. Frigeri, R. Gleichmann, *J. Electron. Mater.* **1989**, *18*, 185.

49. H. Jung, H. Künzel, K. Ploog, H. Kiinzel, *J. Phys. Colloq.* **1982**, 43.

50. G.R. Lin, C.C. Hsu, *J. Appl. Phys.* **2001**, *89*, 6536.

51. E. Garwin, R. Kirby, C. Sinclair, A. Roder, *Vacuum* **1981**, *31*, 553.

52. D.N. Butcher, B.J. Sealy, *J. Phys. D. Appl. Phys.* **1978**, *11*, 1451.

53. P. Alonso-González, D. Fuster, L. González, J. Martín-Sánchez, Y. González, *Appl. Phys. Lett.* **2008**, *93*, 183106.

54. J. Biswas, E. Wang, M. Gaowei, W. Liu, O. Rahman, J.T. Sadowski, *AIP Adv.* **2021**, *11*, 025321.

55. N. Chanlek, J.D. Herbert, R.M. Jones, L.B. Jones, K.J. Middleman, B.L. Militsyn, *J. Phys. D. Appl. Phys.* **2014**, *47*, 7.

56. M.P. Allen, D.J. Tildesley, *Computer Simulation of Liquids*, Oxford university press, **2017**

57. S. Plimpton, *J. Comput. Phys.* **1995**, *117*, 1.

58. S.J. Plimpton, A.P. Thompson, *MRS Bull.* **2012**, *37*, 513.

SUPPORTING INFORMATION

Additional supporting information may be found online in the Supporting Information section at the end of the article.

72

Paper III

Facile formation of self-assembled Ga droplets on GaAs (001) substrate

M. T. Sultan[*], **H. Ö. Árnason**[†], **S. Ingvarsson**[*], **U. B. Arnalds**[*], **H. G. Svavarsson**[†], **A. Manolescu**[†] **and A. Valfells**[†]

[*]Science Institute, University of Iceland, Reykjavík, Iceland
Email: muhammad@hi.is
[†]Department of Engineering, Reykjavík University, Reykjavík, Iceland
Email: hakona07@ru.is

Abstract—**We investigate the formation and evolution of Ga droplets over GaAs (001) substrate with and without Ge top layer (8 nm). Various morphological transformation from holes to droplets formation were observed as a function of annealing parameters. It was observed that the application of Ge layer plays a vital role in incorporating oxygen into the system. Moreover, a potential application of these structures as a photocathode is discussed, demonstrating increased photoemission.**

Index Terms—**Ga droplet, Germanium, RTA, SEM**

I. INTRODUCTION

Self-assembled nanostructures has attracted great interest over the last decades with application in solid-state devices for instance sensors, optical and storage devices [1], [2]. Devising materials system at the nanoscale modifies the optical and electrical properties by inducing low-dimensional charge carrier confinement which can be used to enhance CMOS technology [3].

A classic example of such self-structuring is that of Germanium silicon (Ge_xSi_{1-x}) nanoislands [4]. Another emerging class of self-assembly is droplet-epitaxy [5], [6], which is composed of the initial formation of metallic droplets by vacuum annealing followed by crystallization into that of semiconductor nanoislands via quenching [1]. An interesting example of such droplet formation is that of Gallium (Ga) droplets. The dynamics of Ga droplet formation and coalescence on surfaces at ambient temperature is an active field of research. Langmuir decomposition of Gallium arsenide (GaAs) (001) where the surface evaporates in vacuum is a well defined example of phase separation [5].

The aim of this study is to determine the effect of annealing parameters on the restructuring of GaAs surfaces with and without a thin Germanium (Ge) top layer. Moreover, a possible application of such structures as a photocathodes operating under illumination from a simple ultraviolet (UV) (∼262 nm) diode has been recently proposed [7].

II. MATERIALS AND METHODS

For this study GaAs (001) p-type substrates (∼1×1 cm^2) were utilized. Piece of GaAs were annealed in a rapid thermal process (RTA) before and after deposition of Ge film (∼8 nm). The deposition of the Ge layer was carried out by sputtering from an individual Ge target of 99.9999% (6N) purity, using direct current magnetron sputtering (dcMS) at 30 W. For the dcMS deposition an Advanced Energy MDX500 power supply was utilized. Argon (Ar) gas of 5N purity was used as a working gas. The flow rate for Ar (q_{Ar}= 40 sccm) was controlled by a mass flow controller and throttle valves were adjusted to stabilize the growth pressure of 0.7 Pa during deposition. The structures were characterized via scanning electron microscopy (SEM) and energy dispersive X-ray spectroscopy (EDS).

III. RESULTS AND DISCUSSION

The GaAs substrates were annealed without Ge layer at 550 °C for 30, 60 and 90 sec and at 600 and 650 °C for 60 sec. SEM images for respective structures are shown in Fig. 1. For low annealing temperature and time (i.e., T=550 °C and t=30 sec) randomly distributed nanoholes (Fig. 1a) were observed which with increased t, resulted in the formation of assemblies of rectangular shaped pits with rounded heads (Fig. 1b), aligned along the ± [110] directions. For such geometries it was observed that the depth gradually increases from the head of the pit towards the rectangular base. The EDS analysis revealed that the Ga - As concentration is slightly higher (52/48 wt%) at the rectangular base than in the head regime (49/51 wt%).

With increased time to t=90 sec, Ga droplets (having a small amount of As, 87/13 wt%) were formed within the pits at the rectangular base region where the Ga concentration was higher (Fig. 1c). Similar observation of hole and droplet in hole formation has also been observed by Liu *et al.* [6]. The EDS analysis was carried at various reference spots in order to verify the elemental composition. Increasing T to 600 °C (Fig. 1d) ultimately resulted in the formation of Ga droplets (with no trace of As), enclosed within As rich GaAs ridges, (47/53 wt%), along with a smooth surface around the droplets (rich in Ga). Additionally, the boundaries still have rectangular etch pits which restrict the droplet, as it is rich of As. When increasing the annealing temperature T to 650 °C (see Fig. 1e), self-running Ga droplets with increased sizes were obtained. An evident trail along the moving path of the Ga droplets is visible in Fig. 1e and f.

The formation of the Ga droplets can be explained with respect to the congruent temperature (T_c) [8]. That is, there
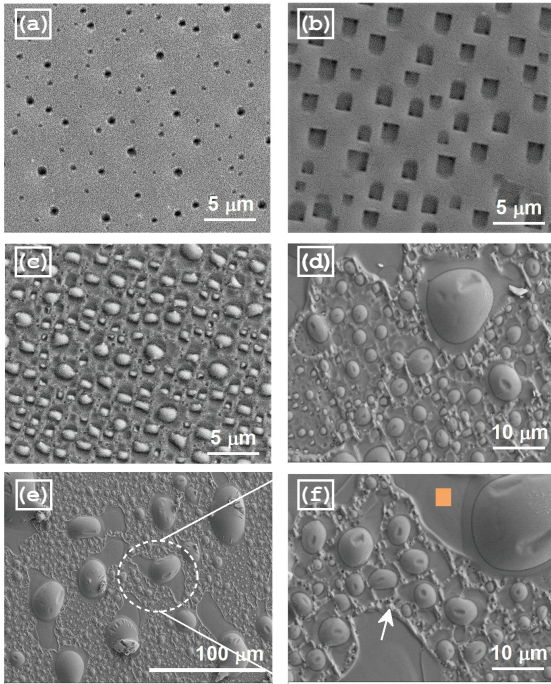
Fig. 1. SEM image for the structures annealed at (a-c) 550 °C for 30, 60, and 90 sec, (d-e) 650 and 700 °C for 60 sec. (f) Magnified image of the highlighted area in (e), arrow pointing at the ridges (orange area is EDS scan).

exists a typical temperature range when the evaporation is congruent, i.e. where the Ga and As leaving the surface is equal [5], [9]. However, above T_c the evaporation rate for As on the surface exceeds that of Ga, thus leaving behind Ga-rich liquid droplets [5], [9]. It was determined that the running Ga droplets occur spontaneously after annealing the GaAs (001) in vacuum.

This motion is a characteristic of disequilibrium induced between the Ga droplet and the surrounding surface and it is assigned to a stick and slip character of droplet motion [8], [10]. Initially a small droplet is formed by absorbing Ga through the surface, by diffusion from the substrate beneath through melting. This in turn increases the droplets volume, thereby altering the interfacial area of the droplet. When the surface tension of the droplet reaches a threshold of holding a cohesive body (because of forces developed due to surface energy difference), random disruption triggers the droplet surface to breakout thus releasing Ga droplet to flow over some distance. This corresponds to a 'slip' in the stick and slip motion [10]. It is well known for droplets on GaAs (001) surfaces, that they will move preferentially in ± [110] directions leaving behind a smooth atomically flat trail of fresh GaAs surface [8], [10] (as can be seen in Fig. 1f and 2b). The mature droplet forms a solid-liquid interface with the substrate; hence the crystal anisotropy is in effect confining the droplet

contact-line along the ±[110] direction on the GaAs (100) surface.

For the structures comprised of Ge on GaAs, a similar annealing treatment was carried out. In this case, the diffusion of Ge into GaAs will tend to act as an amphoteric dopant [11]. The formation of Ga droplets on the surface having a thin Ge layer is most likely due to phase separation and surface segregation of Ga due to the low solubility of Ga in Ge [12], whereas the Ge segregates and diffuse (down to few micron) into bulk GaAs through Ga vacancies [7], [13].

Similarly to GaAs, annealing of Ge:GaAs structure at 550 °C for 60 sec, resulted in the formation of Ga droplets (with a small concentration of As, 83/17 wt%) arranged in the ±[110] direction at the rectangular base (Fig. 2a and c). The Ga droplets are immobile due to the surrounding As rich boundaries. The regime adjacent to droplets i.e., smooth surface, are Ga rich GaAs, where the Ga concentration increases as we move towards the Ga droplets.

Later, when the samples were annealed at 600 °C for 1 min (Fig. 2b and d), the structures showed a different morphology of droplets surrounded by evenly shaped boundaries. One can evidently see from Fig. 3 that the region from the droplet to the surrounding periphery comprises four different regions with systematically varying Ga:As ratio (shown by the numbered sites) as determined by EDS analysis. At site (1, 2), the EDS shows pure Ga (98.02 wt%) with a small amount of oxygen present (1.98 wt%).

Moving away from the droplet (i.e., from the droplet edge towards the boundaries) revealed the presence of fair amount of As which increases as we move further towards the boundaries (which as mentioned earlier are rich in As without any evidence of oxygen). Similar behavior is observed for structures annealed at 650 °C for 60 sec, all though with reduced height of boundaries surrounding the droplets, Fig. 2e. It can be seen from the structure annealed from low temperature to 650 °C that the structure displays no appearance of extra small droplets around or in the vicinity of already present droplets.

Increasing the annealing temperature from 700 to 750 °C (not shown here) for 60 sec (Fig. 2f) resulted in the reduction and eventually the disappearance of boundaries surrounding the droplets. These boundaries, upon exposure to high annealing temperatures, results in areas of small evolving Ga droplets, while the bigger droplets are are separated and sitting in a smooth crater. Further more the EDS analysis showed that the Ga droplets obtained with T ranging from 600 to 750 °C, included minor quantities of oxygen (i.e., GaO_x). Such an incorporation of oxygen in the structure can be explained in light of a study by Wang *et al.* [10], where the diffusion of oxygen in Zn-doped GaAs (001) was studied in the presence of Ge and As_2O_3-rich ambient. There the incorporation was attributed to Ge-O pairs which possess a lower vapor pressure than arsenic oxide. Further, the bond dissociation energy of Ge-O 662 kJmole^{-1} is much higher then Ga-O, thus can strongly be coupled and incorporated into the structure.

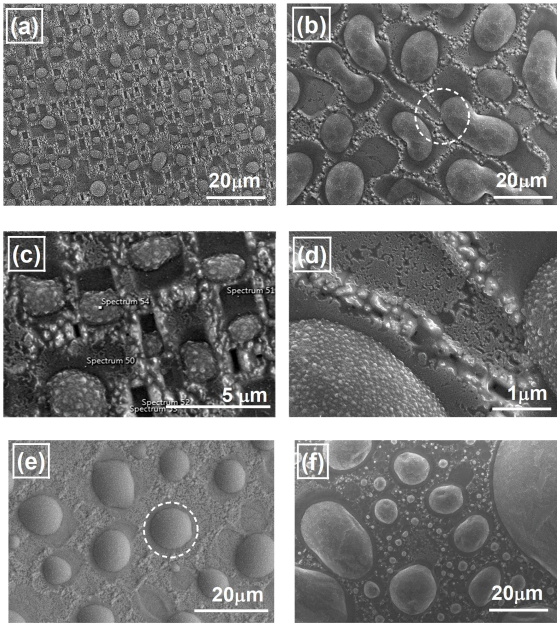The GaAs:Ge structures were utilized to realize them as a

Fig. 2. SEM images for Ge:GaAs structures annealed at (a, b, e, f) 550, 600, 650, and 700 °C for 60 sec. (c, d) Magnified view of the structures in (b).

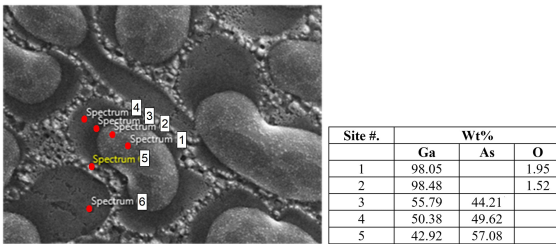| Site #.	Wt%		
	Ga	As	O
1	98.05		1.95
2	98.48		1.52
3	55.79	44.21	
4	50.38	49.62	
5	42.92	57.08	

Fig. 3. SEM image for the structure annealed at 600 °C for 60 sec as in Fig. 2b, along with tabulated EDS analysis carried out at numbered spots, from the center of droplets towards the boundaries.
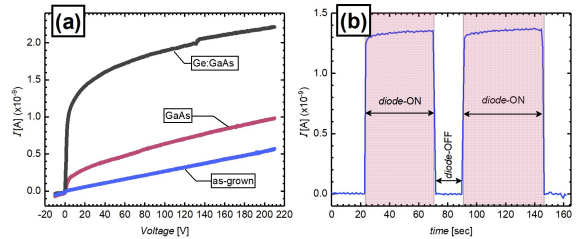

Fig. 4. (a) Photoemission current (I) characteristics as a function of applied bias of as-grown Ge:GaAs and annealed (600 °C, 60 sec) GaAs and Ge:GaAs structures at room temperature under 10^{-3} Pa. (b) Responsivity under illumination by 262 nm UV-diode.

their quantum efficiency is prone to degrade due to the high sensitivity of Cesium oxide layer because of vacuum poisoning or back-bombardment of ions during the operation [14], [15].

IV. CONCLUSION

In summary, the morphological evolution of Ga droplets taking place during rapid thermal annealing of GaAs (001) was studied. It was observed that self-running Ga droplets tended to form upon annealing leaving behind a fresh GaAs surface, where the distance is restricted by As rich boundaries. The deposition of thin Ge film on GaAs exhibited similar droplet evolution but, the Ge tends to incorporate oxygen in to structure, forming GaO_x droplets.

The studied structures provide a simple and cost effective method to obtain photoemission by using a commercially available low-cost UV-diode. However, further analysis is under investigation as to improve the structural stability and emission response by effectively increasing the quantum efficiency.

ACKNOWLEDGMENT

REFERENCES

[1] M. Jo, T. Mano, Y. Sakuma, and K. Sakoda, "Size-dependent contact angle of Ga droplets on GaAs," *Journal of Crystal Growth*, vol. 378, pp. 5–7, sep 2013.

[2] Q. Wei, J. Lian, W. Lu, and L. Wang, "Highly ordered Ga nanodroplets on a GaAs surface formed by a focused ion beam," *Physical Review Letters*, vol. 100, p. 076103, feb 2008.

[3] I. Berbezier, A. Ronda, and A. Portavoce, "SiGe nanostructures: New insights into growth processes," *Journal of Physics Condensed Matter*, vol. 14, pp. 8283–8331, sep 2002.

[4] J. N. Aqua, I. Berbezier, L. Favre, T. Frisch, and A. Ronda, "Growth and self-organization of SiGe nanostructures," *Physics Reports*, vol. 522, no. 2, pp. 59–189, 2013.

[5] B. A. Trisna, N. Nakareseisoon, W. Eiwwongcharoen, S. Panyakeow, and S. Kanjanachuchai, "Reliable synthesis of self-running Ga droplets on GaAs (001) in MBE using RHEED patterns," *Nanoscale Research Letters*, vol. 10, pp. 1–7, dec 2015.

[6] H. Liu, Y. Jin, and C. Yang, "Droplet-induced dot, dot-in-hole, and hole structures in GaGe thin films grown by MOCVD on GaAs substrates," *CrystEngComm*, vol. 18, pp. 4499–4507, jun 2016.

[7] M. T. Sultan, H. Ö. Árnason, M. Kateb, A. Manolescu, H. G. Svavarsson, and Á. Valfells, "Enhanced photoemission from surface modulated GaAs:Ge," *Nano Select*, may 2021.

potential candidate for photoemission (PE) application. A detailed description of the measurement setup, and data analysis for GaAs:Ge nanostructures can be found elsewhere [7] Fig. 4 shows a comparison between room temperature photoemission under UV-illumination as a function of applied bias for GaAs with and without Ge, annealed at 600 °C, 60 sec, along with responsivity (PE under UV-diode ON/OFF state).

Almost an order of magnitude increase in PE intensity was observed for Ge:GaAs structures compared to GaAs, and can be attributed to droplet formation exhibiting quantum confinement having low electron emission barrier and increased hole mobility induced by Ge [7]. Although negative electron affinity diodes (e.g. cesiated GaAs) are more powerful, they require complex setups for fabrication and packaging. Additionally,

[8] C. Heyn and D. E. Jesson, "Congruent evaporation temperature of molecular beam epitaxy grown GaAs (001) determined by local droplet etching," *Applied Physics Letters*, vol. 107, p. 161601, oct 2015.

[9] J. Wu, Z. M. Wang, A. Z. Li, M. Benamara, S. Li, and G. J. Salamo, "Nanoscale footprints of self-running gallium droplets on GaAs surface," *PLoS ONE*, vol. 6, no. 6, p. 20765, 2011.

[10] W. F. Wang, K. Y. Cheng, and K. C. Hsieh, "Germanium diffusion with vapor-phase GeAs and oxygen co-incorporation in GaAs," *AIP Advances*, vol. 8, p. 15230, jan 2018.

[11] M. Bosi, G. Attolini, C. Ferrari, C. Frigeri, M. Calicchio, F. Rossi, K. Vad, A. Csik, and Z. Zolnai, "Effect of temperature on the mutual diffusion of Ge/GaAs and GaAs/Ge," in *Journal of Crystal Growth*, vol. 318 Issue 1, pp. 367–371, North-Holland, mar 2011.

[12] J. Tersoff, D. E. Jesson, and W. X. Tang, "Running droplets of gallium from evaporation of gallium arsenide," *Science*, vol. 324, pp. 236–238, apr 2009.

[13] A. V. Nezhentsev, V. E. Zemlyakov, V. I. Egorkin, and V. I. Garmash, "Diffusion theory and optimization of ohmic contacts to n-layer of bipolar nanoheterostructures," in *Journal of Physics: Conference Series*, vol. 917 Issue 9, p. 092003, Institute of Physics Publishing, nov 2017.

[14] N. Chanlek, J. D. Herbert, R. M. Jones, L. B. Jones, K. J. Middleman, and B. L. Militsyn, "The degradation of quantum efficiency in negative electron affinity GaAs photocathodes under gas exposure," *Journal of Physics D: Applied Physics*, vol. 47, p. 55110, feb 2014.

[15] J. Biswas, E. Wang, M. Gaowei, W. Liu, O. Rahman, and J. T. Sadowski, "High quantum efficiency GaAs photocathodes activated with Cs, O2, and Te," *AIP Advances*, vol. 11, p. 25321, feb 2021.

78

Paper IV

Communication

Piezoresistance Characterization of Silicon Nanowires in Uniaxial and Isostatic Pressure Variation

Elham Fakhri [1,*], Rodica Plugaru [2], Muhammad Taha Sultan [1,3], Thorsteinn Hanning Kristinsson [1], Hákon Örn Árnason [1], Neculai Plugaru [2], Andrei Manolescu [1], Snorri Ingvarsson [3] and Halldor Gudfinnur Svavarsson [1,*]

[1] Department of Engineering, Reykjavik University, Menntavegur 1, 102 Reykjavik, Iceland
[2] National Institute for Research and Development in Microtechnologies-IMT Bucharest, 077190 Voluntari, Romania
[3] Science Institute, University of Iceland, Dunhaga 3, 107 Reykjavik, Iceland
[*] Correspondence: elhamf20@ru.is (E.F.); halldorsv@ru.is (H.G.S.)

Abstract: Silicon nanowires (SiNWs) are known to exhibit a large piezoresistance (PZR) effect, making them suitable for various sensing applications. Here, we report the results of a PZR investigation on randomly distributed and interconnected vertical silicon nanowire arrays as a pressure sensor. The samples were produced from p-type (100) Si wafers using a silver catalyzed top-down etching process. The piezoresistance response of these SiNW arrays was analyzed by measuring their I-V characteristics under applied uniaxial as well as isostatic pressure. The interconnected SiNWs exhibit increased mechanical stability in comparison with separated or periodic nanowires. The repeatability of the fabrication process and statistical distribution of measurements were also tested on several samples from different batches. A sensing resolution down to roughly 1 mbar pressure was observed with uniaxial force application, and more than two orders of magnitude resistance variation were determined for isostatic pressure below atmospheric pressure.

Keywords: silicon nanowires; MACE; piezoresistivity

1. Introduction

Low-dimensional structures may possess unique mechanical, electrical, optical, and thermoelectric properties. Particularly, silicon nanowires (SiNWs) have demonstrated properties suitable for various advanced applications [1–3], including low-cost thermoelectric devices and chemo-biological sensors with ultrahigh sensitivity [4,5]. The integration of SiNWs in electronic devices is favoured by their compatibility with the well-established Si-SiO$_2$ electronic industrial technology. Bulk silicon has been known for a while to exhibit high piezo resistance (PZR) effect [6]. In bulk semiconductors, the PZR-effect takes place, in principle, due to a change in the electronic structure and modification of the charge-carriers effective masses. This phenomenon has found practical applications in many Si-based devices, such as pressure transducers [7], cantilevers for atomic force microscopy [8], accelerometers [9], biosensors [10], and multi-axis force sensing tools [11].

Recently, nanowires have been shown to possess the ability to significantly increase the PZR response [12]. A giant PZR was observed in p-doped SiNWs with diameters of 50 nm to 350 nm and a length of microns initially under tensile uniaxial stress [13]. However, the PZR effect in n-doped nanowires was found to be comparable to that in the bulk counterpart, both for tensile and compressive uniaxial stress [14].

On the theoretical side, the origin of the PZR effect in SiNWs has long been under debate, and most frequently, it is referred to as anomalous PZR [15]. It has been related to quantum confinement effects [16], surface charge effects [17–19], strain-induced bandgap shift [20], or changes in the charge carrier's effective masses [21]. A complex model

incorporating these mechanisms has been proposed in order to analytically quantify the PZR effect in silicon [22].

A survey of several PZR sensors based on SiNWs, e.g., cantilever [23], opto-mechanical sensor [24], flexible pressure sensor [18], or breath detector [19], shows that different methods have been used for fabricating the SiNWs, such as vapor-liquid-solid (VLS), laser ablation, and metal-assisted catalyzed etching (MACE) [25]. Among these methods, MACE is the simplest and most versatile one [26]. It relies on catalyzed etching with assistance from a perforated metal template film (typically gold or silver) [27] or randomly distributed metallic nanoparticles (typically gold or silver) [28,29] spread on the Si-wafer. To date, studies have been focused on using different gas types to apply direct pressure on SiNWs, either single SiNW or arrays of SiNWs [19,30], and have neglected the SiNWs response under isostatic pressure, which creates a load uniformly distributed on the sample surface. Here, we report on the PZR effect in SiNWs obtained by MACE under uniaxial compression load as well as isostatic pressure in a vacuum chamber. We find that the interconnected SiNWs are mechanically stronger and functionally more stable compared with the arrays of separated wires under applied uniaxial pressure. They show higher PZR sensitivity under isostatic pressure variation. We also demonstrate a simple, low-cost, and reproducible fabrication method for a robust and sensitive pressure sensor.

2. Materials and Methods

2.1. Fabrication of SiNWs

Arrays of interconnected SiNWs were fabricated by silver (Ag) MACE in a three-step process, from p-type, single-side polished 525 µm-thick Si wafers, with resistivity, ρ, of $10\,\Omega\,cm$ to $20\,\Omega\,cm$. The nanowire patterns were made on areas of about $1\,cm^2$ on the polished side of the wafers. The sequence of steps used to prepare the SiNW areas is as follows:

1. Deposition of metal catalyst: Ag nanoparticles were deposited on the surface of the Si wafers by immersing the wafers in a solution of $3\,M$ HF and $1.5\,M$ $AgNO_3$ for $60\,s$.
2. Wire etching: The samples were etched by immersing them in $HF:H_2O_2$ (5M:0.4M) solution to obtain vertically aligned SiNWs.
3. Removal of residual Ag nanoparticles: Samples were immersed in 20% *w/v* HNO_3 to remove residual silver particles. A more detailed description can be found in Refs. [28,29].

Subsequently, 150 nm-thick aluminum electrodes were deposited on the samples by electron beam evaporation (Polyteknik Cryofox Explorer 600 LT). For the uniaxial measurements, the electrodes were deposited on the top and backside of the samples, while for the isostatic pressure measurements, the electrodes were made co-planar.

Four sets of interconnected SiNWs samples, denoted as follows, were prepared by varying the etching time: A (1 min), B (3 min), C (5 min), and D (7 min) were made for uniaxial pressure application, and sample E (40 min) was made for isostatic pressure testing.

Additionally, periodic SiNWs, such as sample F, were made as described in the Supplementary Material. Table 1 shows the list of the samples with corresponding etching times and length.

A scanning electron microscope (SEM, Zeiss Supra 35) was used to characterize the SiNW's geometry. Top and cross-sectional SEM images were used to estimate the average diameter of the wires. The Gwyddion software for data visualization and analysis was applied to surface SEM images in order to estimate the total top area of the wires. Figure 1 shows (a,b) the cross-section of the wire array and (c) the surface area of SiNWs obtained after 7 min etching. It is worth mentioning here that the SEM analysis was carried out on the sample prior to the removal of Ag nanoparticles, which are visualized as bright spots at the base of the nanowires in the cross-section.

Table 1. List of samples with different etching times and corresponding lengths. Samples A, B, C, D, and E are random wires, and sample F is with periodic wires (shown in the Supplementary Material).

Sample	Etching Time (min)	SiNW Length (µm)
A	1	0.7
B	3	1.5
C	5	2.2
D	7	3
E	40	10
F	5	0.65

As can be seen in the top-view image, the wires are partly interconnected, forming a continuous rigid structure. Further, also seen from place to place are free-standing nanowires forming bundles. Such bundle formation may take place because of capillary forces acting during the drying process following the wet-etching step. In the cross-sectional image, one may observe that the length of the wires is relatively homogeneous, around 3 µm, and their typical diameter is approximately 150 nm. According to Peng et al. [5], porosity plays an essential role in the PZR response, which increases with increased porosity. The porosity is most conveniently controlled by the concentration of Ag deposition solution and etching time. In a previous study [28], it was demonstrated that the SiNWs porosity was highly affected by the concentration of the $AgNO_3$ during the Ag deposition. A 1.5 mM $AgNO_3$ (as used for samples A–D) provided highly porous SiNWs with maximum photoluminescence spectra intensity.
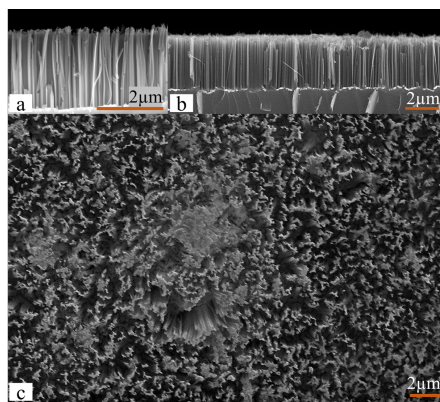

Figure 1. SEM image of SiNWs etched for 7 min (**a**), high-magnification cross-section of the same image (**b**), and (**c**) top-view SEM image of SiNWs etched for 7 min.

From the SEM image analysis, the wire's cross-sectional surface coverage was estimated at roughly 28% by using the Gwyddion program, Figure 2. By counting the average number of wires on several line scans, the wire density was estimated to be 1.6×10^7 mm^2, which corresponds to roughly 8×10^8 wires under the force meter area (7 × 7 mm).

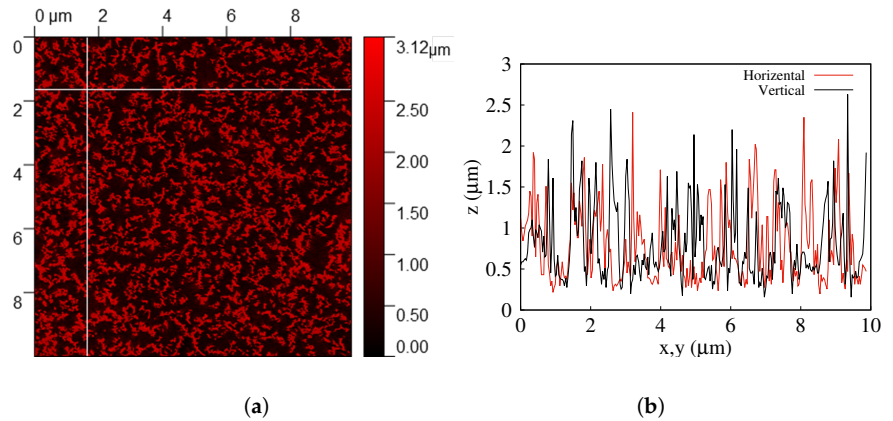(**a**)   (**b**)

Figure 2. (**a**) Gwyddion analysis of top-view SEM image in (100 μm^2). (**b**) Two Gwyddion line-scans of the figure to the left (red color—horizontal axis, black color—vertical axis).

2.2. Measurement Setups

For uniaxial PZR tests, the samples were clamped between a metal pin of a force meter (Mark-10, M5-012), touching the top side of the samples, and a rigid copper (Cu) plate at the backside, as shown in Figure 3. In order to improve the electrical contacts, the samples were glued to the Cu backside plate with silver paste. The force meter was mounted on a vertical rod allowing for movement on the *z*-axis (vertical) by a manually adjusted screw. Uniaxial pressure was applied to the samples by pressing the pin of the force meter into the samples' surface with an intensity determined by the aforementioned screw. The applied force was in the range of 100 mN to 900 mN on an area of 7×7 mm (the cross-sectional area of the pin). Taking the wire coverage (28 %) into account, this corresponds to a gauge pressure of 7 kPa to 66 kPa. Figure 3 shows a sketch of the experimental setup. A Keithley 2400 SourceMeter was used to measure the resistance *R* through the sample as a function of applied pressure at a constant bias voltage of 2 V.
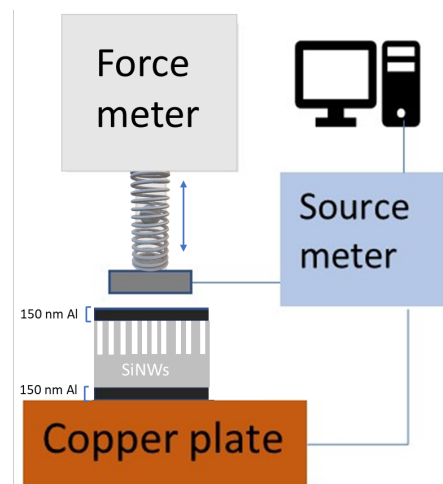

Figure 3. Schematic of the force meter setup for testing PZR characteristics.

For PZR tests under isostatic pressure variation, a vacuum chamber was used, and the air was removed while the resistance was measured at a fixed 5 V. In this case (for sample E), the contacts were made in co-planar configuration, with separate contacts on each side

of the patterned area, such that the nanowires are maximally exposed to air instead of top-and-bottom contacts as for the uniaxial measurements (performed with samples A–D). Furthermore, the wire length was increased (to 10 µm) to increase the surface area exposed to the air. The samples were mounted on a fixed sample station inside the chamber with tungsten needle tip kelvin probes as a connection.

3. Results

3.1. Electrical Response under Uniaxial Force

A maximum force of approximately 900 mN was applied to the samples using the setup shown in Figure 3. The maximum vertical force exerted on each wire thus corresponds to $900 \times 10^{-3}\,\text{N}/8 \times 10^8 \approx 1.1 \times 10^{-9}\,\text{N/wire}$ or $6.6 \times 10^4\,\text{Pa}$ (0.65 bar).

The force and the instantaneous resistance measured after applying the force to the sample with nanowires of length 3 µm (etched for 7 min) are shown in Figure 4a as a function of time. The maximum force was applied at the beginning (time zero) and then reduced step-wise while the resistance was being measured. Each force level was kept constant for roughly 50 s to confirm that the resistance value was stable with time. As clearly visible, the resistance changes significantly and inversely with pressure.
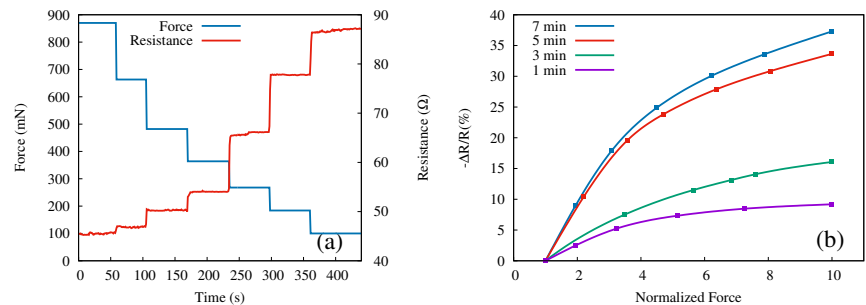

Figure 4. (**a**) Instantaneous resistance (right y-axis, red line) in response to applied force (left 4-axis, blue line) over time for sample D. (**b**) Relative resistance change versus normalized force for SiNWs samples A (purple), B (green), C (red), and D (blue).

We define the relative resistance change vs. force variation for each step $k = 1, 2, \ldots$ as

$$\frac{\Delta R}{R} = \frac{R_k - R_1}{R_1}, \tag{1}$$

where R_k is the average resistance obtained for the constant force step k. The measurements were repeated four times on each sample (A, B, C, D), each time reproducing the force steps as well as possible with the adjustable screw. A second average, this time of the relative resistance in step k, defined by Equation (1), obtained for the four measurements vs. the average normalized forces for each step, is presented in Figure 4b. Here, by normalized force, we mean the ratio of the force in a particular step k to the initial force, F_k / F_1. Hence, the maximum force values for each step-wise measurement are normalized to unity. Note that the resistance decreases when the force increases and that in Figure 4b, we show the negative of $\Delta R / R$.

Increasing the length of the nanowires (by increasing the etching time) leads to higher relative resistance, although the trend appears to saturate; only a relatively small difference between the 5 min and 7 min samples has been obtained. The highest relative change (37.3%) in resistance is observed for the longest etching time (sample D) with regards to uniaxial pressure.

In Figure 5, the resistance versus applied force is shown again for sample D (blue line), now compared with the case of the bulk Si (red line). For this measurement, we replicated sample D four times, in the same conditions of a 7 min etching time, and performed the

measurements on each sample replica. These measurements have been performed to test the repeatability of the sensor's response in the same conditions as have been performed in Figure 4a. It is worth noting that the un-uniform step size observed in Figure 4a is due to the manually adjustable screw of the force meter shown in the schematic. The data displayed are average values measured on these samples (D-like), shown with the error bars. A striking difference between these two configurations (SiNWs vs. bulk Si) is observed. No measurable change in resistance is seen for the bulk Si, in very sharp contrast to the SiNWs sample.
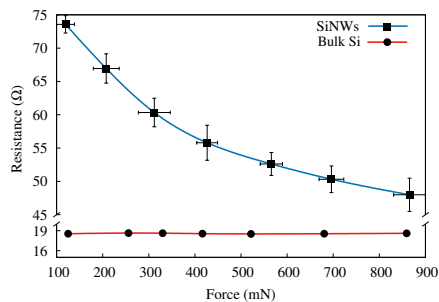

Figure 5. Resistance vs. applied force for the D-like samples (blue line) and bulk-Si (red line). Data for SiNWs are average values of four distinct samples; the error bars show the range in which the measurements fell.

Up to a 35 % change in resistivity was observed over the pressure variation in the range of 0.1 N to 0.9 N. In order to test the stability of SiNW's PZR response and response time, we performed several sets of measurements over different samples. In this stability test, the resistance shift was measured in periods of 60 s of loading and unloading force for all the samples. All samples were loaded by 860(10) mN and then unloaded to 220(10) mN. We observe a fast response (below 0.5 s), good stability, and high sensitivity to repeated pressure changes. The results of a reproducibility test for sample D are presented in Figure 6.
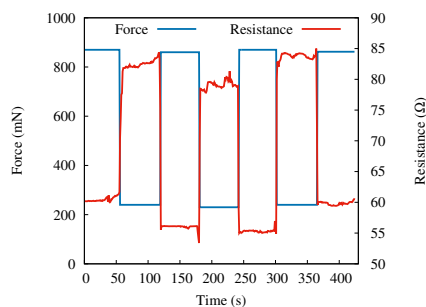

Figure 6. SiNWs PZR response due to repeated load–unload forces in real time for sample D.

Hydrogenation (exposure to hydrogen plasma) is widely used in the electronic industry to increase the mobility of charge carriers in semiconductors. It neutralizes deep and shallow defects and charged surface states [31,32]. Because the PZR effect has been attributed to surface states, we applied a hydrogenation treatment in order to explore the origin of the PZR effect in SiNWs. For hydrogen plasma treatment, we used a custom-built inductively coupled discharge setup with cylindrical geometry (290 mm long quartz tube with a diameter of 34 mm). The quartz tube was held inside a circular copper inductive coil with a diameter of 54 mm. A radio-frequency power generator CERSAR (c) (13.56 MHz) source coupled with an impedance-matching unit was utilized. For hydrogenation, a gas

mixture of Ar/H_2 (30 / −70%) was used, and the throttle valves were adjusted to stabilize the gas pressure of 29 mbar. A more detailed description and schematic of the hydrogenation setup can be found elsewhere [33,34]. In Figure 7, we compare the behavior of sample D before and after the hydrogenation. The PZR effect decreases dramatically and can be attributed to the passivation of the surface states [35].
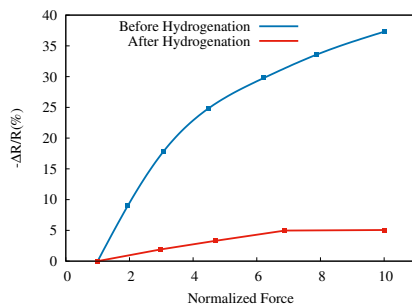

Figure 7. SiNWs PZR response for sample D before and after hydrogenation.

3.2. Electrical Response under Isostatic Pressure

Sample E (10 μm) was used for the investigation of the PZR response to isostatic pressure in a vacuum chamber. The PZR response was tested in the chamber under re-pressurizing conditions in the range of 10^{-4} mbar to 10^3 mbar. The results are shown in Figure 8, where the resistance is plotted as a function of the pressure measured at a fixed bias voltage of 5 V. We observed a dramatic increase in the resistance by more than two orders of magnitude when pumping the air out of the vacuum chamber. We believe this is a result of combined mechanical and chemical effects: the pressure drop removes mechanical stress, and the lack of air and humidity suppresses the chemisorption. Note that the resistance values for sample E are much higher than for samples A–D because of the co-planar configuration of the contacts and also because of the larger length of the nanowires.

In the Supplementary Material we show, for comparison, the behavior of periodic arrays of SiNWs with increasing isostatic pressure.
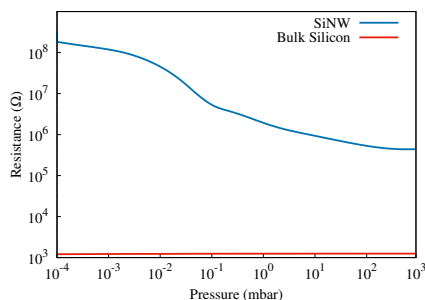

Figure 8. The resistance of sample E (on a log 10 scale) as a function of pressure measured in the vacuum chamber is shown with the blue curve. For comparison, in red, the resistance of a bulk silicon sample (i.e., without nanowires).

4. Discussion

For solid materials, the inter-atomic spacing may be altered by strain. Consequently, apart from geometric changes in semiconductors, bandstructure-related details, such as bandgap or effective mass, may change, and thereby the resistivity may change as well. An applied strain changes the bandgap and the effective mass of charge carriers, which, in

turn, affect the carrier concentration as well as their mobility [36]. Within a certain range of strain, this relationship is linear [22,37]. Niquet et al. [36] show that electron mobility saturates with strain. Subsequently, the PZR response saturates above a certain range of strain. When a uniaxial stress X is applied, the piezoresistance coefficient of the resistivity ρ in the direction of stress is defined as

$$\pi_l = \frac{\Delta\rho}{\rho_0}\frac{1}{X}\,, \tag{2}$$

where $\Delta\rho$ is the stress-induced change in the resistivity and ρ_0 is the reference resistivity of the unstressed material.

In our case, a uniaxial compressive force F was applied to SiNWs along their length by a force meter. The stress is $X = F/A_t$, A_t being the total cross-sectional area of the nanowires, which is equal to pA_m, where A_m is the cross-sectional area of the pin pressed into the wires, and p is the relative cross-sectional area of the wires. Assuming the electrical resistivity of the nanowires is proportional to their resistance, Equation (2) becomes

$$\pi_l = \frac{pA_m}{F} \times \frac{\Delta R}{R_0}\,. \tag{3}$$

The structure of our SiNWs array is robust and stable as the wires are partially interconnected, which provides high structural strength. Such stability and fast response of SiNWs is a desired property for many devices, such as solid-state accelerometers and bipolar transistors [38]. Further, our results are in agreement with the study of Ghosh et al. [19], in which large-diameter Si nanorod-based sensors were used for force detection.

He et al. [13], who measured PZR coefficients of single (p-doped) SiNWs, with diameters 50 nm to 300 nm, made from wafers with resistivities of 0.003 Ω cm to 10 Ω cm, found that the PZR was roughly inversely proportional to the diameter and proportional to the wafer resistivity. For a similar diameter and wafer resistivity as in our present work, $\sim$150 nm and 10 Ω cm, respectively, the PZR coefficient π_l for a single wire was of the order 10^{-7} Pa^{-1}. (According to Figure 2d of Ref. [13]). Using Equation (3), with $p = 0.28$, $A_m = 49$ mm^2, $F = 0.8$ N, and $\Delta R/R = 0.35$, we obtain $\pi_l \approx 6 \times 10^{-6}$ Pa^{-1}, i.e., almost two orders of magnitude higher. Note that, in principle, Equation (2) does not depend on sample details, such as the number of nanowires or their configuration, which we believe plays a role in our case. Therefore, we attribute this higher value to a collective PZR effect brought about by the interaction between multiple and interconnected wires rather than the response of a single nanowire. Additionally, the pressure sensitivity of the sensor in the isostatic pressure variation given by $S = \frac{\Delta R}{R}/\Delta P$ [39], in the pressure range of 10^{-4} to 10^3 mbar, is 9.98×10^{-6} Pa^{-1}. It is also seen that the highest sensitivity (highest slope in Figure 8) is found in the pressure range of roughly 10^{-2} and 10^{-1} mbar where the sensitivity measure is 8.8×10^{-3} Pa^{-1}.

5. Conclusions

In summary, large arrays of interconnected SiNWs were fabricated in a simple three-step wet chemical process and used for testing the piezoresistance effect in nanowires. The interconnected structures of the SiNWs provide a great increase in mechanical stability. A pressure change of 100 Pa could be measured with this robust device. The calculated PZR coefficient based on SiNWs array with NWs length of 3 µm as resulted after MACE etching for 7 min, sample D, was almost two orders of magnitude higher for our sensor than reported for a single SiNW. Repeated measurements for different samples fabricated with the same process demonstrated good reproducibility with less than 5% deviation in pressure sensing. The electrical resistance of SiNWs of 10 µm length increased more than two orders of magnitude when measured in a vacuum. These findings make the device based on random and interconnected SiNWs a strong candidate as a simple and inexpensive alternative to various pressure-sensing applications.

Author Contributions: Conceptualization, R.P.; Funding acquisition, H.G.S.; Investigation, E.F., M.T.S., T.H.K. and H.Ö.Á.; Methodology, E.F., M.T.S. and H.G.S.; Project administration, R.P., N.P., A.M. and H.G.S.; Supervision, R.P., N.P., A.M., S.I. and H.G.S.; Visualization, H.G.S.; Writing—original draft, E.F.; Writing—review & editing, M.T.S., A.M., S.I. and H.G.S. All authors have read and agreed to the published version of the manuscript.

Institutional Review Board Statement: Not applicable.

Informed Consent Statement: Not applicable.

Data Availability Statement: Not applicable.

Conflicts of Interest: The authors declare no conflict of interest.

References

1. Peng, K.Q.; Wang, X.; Li, L.; Hu, Y.; Lee, S.T. Silicon nanowires for advanced energy conversion and storage. *Nano Today* **2013**, *8*, 75–97. [CrossRef]
2. Heris, H.R.; Kateb, M.; Erlingsson, S.I.; Manolescu, A. Thermoelectric properties of tubular nanowires in the presence of a transverse magnetic field. *Nanotechnology* **2020**, *31*, 424006. [CrossRef] [PubMed]
3. Heris, H.R.; Kateb, M.; Erlingsson, S.I.; Manolescu, A. Effects of transverse geometry on the thermal conductivity of Si and Ge nanowires. *Surf. Interfaces* **2022**, *30*, 101834. [CrossRef]
4. Zhou, X.; Hu, J.; Li, C.; Ma, D.; Lee, C.; Lee, S. Silicon nanowires as chemical sensors. *Chem. Phys. Lett.* **2003**, *369*, 220–224. [CrossRef]
5. Peng, K.Q.; Wang, X.; Lee, S.T. Gas sensing properties of single crystalline porous silicon nanowires. *Appl. Phys. Lett.* **2009**, *95*, 243112. [CrossRef]
6. Smith, C.S. Piezoresistance effect in germanium and silicon. *Phys. Rev.* **1954**, *94*, 42–49. [CrossRef]
7. Tufte, O.N.; Chapman, P.D.; Long, D. Silicon diffused-element piezoresistive diaphragms. *J. Appl. Phys.* **1962**, *33*, 3322–3327. [CrossRef]
8. Tortonese, M.; Barrett, R.C.; Quate, C.F. Atomic resolution with an atomic force microscope using piezoresistive detection. *Appl. Phys. Lett.* **1993**, *62*, 834. [CrossRef]
9. Ning, Y.; Loke, Y.; McKinnon, G. Fabrication and characterization of high g-force, silicon piezoresistive accelerometers. *Sens. Actuators A Phys.* **1995**, *48*, 55–61. [CrossRef]
10. Wee, K.; Kang, G.; Park, J.; Kang, J.; Yoon, D.; Park, J.; Kim, T. Novel electrical detection of label-free disease marker proteins using piezoresistive self-sensing micro-cantilevers. *Biosens. Bioelectron.* **2005**, *20*, 1932–1938. [CrossRef]
11. Tiwari, B.; Billot, M.; Clévy, C.; Agnus, J.; Piat, E.; Lutz, P. A two-axis piezoresistive force sensing tool for microgripping. *Sensors* **2021**, *21*, 6059. [CrossRef] [PubMed]
12. Dorda, G. Piezoresistance in quantized conduction bands in silicon inversion layers. *J. Appl. Phys.* **1971**, *42*, 2053–2060. [CrossRef]
13. He, R.; Yang, P. Giant piezoresistance effect in silicon nanowires. *Nat. Nanotechnol.* **2006**, *1*, 42–46. [CrossRef] [PubMed]
14. Gao, D.; Yang, Z.; Zheng, L.; Kun, Z. Piezoresistive effect of n-type <111> -oriented Si nanowires under large tension/compression. *Nanotechnology* **2017**, *28*, 095702. [PubMed]
15. Zhang, S.; Lou, L.; Lee, C. Piezoresistive silicon nanowire based nanoelectromechanical system cantilever air flow sensor. *Appl. Phys. Lett.* **2012**, *100*, 023111. [CrossRef]
16. Cheng, W.; Yu, L.; Kong, D.; Yu, Z.; Wang, H.; Ma, Z.; Wang, Y.; Wang, J.; Pan, L.; Shi, Y. Fast-response and low-hysteresis flexible pressure sensor based on silicon nanowires. *IEEE Electron Device Lett.* **2018**, *39*, 1069–1072. [CrossRef]
17. Nguyen, T.D.; Lee, J.S. Recent Development of Flexible Tactile Sensors and Their Applications. *Sensors* **2021**, *22*, 50. [CrossRef]
18. Kim, C.; Ahn, H.; Ji, T. Flexible Pressure Sensors Based on Silicon Nanowire Array Built by Metal-Assisted Chemical Etching. *IEEE Electron Device Lett.* **2020**, *41*, 1233–1236. [CrossRef]
19. Ghosh, R.; Song, M.S.; Park, J.; Tchoe, Y.; Guha, P.; Lee, W.; Lim, Y.; Kim, B.; Kim, S.W.; Kim, M.; et al. Fabrication of piezoresistive Si nanorod-based pressure sensor arrays: A promising candidate for portable breath monitoring devices. *Nano Energy* **2021**, *80*, 105537. [CrossRef]

20. Shiri, D.; Kong, Y.; Buin, A.; Anantram, M.P. Strain induced change of bandgap and effective mass in silicon nanowires. *Appl. Phys. Lett.* **2008**, *93*, 07314. [CrossRef]
21. Zhang, J.; Zhao, Y.; Ge, Y.; Li, M.; Yang, L.; Mao, X. Design optimization and fabrication of high-sensitivity SOI pressure sensors with high signal-to-noise ratios based on silicon nanowire piezoresistors. *Micromachines* **2016**, *7*, 187. [CrossRef] [PubMed]
22. Rowe, A. Piezoresistance in silicon and its nanostructures. *J. Mater. Res.* **2014**, *29*, 731–744. [CrossRef]
23. Toriyama, T.; Tanimoto, Y.; Sugiyama, S. Single crystal silicon nano-wire piezoresistors for mechanical sensors. *J. Microelectromechanical Syst.* **2002**, *11*, 605–611. [CrossRef]
24. Toriyama, T.; Sugiyama, S. Single crystal silicon piezoresistive nano-wire bridge. *Sens. Actuators A Phys.* **2003**, *108*, 244–249. [CrossRef]
25. Schmidt, V.; Wittemann, J.V.; Senz, S.; Gösele, U. Silicon nanowires: A review on aspects of their growth and their electrical properties. *Adv. Mater.* **2009**, *21*, 2681–2702. [CrossRef]
26. Shi, D.; Chen, Y.; Li, Z.; Dong, S.; Li, L.; Hou, M.; Liu, H.; Zhao, S.; Chen, X.; Wong, C.P.; et al. Anisotropic Charge Transport Enabling High-Throughput and High-Aspect-Ratio Wet Etching of Silicon Carbide. *Small Methods* **2022**, 6, 2200329. [CrossRef]
27. Svavarsson H.G.; Hallgrimsson, B.H.; Niraula, M.; Lee K.J.; Magnusson, R. Large arrays of ultra-high aspect ratio periodic silicon nanowires obtained via top-down route. *Appl. Phys. A-Mater. Sci. Process.* **2016**, *122*, 1–6. [CrossRef]
28. Fakhri, E.; Sultan, M.; Manolescu, A.; Ingvarsson, S.; Plugaru, N.; Plugaru, R.; Svavarsson, H. Synthesis and photoluminescence study of silicon nanowires obtained by metal assisted chemical etching. In Proceedings of the 2021 International Semiconductor Conference (CAS), Sinaia, Romania, 6–8 October 2021; pp. 147–150.
29. Plugaru, R.; Fakhri, E.; Romanitan, C.; Mihalache, I.; Craciun, G.; Plugaru, N.; Árnason, H.O.; Sultan, M.T.; Nemnes, G.A.; Ingvarsson, S.; et al. Structure and electrical behavior of silicon nanowires prepared by MACE process. *arXiv* **2022**, arXiv:2206.05006
30. Neuzil, P.; Wong, C.C.; Reboud, J. Electrically controlled giant piezoresistance in silicon nanowires. *Nano Lett.* **2010**, *10*, 1248–1252. [CrossRef]
31. Danielsson, D.; Gudmundsson, J.; Svavarsson, H. Effect of hydrogenation on minority carrier lifetime in low-grade silicon. *Phys. Scr.* **2010**, *2010*, 014005. [CrossRef]
32. Svavarsson, H.G.; Sultan, M.T.; Lee, K.J.; Magnusson, R. Hydrogenated silicon films for low-loss resonant reflectors operating in the visible region. In Proceedings of the 2020 IEEE Research and Applications of Photonics, Miramar Beach, FL, USA, 10–12 August 2020; pp. 1–2.
33. Sultan, M.; Gudmundsson, J.T.; Manolescu, A.; Stoica, T.; Ciurea, M.; Svavarsson, H. Enhanced photoconductivity of embedded SiGe nanoparticles by hydrogenation. *Appl. Surf. Sci.* **2019**, *479*, 403–409. [CrossRef]
34. Sultan, M.; Gudmundsson, J.T.; Manolescu, A.; Ciurea, M.; Svavarsson, H. The Effect of H 2/Ar Plasma Treatment Over Photoconductivity of Sige Nanoparticles Sandwiched Between Silicon Oxide Matrix. In Proceedings of the 2018 International Semiconductor Conference (CAS), Sinaia, Romania, 10–12 October 2018; pp. 257–260.
35. Song, L.; Yang, D.; Yu, X. Investigation on the impact of hydrogen on the passivation of silicon surface states in clean and copper contaminated conditions. *AIP Adv.* **2019**, *9*, 105102. [CrossRef]
36. Niquet, Y.M.; Delerue, C.; Krzeminski, C. Effects of strain on the carrier mobility in silicon nanowires. *Nano Lett.* **2012**, *12*, 3545–3550. [CrossRef]
37. Matsuda, K.; Suzuki, K.; Yamamura, K.; Kanda, Y. Nonlinear piezoresistance effects in silicon. *J. Appl. Phys.* **1993**, *73*, 1838–1847. [CrossRef]
38. Doll, J.C.; Pruitt, B.L. *Piezoresistor Design and Applications*; Springer: Berlin, Germany, 2013.
39. Pataniya, P.M.; Bhakhar, S.A.; Tannarana, M.; Zankat, C.; Patel, V.; Solanki, G.; Patel, K.; Jha, P.K.; Late, D.J.; Sumesh, C. Highly sensitive and flexible pressure sensor based on two-dimensional MoSe2 nanosheets for online wrist pulse monitoring. *J. Colloid Interface Sci.* **2021**, *584*, 495–504. [CrossRef] [PubMed]

Paper V
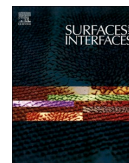
Structure and electrical behavior of silicon nanowires prepared by MACE process

R. Plugaru [1,a], E. Fakhri [*,1,b], C. Romanitan [a], I. Mihalache [a], G. Craciun [a], N. Plugaru [a], H.Ö. Árnason [b], M.T. Sultan [c], G.A. Nemnes [d,e], S. Ingvarsson [c], H.G. Svavarsson [b], A. Manolescu [b]

[a] National Institute for Research and Development in Microtechnologies- IMT Bucharest, Voluntari 077190, Romania
[b] Department of Engineering, Reykjavik University, Menntavegur 1, Reykjavik IS-102, Iceland
[c] Science Institute, University of Iceland, Dunhaga 3, Reykjavik IS-107, Iceland
[d] Horia Hulubei National Institute for Physics and Nuclear Engineering, Magurele-Ilfov 077126, Romania
[e] University of Bucharest, Department of Physics, Magurele-Ilfov 077125, Romania

ARTICLE INFO

ABSTRACT

We report on the structure and electrical characteristics of silicon nanowire arrays prepared by metal assisted chemical etching (MACE) method, investigated by cross-sectional scanning electron microscopy (SEM) and high resolution X-ray diffraction (HR-XRD) methods. SEM micrographs show arrays of merged parallel nanowires, with lengths of 700 nm and 1000 nm, resulted after 1.5 min and 5 min etching time, respectively. X-ray reciprocal space maps (RSMs) around Si (004) reciprocal lattice point indicate the presence of 0D structural defects rather than of extended defects. The photoluminescence spectra exhibit emission bands at 1.70 eV and 1.61 eV, with intensity significantly higher in the case of longer wires and associated with the more defected surface. The transient photoluminescence spectroscopy reveals average lifetime of 60 ôs and 111 ôs for the two SiNW arrays, which correlate with a larger density of defects states in the latest case. The I-V characteristics of the nanowires, show a memristive behavior with the applied voltage sweep rate in the range 5–0.32V/s. We attribute this behavior to trap states which control the carrier concentration, and model this effect using an equivalent circuit. Photogeneration processes under excitation wavelengths in visible domain, 405 nm - 650 nm, and under light intensity in the range 20–100 mW/cm^2 provided a further insight into the trap states.

1. Introduction

Silicon nanowire (SiNW) arrays with controlled morphology (porosity, length, orientation) have been efficiently prepared by metal assisted chemical etching (MACE) processing [1–3], aiming to widen their applicability to performant light emitting devices, photodetectors, energy storage and conversion, or sensors [4–6]. Yet, defective surfaces of SiNWs resulting from chemical-assisted preparation processes can affect the electric parameters of the devices [7,8].

The dynamic hysteresis of the electrical characteristics of a nano-electronic device when the applied voltage changes in time is one of the first indications of the presence of a charge trapping mechanism inside the devices with a relaxation time comparable to the time of the voltage variation. This phenomenon is used in memristive device, often based on metallic nanowires [9], but also on silicon nanowires [10,11].

Sensing devices based on SiNWs have also been proposed, where the dynamic occupation of the nanowire surface states created by the external charges from the adsorbed biomolecules modify the hysteresis loop [12]. Or field effect transistors where the nanowires are in contact with a dielectric, or polymer [13].

The electrical hysteresis is also present in solar cells based on perovskite materials, and associated to the degradation of the cell, due to ionic migration, charge accumulation at interfaces, and their influence on the photogenerated current [14–16]. Apart of the possible hysteretic effects, the surface states of SiNWs are also important for the characteristics of nanostructured solar cells, where the electrons trapped by surface states can act as a gate bias that enhances the photoconductivity [17–19].

In this work we report on the electrical response of Al/SiNWs/Al device structures with pristine SiNW arrays prepared by the MACE

* Corresponding author.
E-mail addresses: rodica.plugaru@imt.ro (R. Plugaru), elhamf20@ru.is (E. Fakhri).
[1] These authors contributed equally to this work.

method. The nanowires are highly imperfect and in lateral contact to each other, forming a system of inter-connected wires rather than independent wires. The current-voltage (I-V) and capacitance-voltage (C-V) curves, measured in dark and under various illumination conditions in terms of wavelengths and intensity, are analyzed using an equivalent circuit with lump elements. The model, although simplistic, is able to reproduce satisfactorily the normal and inverted hysteresis observed in the I-V curves. We suggest that the intimate mechanism accounting for the hysteresis may be related to the effect of charge carrier trapping and detrapping at the surface states present in the pristine SiNW arrays. We show that traps filling by tuning the light wavelength may be used as a method to determine their origin and electronic properties.

2. Experimental

Inter-connected silicon nanowire arrays have been fabricated via metal-assisted chemical etching (MACE) as shown in the flow chart presented in Fig. 1 Single-sided polished samples (1×1 cm^2) cut from (100) oriented silicon wafers (p-type, with resistivity of $1 - 10$ $\Omega \cdot$cm and thickness of 625 ôm) were used in the process. The samples were cleaned with acetone, methanol, isopropanol, and deionized water followed by drying in N_2 gas flow, then treated with HF:H_2O (1:3) solution for 3 min to remove the native oxide. To obtain the SiNW arrays, the polished side of the samples were coated with Ag nanoparticles by immersing them in HF [3 M]:AgNO$_3$ [1.5 mM] solution for 1 min. The coated samples were then cleaned with DI-water to remove the excess of Ag nanoparticles. The samples subsequently underwent etching process by immersing them in an etching solution of HF [5 M]:H_2O_2[0.4 M] for 1.5 min and 5 min, respectively, followed by immersion in H_2O:HNO$_3$ (3:1) to remove residual Ag nanoparticles. Finally, the samples were cleaned with DI-water, then dried with N_2 gas. For electrical measurements, two coplanar Al contacts, 2×10 mm^2 each, with the thickness of 150 nm were deposited on the surface of the samples via a hard mask. The distance between the two contacts is 6 mm. Contacts deposition was made by using an electron beam evaporator (Polyteknik Cryofox Explorer 600 LT).

Micrographs of the SiNWs were recorded on the top and at a tilt angle to observe the in-depths of the structures, by using a field emission scanning electron microscope (FE-SEM), FEI NovaTM NanoSEM 630. The structural characteristics of the SiNW arrays were investigated by using a SmartLab X-ray diffraction system from Rigaku Corp. (Osaka, Japan). X-ray reciprocal space maps (RSMs) around Si (004) reciprocal lattice point were recorded in triple-axis configuration (ultra-high resolution) with a four-bounce Ge monochromator with two reflections at incidence and a two-bounce Ge monochromator with two reflections in the front of detector. Bending profiles were obtained using grazing-incidence XRD in asymmetric skew geometry in (111) reflection. In this configuration, the incidence angle of the source was varied from 0.5° to 4° to obtain different X-ray penetration depth.

The photoluminescence (PL) emission spectra of the SiNW arrays were recorded with an Edinburgh FL920 fluorescence spectrophotometer equipped with microsecond flashlamp as an excitation source. Time-correlated single photon counting (TCSPC) technique was used to
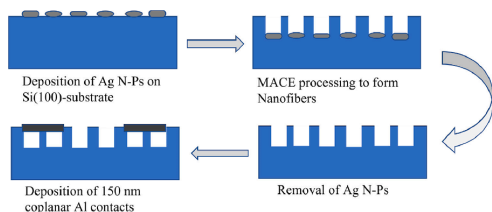
determine the photoluminescence lifetime, using excitation at 300 nm and recording the emission at 770 nm wavelength. FAST Version 3.4.2. Edinburgh Instruments Ltd software was used for experimental fit.

The I-V and C-V characteristics were measured using a Keithley 2400 and SCS 4200 Keithley system, in dark and under light illumination with various wavelengths, as well as under white light using a solar simulation lamp, with intensities in the range 20–100 mW/cm^2. The curves were recorded by forward and reverse sweeping the applied voltage in the range -10V to +10V.

3. Results

3.1. Structure and PL properties of silicon nanowires

The top and cross-sectional SEM micrographs of the SiNW arrays obtained at 1.5 min and 5 min etching time, are shown in Fig. 2a–d. The length of the NWs is about 700 nm after 1.5 min etching (see Fig. 2a-b) and 1000 nm after 5 min etching (Fig. 2 c-d). In the following we refer to these two samples as SiNW$_{short}$ and SiNW$_{long}$, respectively. There is a saturation value so that the lengths of the wires are limited with the respect of the concentrations of the oxidizing agent H_2O_2, AgNO$_3$ concentration, and specific resistivity (ρ) of bulk Si [20]. As seen, the wires are laterally interconnected and form continuous structures of walls in both arrays. According to ImageJ analysis, the coverage area is 36% and 32% for SiNW$_{short}$ and SiNW$_{long}$, respectively, which suggests that the longer etching time leads to a higher porosity. Note that the coverage area means the surface occupied by tips of SiNWs observed in SEM top view image and by longer etching time the diameter of SiNWs decreases and as result the coverage area decreases. In order to investigate the microstructural features of the nanowire arrays, we performed X-ray diffraction in high resolution setup. X-ray reciprocal space maps (RSMs) around Si (004) reciprocal lattice point give information regarding the out-of-plane lattice value, relative lattice strain and the crystal imperfections. X-ray RSMs along (q_z, q_x) coordinates for SiNW$_{short}$ and SiNW$_{long}$ arrays are presented in Fig. 3a and b. The reciprocal space coordinates q_x and q_z are projections of the scattering vector along [100] and [001] directions, respectively, and are related with the angular coordinates as: $q_x = [2\sin(\omega - \theta)]/\lambda$ and $q_z = (2\sin\theta)/\lambda$.

The X-ray reciprocal space maps present an intense peak located around $q_z \in (0.7360 - 0.7365)$ Å^{-1}. Using the crystallographic relations for cubic crystals, the lattice constant a can be expressed as $\frac{4}{q_z}$ [21], giving a lattice constant equal to 5.43 Å, which corresponds to the lattice

Fig. 1. Schematic illustration of the MACE steps for SiNWs preparation and Al/SiNWs/Al structures fabrication.
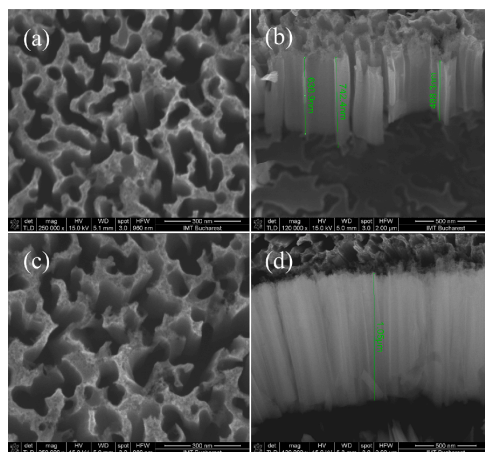

Fig. 2. SEM micrographs of the SiNWs arrays prepared by a MACE process. The etching time was: (a), (b) 1.5 min and (c), (d) 5 min.
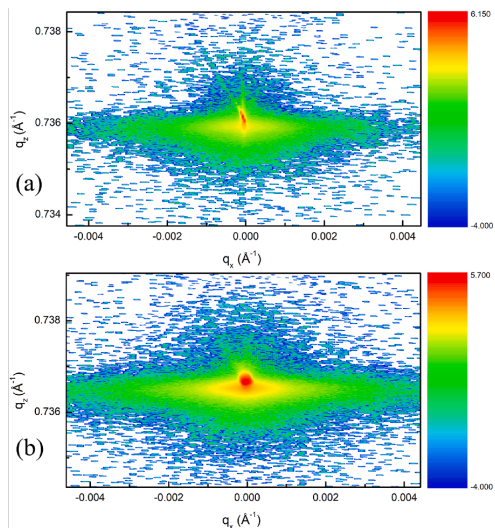
Fig. 3. X-ray reciprocal space maps (RSMs) recorded near Si (004) reciprocal lattice point on the nanowire arrays with length of (a) 700 nm and (b) 1000 nm SiNWs.

parameter of bulk Si. This is an indication that the MACE process does not affect the value of the lattice parameter of the samples. Further, it can be observed that the spot broadening increases with increasing the nanowire length in both q_z and q_x direction. The broadening of the RSM spot can be ascribed to the occurrence of bending and torsion of nanowire array, which is more pronounced for the longer (1000 nm) SiNWs, due to a higher surface energy. At the same time, the X-ray scattering in the reciprocal space looks different. For instance, the area elongated along q_x, which is related to the diffuse scattering, could be determined by crystal imperfections (e.g. point defects, extended defects, or stacking faults), and broader angular dispersion is observed for the longer nanowires. The cross section of intensity distribution of our RSM along q_x is presented below in Fig. 4a.

The X-ray rocking curves indicate two types of scattering: (1) the narrow peak is related to the specular scattering (I_{spec}), also called Bragg scattering, where the X-ray scattering has taken place on the atomic planes; (2) the broad feature indicates the presence of the X-ray diffuse scattering (XDRS), further denoted as I_{diff}. This scattering is determined by the structural imperfections in the Si lattice. To have a qualitative description of the X-ray scattering, we obtain the ratio between I_{diff} /($I_{diff} + I_{spec}$). For instance, the shorter SiNWs exhibits a ratio of 0.31, whereas the longer SiNWs exhibits ratio of 0.94. Clearly, this ratio can

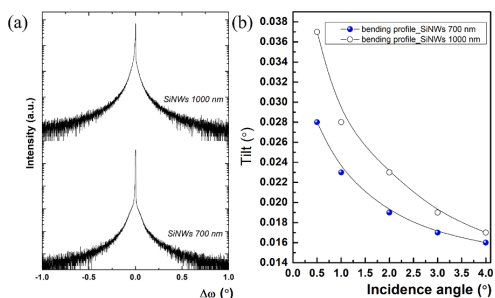be viewed as a measure of the structural defect density in our samples. It is reasonable to assume that the longer SiNWs possesses a higher density of the structural defects, being promoted by the strain relaxation processes due to the bending and torsion phenomena [22].

To prove the existence or absence of the strain relaxation processes, we obtained bending profiles of our samples, which correspond to the average tilt of the arrays - Fig. 4 b. These profiles were obtained in the framework of grazing-incidence X-ray diffraction on highly-asymmetric (111) reflection, which allowed us to attain different X-ray penetration depths, varying the incidence angles of the X-ray source. Further details regarding the grazing-incidence X-ray diffraction technique on (111) in nanowires, as well as for the bending profiles can be found in [23].

The evolution of the FWHM of the X-ray spectra with the incidence angle gives the tilt of nanowire array at different penetration depths. One may observe that the shorter nanowires determine a smaller tilt, e.g. 0.028°, comparing to the longer ones which have an average tilt of 0.037°. It is clear that the higher tilt for the longer nanowires is determined by a higher surface energy of the nanowire array. However, for both samples the bending profiles do not present dips, whose occurrence can be assigned to a quasi-local manifestation of some relaxation mechanisms in the nanowires. The absence of the strain relaxation processes can be further attributed to the absence of the extended structural defects, such as edge and screw threading dislocations. This is possible by taking into account the small length of our arrays. Also, previous investigations in highly dense nanowire arrays prepared by MACE showed the occurrence of edge and screw threading dislocations only for wires longer than 9 μ m [23]. At the same time, we must consider the previous findings from the rocking curves profiles, indicating a relationship between the array length and the XRDS intensity, which was attributed to the presence of the structural defects.

The XRD findings indicate that the MACE process has determined the formation of 0D defects, nanocrystals or nanopores on the surface of SiNWs, rather than extended structural defects. The nature of structural defects is analyzed by the photoluminescence (PL) emission from SiNWs arrays. The PL spectra are shown in Fig. 5.

The SiNW$_{short}$ presents a rather weak PL intensity, about 1/15 of the PL for the SiNW$_{long}$. The spectrum is centered at 730 nm (1.70 eV). Sample SiNW$_{long}$ shows an intense and broad PL emission spectra in the VIS-NIR region, centered at 770 nm (1.61 eV). The red-shift in energy of 80 meV of the PL maximum position, observed for the longer NWs, could be related to the structure of interconnected skeletons and increased porosity, as resulted during the MACE process with a longer duration [20]. The observed red-shift with longer etching time is in agreement with our previous results [20]. It has however worth noting that others researchers [24], have observed blue-shift upon increasing etching time

Fig. 4. Cross section of intensity distribution along q$_x$ direction for short and long nanowire arrays (a) and (b) bending profiles.
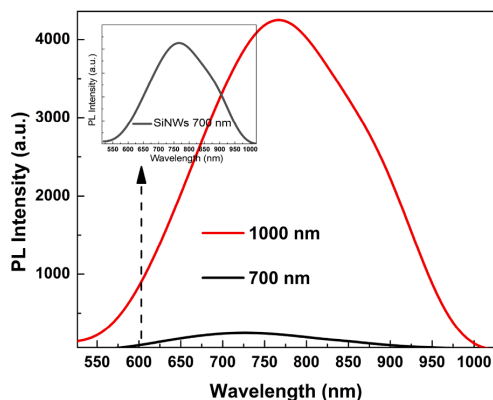

Fig. 5. PL spectra of SiNWs arrays under excitation with Xe lamp at wavelength of 350 nm and 450 W power.

and correlated that with the presence of SiO_x. It appears that in our case, the SiO_x fraction is not increasing with the etching time and consequently has a low contribution to the PL emission which strongly shifts towards NIR spectral range. A slow (S) band in the red-yellow spectral range with long microsecond decay times is reported and analyzed in porous silicon nanostructures PL spectra and attributed to phonon-assisted exciton recombination within the silicon nanostructure [25]. It was also reported that TEM images of the luminescent SiNWs prepared by MACE technique reveal that the surfaces of the SiNWs are very rough, with a few nano-sized silicon particles being attached to the SiNWs. The PL spectrum of such SiNWs was peaked at 700 nm for an excitation wavelength of 400 nm [26].

Lin et al. [27] reported that SiNWs synthesized via MACE exhibit a nanoporous structure. The PL emission band in the red region, at 730 nm was attributed to the excitons captured by the interface states between the Si nanostructures and the native oxide layer. The PL intensity increases with the porosity [27]. It was also reported that longer etching time, or higher H_2O_2 concentration could facilitate the diffusion and nucleation of Ag ions and effectively enhance the porosity of the nanowires [28]. Recently, it was shown that MACE-produced SiNW arrays are covered with porous structures, silicon nanocrystals, which result from the lateral etching of NWs sidewalls. The broad PL spectrum centered at 695 nm (1.78 eV) is attributed to radiative recombination of excitons in these nanocrystals [29]. In our experiment, even if the length of the NWs does not differ very much, the PL intensity is substantially higher in the case of long wires which suggests the formation of a larger number of luminescence centers.

The enhancement of the PL intensity and the wavelength red-shift could be attributed to enhanced porous structure of the SiNWs surface and also of a porous Si layer formed at the base of SiNWs, resulting after a longer MACE process [30,31]. Previous studies reported that HF post etching treatments of SiNWs are mandatory in order to obtain light emission [32]. Other experiments demonstrated that H_2O_2 could favor PL emission, which is attributed to SiO_2 layer formation on the NWs surface [24]. However, in this work a different etching process in terms of reagents concentration leads to a significant intensity of the PL emission, without any post-treatment, as also observed by reference [33]. This result underlines the essential role of the etching solution concentration on the formation of various light emitting centers, such as Si nanostructures, SiO_2 layer, other specific Si bonding structure. The PL lifetime of the SiNWs arrays, was measured by transient photoluminescence spectroscopy (TCSPC) method.

Fig. 6 shows PL emission decay curves of the SiNWs arrays obtained by using the excitation wavelength 300 nm and the emission wavelength 770 nm. The monoexponential lifetime decreases sharply for shorter

Fig. 6. PL emission decay curves of the SiNWs arrays, with average lifetime 111 μ s (1000 nm length) and 60 μ s (700 nm length), respectively.

SiNWs, indicating a smaller contribution of the surface disorder. Long lifetime observed for the longer SiNWs should be mostly dictated by nonradiative processes involving surface defects, in agreement with the results of XRD-RSM maps presented in Fig. 3. The average lifetime obtained by fitting the experimental values is 60 ôs for the short SiNWs and 111 ôs for long SiNWs. By increasing the etching time, the number of both radiative and non-radiative centers increases, however their ratio remains relatively unchanged and that determines longer luminescence lifetime coupled with stronger radiative emission.

3.2. Electrical characteristics of silicon nanowires

The I-V curves of the Al/SiNWs/Al structures, measured at various voltage sweep rates in dark and under illumination, are presented in Fig. 7 a–j. The plots are non-linear, characteristic to two diodes in antiparallel configuration, due to the Al-Si Schottky contacts. The current intensities under illumination are slightly higher compared to those measured in dark. The hysteresis observed in the I-V curves of both samples suggests that a process of trapping and de-trapping of minority (e) charge carriers, with different time constants, may take place. A dependence of the hysteresis area (in VA units) as a function of the voltage sweep rate may also be observed, see Fig. 8a and b.

In the case of the SiNW$_{short}$ sample the hysteresis area in quadrant 1, defined as area of the "down" curve minus the area of the "up" curve, shows a continuous decrease as the voltage sweep-rate increases, see Fig. 8a, but remains in the positive range of values. A different behavior may be observed in the case of SiNW$_{long}$, as the hysteresis area takes negative values at small V rates and positive values for rates beyond 1.38 V/s, see Fig. 8b. Also, the data reveal that the hysteresis area increases under illumination for short NWs, see Fig. 8a, but exhibits an interesting evolution at sweep rates below 4 V/s in the case of long NWs, Fig. 8b. Additional results obtained on SiNW arrays with lengths larger than 1000 nm and exhibiting different morphologies are shown in the Supplementary Material, Fig. S2. where it has been observed that posttreated SiNWs with HF shows minimum hysteresis and confirm that surface defect-free nanowires can be prepared by MACE using an HF post-treatment. This result is in good agreement with Choi et al [34]. It is worth noting that the untreated bulk Si shows no hysteresis and confirms the larger defective surface area of SiNWs is associated with charge trapping and hysteresis effect. The corresponding plot is shown in Supplementary Material, Fig. S3. As apparent, the extend of the hysteresis is not related with etching time in the range tested (2–10 min).

4. Modeling the I-V characteristics

We consider an equivalent electrical circuit of the Si/SiNWs/Al structures to model the observed memristive behavior of measured I-V curves. The memristive effect consists in the dependence of the I-V curve, and consequently of the electrical resistance of the device, on the history of the applied voltage, i. e. increasing or decreasing [9]. I-V hysteresis loops for multiple cycles are shown in the Supplementary Material, Fig. S1. The I-V experimental data show exponential-like dependencies, and a difference between the current ædupg, I_{up}, i.e. when the voltage increases, and the current ædowng I_{down}, i.e. when the voltage decreases. A simple model to account for this behavior should combine a resistor, two diodes, and one or two capacitors, as illustrated in Fig. 9. The role of the diodes is to give the exponential-like current as a function of voltage, and the role of the $R - C$ block is to generate a voltage drop u which controls the number of charge carriers passing through the circuit. The voltage u corresponds to an electric field internal to the diodes, such that the currents through each diode D_j, $(j = 1, 2)$ can be written as:

$$I_{D_j}(t) = I_j \left[e^{\frac{q[V(t) - u(t)]}{\eta_j kT}} - e^{\frac{-qu(t)}{\eta_j kT}} \right] \tag{1}$$
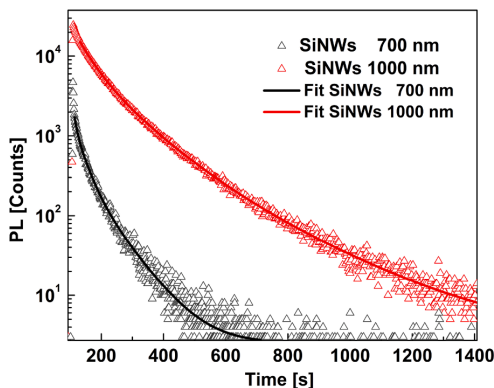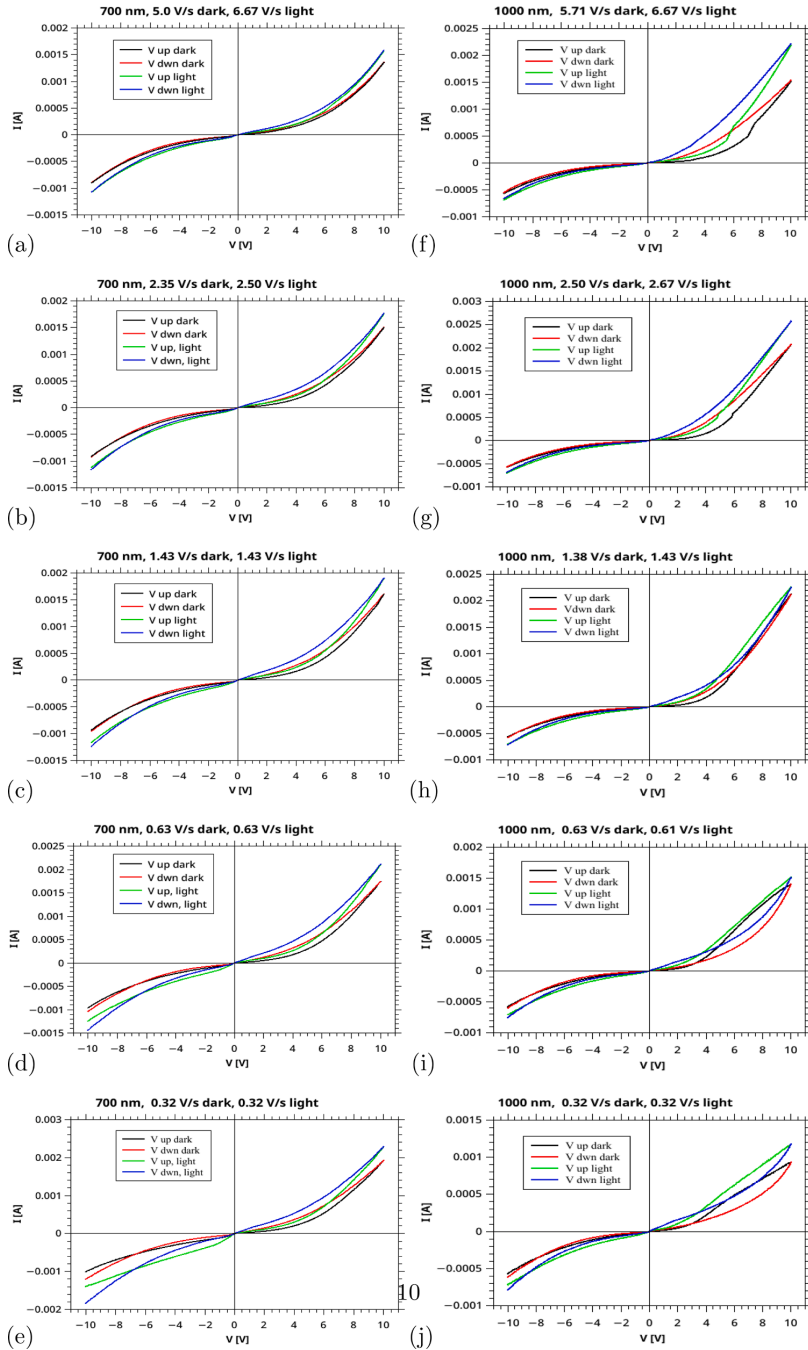
Fig. 7. Current-voltage characteristics of Al/SiNWs/Al structures: (a)-(e) short SiNWs and (f)-(j) long SiNWs, measured at various voltage sweep rates. In dark and under illumination measurements.

where I_j and n_j are diode parameters (saturation current and ideality factor, respectively), q is the elementary electric charge, k is Boltzmanns constant, and T the temperature. We begin by considering only one capacitor, C_1, and ignore the second one, i.e. $C_2 = 0$. The total current in

the circuit is then:

$$I = I_{D_1} + I_{D_2} = I_R + I_{C_1},$$ (2)

where $I_R = u/R$, and I_{C_1} is discussed below.

5

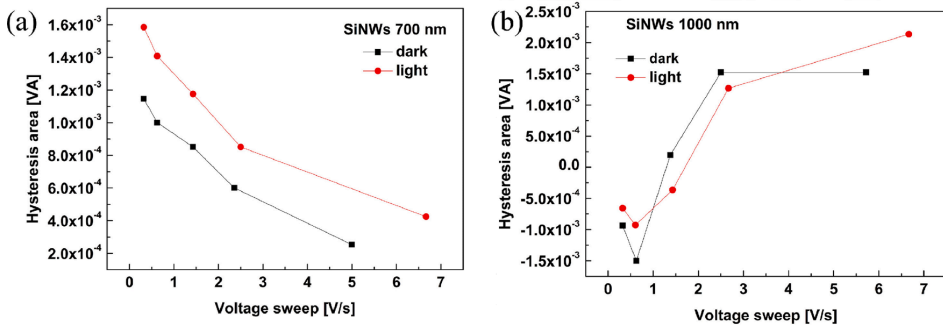**Fig. 8.** Hysteresis area vs voltage sweep rate for the device: (a) short SNWs and (b) long SiNWs.

The order of magnitude of the charge associated with the capacitance C_1 needed to explain the experimental data can be inferred from the observed hysteresis effect. The total charge going through the circuit corresponds to the area of the current versus time, which can easily be evaluated since the voltage has a constant rate in time. For example, for the SiNW$_{short}$ sample, at a voltage rate of 0.63 V/s in dark (Fig. 7d), the hysteresis area between the positive voltages 4 V and 5 V, corresponding to a time interval of 1.6 s, is 0.15 mVA, or 0.24 mAs or 0.24 mC of electric charge. This gives an estimated $C_1 \approx 0.24$ mF, which is obviously a very large value for such a small sample. A more realistic assumption is to assume a much smaller capacitance, and associate the capacitor with a trapping mechanism, which temporarily stores a relatively small amount of charge, Q_1, but contributes significantly to the voltage u, which in turn has a much larger effect on the current than the stored charge. The capacitance is associated to a temporary polarization effect, likely due to interface states in the Schottky diodes [35] and/or surface states [11,12]. Therefore, we assume that the current controlled by the capacitor is

$$I_{C_1} = b \frac{dQ_1}{dt} \qquad (3)$$

where b is a coefficient describing the amplification factor of the number of carriers controlled by the polarization effects associated with the charge Q_1. Here Eq. (3) is a simplified version of Equation (5) of Reference [12], where both acceptor-like and donor-like traps are considered.

Next, we denote by τ_1 the time constant associated to the relaxation of this electric or trapping charge. This relaxation process may depend on more complex phenomena, like ion displacement, diffusion, etc., which we cannot describe in detail. Instead, we define the relaxation time τ_1 via the equation

$$\frac{dQ_1}{dt} = -\frac{Q_1(t) - C_1 u(t)}{\tau_1} \qquad (4)$$

which leads to an exponentially asymptotic charging or discharging with a time factor e^{-t/τ_1}. A similar assumption has been used to explain the hysteresis phenomenon in perovskite based solar cells [36].

In Fig. 10 we show the calculated I-V characteristic using empirical parameters inspired by the experimental results, but also adjusted for the convenience of the numerical calculations: $I_1 = 0.04$ mA, $I_2 = 0.03$ mA, $n_1 = -n_2 = 30$, $\tau_1 = 6$ s, $C_1 = 1.5$ nF, $b = 10^6$, $R = 1600$ Ω. The voltage is swept from -5 V to 5 V and back to -5 V in 50 seconds, i.e. with a rate of 0.4 V/s. The current was calculated numerically using Eqs. (1)–(4), by discretizing the time in small steps, with initial conditions $Q_1 = 0$. (The current in the two diodes was obtained using the Lambert function, since the voltage $u(t)$ implicitly depends on the current.)

The intersection of the "up" and "down" curves at negative voltages occurs because of the initial and final state of the capacitor (uncharged vs. charged). However, one feature of the hysteresis loop shown in Fig. 10 differs from the experiment. For positive voltage, the "up" curve is always above the down curve, i.e. opposite to the experimental data obtained for the sample A (700 nm). The reason is that after the voltage reached the maximum and begins to decrease, the capacitor C_1 pushes current against the main current of the source, i.e. decreasing the current compared to the "up" values. This effect does not depend on the magnitude of the coefficient b, but on its sign, which is positive. To match the experimental data with this simple model we need to assume a *negative* sign of this coefficient b for the "up" segment of the I-V characteristic, i.e. in that phase the trapping mechanism releases current with the same orientation as of the total current. The resulting I-V curves are shown in Fig. 11.

The I-V characteristic looks now qualitatively similar to the experimental data shown in Fig. 7a–e. This similarity suggests a negative intrinsic polarization mechanism of the sample, during the measurements, with a relaxation time of the order of seconds. Such a situation can also be obtained in perovskite based solar cells, where the "up" and "down" currents in the hysteresis loops can be inverted, depending on the sign of the polarization of the cell [16,36]. It is also seen in Fig. 7 that in presence of light the magnitude of the current increases, due to increased number of photogenerated charge carriers.

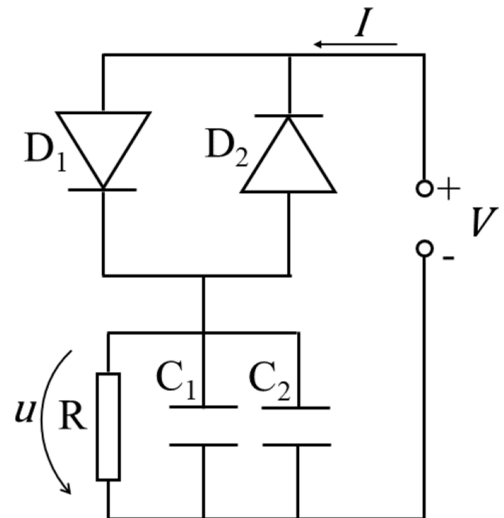An additional feature may be observed in the I-V curves of the sample

Fig. 9. A simple circuit model for the I-V characteristic with hysteresis. The direction of the current depends on the polarity of the main voltage V(t).
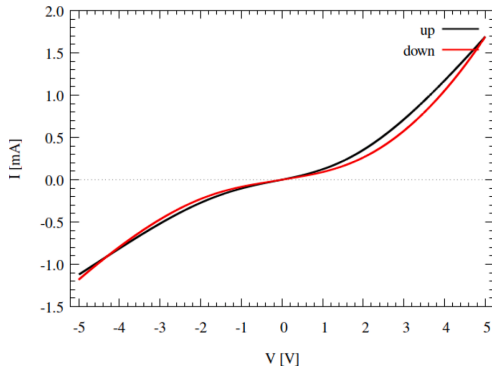
Fig. 10. The I-V characteristic with a normal current I_{C_1}. When the voltage V decreases (along the "down" curves) I_{C_1} is oriented against the source, if it is released by a normal capacitor, and consequently the total current is smaller than it was when V increased (the "up" curves).
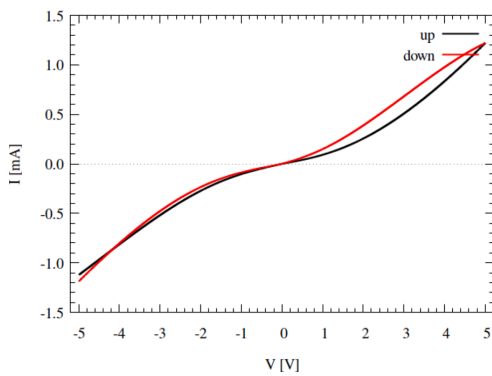

Fig. 11. The calculated I-V curves with the same parameters as in Fig. 9, but negative coefficient b. In this case the current for positive voltage is smaller when the voltage decreases, as observed for the samples of 700 nm.

SiNW$_{long}$, where the hysteresis for positive voltage reverses with decreasing the voltage rate, see Fig. 7f–j. An initial shoulder is visible at high rates on the "'up" curve, below the "down" curve, which then moves above the "down" curves at lower voltage rates, below 1.38 V/s. For lower voltage values the hysteresis loop becomes twisted. A possible interpretation is that in this situation another capacitor, C_2, is activated at a certain positive voltage, acting now in the regular manner, i.e. pumping current against the source, $I_{C_2} = b\ dQ_2/dt$ with the b coefficient always positive. In Fig. 12 we show the results with $C_2 = 0.6$ nF. Such an example looks qualitatively similar with the data for the sample SiNW$_{long}$ shown in Fig. 7h–j. Such a twisted hysteresis loop has been shown by Thissandier et al. [37], for an array of disconnected SiNWs, when the voltage was increased above a certain threshold.

We emphasize that the model used for explaining the I-V curves is primitive, and only qualitative. The magnitude of the b coefficient and of the capacitances have somehow a complementary character: we could increase one by decreasing the other one. However, for a small b value the capacitances would be unrealistic, and for this reason we believe their role is more like a trigger for activation of more charge carriers, typical for a small polarization field inside a Schottky or a p-n diode, or for a gate inside a transistor. Since the NWs are formed in p-type Si, with resistivity of the order of 1–10 Ω·cm, then shunt resistors should be included for a more realistic circuit model. Still, the development of a
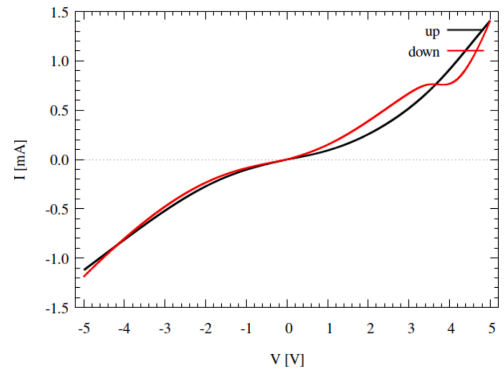

Fig. 12. The calculated I-V curves with the same parameters as in Figure 3, plus second capacitor $C_2 = 0.6$ nF which is activated gradually between voltages 0.5–1 V. The current created by the second capacitor has always a positive coefficient b.

more complex equivalent circuit is beyond the scope of this study.

4.1. Capacitance behavior under illumination

The C-V characteristics of the SiNW arrays measured at various frequencies are shown in Fig. 13a and b. Both structures exhibit reduced capacitance by increasing the frequency in the range 5–100 kHz, with maximum value of 9.9 nF, Fig. 14a, and 3.7 nF, Fig. 14b, at 5 kHz. However, the SiNW arrays with long NWs exhibit asymmetric behavior in the region of positive voltages, 0 to +10V, where large and switching hysteresis loops appear under the forward and reverse polarization. The presence of a positive or negative sign of the current due to traps, or equivalently, negative or positive capacitance, as proposed in the equivalent circuit, could explain the observed behavior.

Next we show the C-V characteristics measured under illumination with various wavelengths, in Fig. 14a and b. The capacitance of the structure with short NWs slightly increased when the structure is illuminated at 650 nm and 532 nm wavelength, Fig. 14a, while the structure with long NWs exhibits a significantly reduced capacitance under illumination at these wavelengths, Fig. 14b, likely due to the effect of photogenerated carries trapped at the surface states, lowering the value of the capacitive reactance. Fig. 14b also shows the capacitance changing slightly under illumination with 450 nm or 405 nm wavelength. In this case the photogenerated carriers behave like free carriers and determine the increase of the current intensity, see I-V characteristics in Fig. 7.

Fig. 15 shows the C-V characteristics under illumination with white light, with various intensities. Both structures exhibit higher capacitance when the light intensity increases, reaching 26 nF for the structure with short NWs, Fig. 15a, and 1.6 nF for SiNWs with long NWs, Fig. 15b, under illumination with 100 mW/cm². All the C-V curves present hysteresis, noticeable under positive applied voltage, 0,+10V. The structure with long NWs shows also a supplementary capacitance peak at positive applied voltage, that increases with the intensity of light. Also, the occurrence voltage shifts towards higher values, from 1.82 V to 2.16 V with increased light intensity.

5. Discussion and conclusions

The analysis of hysteresis exhibited by the I-V characteristics shown in Fig. 7a–e, reveals that charge carriers are trapped on the surface states in sample SiNW$_{short}$, with PL average lifetime of 60 μ s, when the voltage sweep rate varies from 5 V/s to 0.32 V/s. The hysteresis area linearly increases by lowering the sweep rate, see Fig. 8a, which suggests that the
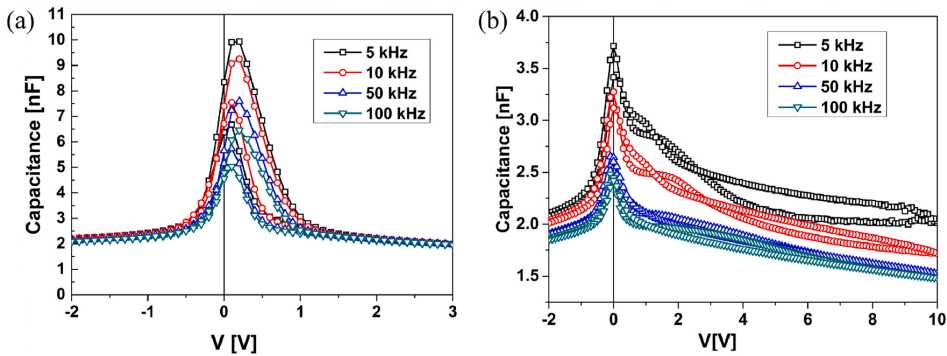
Fig. 13. Capacitance-voltage characteristics of Al/SiNWs/Al structures at various frequencies: (a) SiNWs with 700 nm length and (b) SiNWs with 1000 nm lengths.
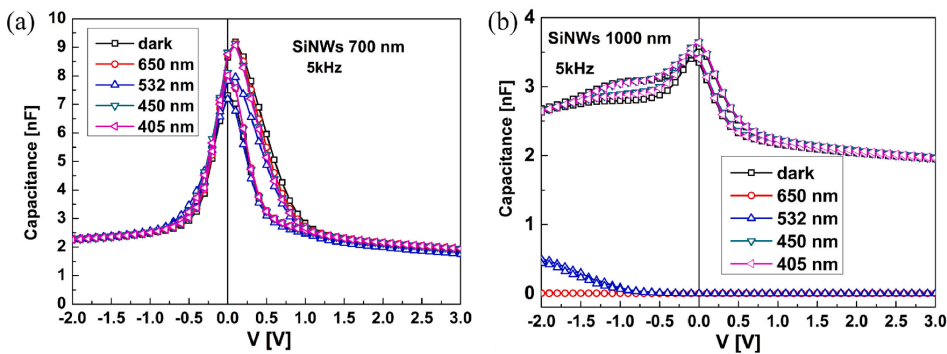

Fig. 14. Capacitance-voltage characteristics at 5 kHz, of Al/SiNWs/Al structures with: a) short (700 nm) NWs and b) long (1000 nm) NWs, under illumination with various wavelengths.
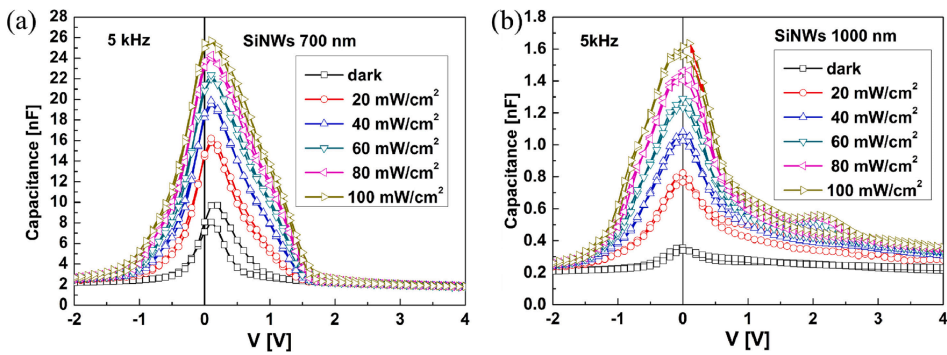

Fig. 15. Capacitance-voltage characteristics at 5 kHz, of Al/SiNWs/Al structures with: a) short NWs and (b) long NWs, as function of the white light intensity.

slow traps are involved in the process. The situation changes for the SiNW$_{long}$ sample, with PL average lifetime of 111 μ s, where larger hysteresis areas appear at faster voltage sweep rates, Fig. 7f–j. In fact, as the variation of the hysteresis area vs voltage sweep rate presented in Fig. 8a and b suggests, at slow V rates, of 0.32 V/s and 0.63 V/s, the slow traps act in the both structures. Also, since faster voltage sweeps are required to activate the fast surface states, the evolution of the hysteresis area in Fig. 8b indicates the presence of fast surface traps in the SiNW$_{long}$ sample. The I-V hysteresis in SiNWs prepared by MACE has also been obtained in Ref. [6], but the dependence on the voltage rate has not been

reported. The presence of the traps in the SiNWs can also be inferred from the non-ideal diode characteristic of the Schottky contacts, observed in the I-V characteristic [38].

The C-V response of this structure to excitation with various wavelengths suggests the presence of electron traps active at energy below 2.4 eV (observed in C-V responses at 1.9 eV and 2.33 eV irradiation), which are within the band gap of porous silicon [39–41]. Although these band gap values are also within the (broad) emission band limits observed in Fig. 5, they are different than the values derived from the maxima in the PL emission spectra, centered at 1.70 eV for SiNW$_{short}$ and

1.61 eV for SiNW$_{long}$, suggesting that different trap centers are involved in the PL emission and photogeneration processes.

In summary, the evolution of I–V hysteresis vs applied voltage rates was used to assess the effect of surface traps on transport properties of the pristine SiNWs arrays. The transition from an inverted to a direct hysteresis is demonstrated considering the effect of a capacitance associated with the surface traps which controls the charge current through the structure. The I–V and C–V characteristics measured under illumination with various wavelengths in the visible domain indicate that traps filling can be detected by tuning the photons energy. Using this method we assessed the energy range of the surface trap states energy of a SiNWs array.

However, the characterization methods used in this work, including PL, I–V and CV, bring evidence on effects due to the presence of surface states, but hardly allow an accurate assignment of their energy to a specific defect or complex. First, taking into account that different techniques may give specific energy values to the same defect type, and second, the fact that we deal with a highly irregular surface which allows a variety of local environments and therefore prevents an accurate identification of the defect type, then a schematic representation of the associated energy levels may be misleading.

Author Contributions

Conceptualization, RP, HGS, AM; methodology, investigation, EF, MTS, HÖÁ (MACE processes, electrical measurements), CR (x-ray diffraction), IM (PL), GC (SEM), RP, EF, HÖÁ (electrical characterization); modeling, AM, GAN.; formal analysis, RP, AM; data curation, EF, HGS; writing and original draft preparation, RP, NP, AM; writing, review and editing, RP, NP, AM, HGS, SI; visualization, EF, CR, IM, RP; funding acquisition, HGS, SI, and RP.

Declaration of Competing Interest

All authors have read and agreed to the published version of the manuscript. The authors declare no conflict of interest.

Acknowledgments

Supplementary material

Supplementary material associated with this article can be found, in the online version, at doi:10.1016/j.surfin.2022.102167.

References

[1] P.-J. Chien, T.-C. Wei, C.-Y. Chen, High-speed and direction-controlled formation of silicon nanowire arrays assisted by electric field, Nanoscale Res. Lett. 15 (1) (2020) 1–8.

[2] H. Han, Z. Huang, W. Lee, Metal-assisted chemical etching of silicon and nanotechnology applications, Nano Today 9 (3) (2014) 271–304.

[3] B. Azeredo, J. Sadhu, J. Ma, K. Jacobs, J. Kim, K. Lee, J. Eraker, X. Li, S. Sinha, N. Fang, et al., Silicon nanowires with controlled sidewall profile and roughness fabricated by thin-film dewetting and metal-assisted chemical etching, Nanotechnology 24 (22) (2013) 225305.

[4] L. Baraban, B. Ibarlucea, E. Baek, G. Cuniberti, Hybrid silicon nanowire devices and their functional diversity, Adv. Sci. 6 (15) (2019) 1900522.

[5] Y. Guan, G. Cao, X. Li, Single-nanowire silicon photodetectors with core-shell radial Schottky junction for self-powering application, Appl. Phys. Lett. 118 (15) (2021) 153904.

[6] F. Zaïbi, I. Slama, N. Beshchasna, J. Opitz, M. Mkandawire, R. Chtourou, Effect of etching parameters on the electrochemical response of silicon nanowires, J. Appl. Electrochem. 52 (2) (2022) 273–284.

[7] T. Moh, M. Nie, G. Pandraud, L. de Smet, E. Sudhölter, Q. Huang, P. Sarro, Effect of silicon nanowire etching on signal-to-noise ratio of sinw fets for (bio) sensor applications, Electron. Lett. 49 (13) (2013) 782–784.

[8] Y. Dan, K. Seo, K. Takei, J.H. Meza, A. Javey, K.B. Crozier, Dramatic reduction of surface recombination in situ surface passivation of silicon nanowires, Nano Lett. 11 (6) (2011) 2527–2532.

[9] G. Milano, S. Porro, I. Valov, C. Ricciardi, Recent developments and perspectives for memristive devices based on metal oxide nanowires, Adv. Electron. Mater. 5 (9) (2019) 1800909.

[10] S. Carrara, D. Sacchetto, M.-A. Doucey, C. Baj-Rossi, G. De Micheli, Y. Leblebici, Memristive-biosensors: a new detection method by using nanofabricated memristors, Sens. Actuators B 171 (2012) 449–457.

[11] D. Sacchetto, Y. Leblebici, G. De Micheli, Memristors and Memristive Systems, Springer, New York, NY, 2014, pp. 253–280, https://doi.org/10.1007/978-1-4614-9068-5_8.

[12] F. Puppo, F.L. Traversa, M. Di Ventra, G. De Micheli, S. Carrara, Surface trap mediated electronic transport in biofunctionalized silicon nanowires, Nanotechnology 27 (34) (2016) 345503.

[13] K.P. Rajeev, C. Opoku, V. Stolojan, M. Constantinou, M. Shkunov, Effect of nanowire-dielectric interface on the hysteresis of solution processed silicon nanowire fets, Nanosci. Nanoeng. 5 (2) (2017) 17–24.

[14] K. Seki, Equivalent circuit representation of hysteresis in solar cells that considers interface charge accumulation: potential cause of hysteresis in perovskite solar cells, Appl. Phys. Lett. 109 (3) (2016) 033905.

[15] B. Chen, M. Yang, X. Zheng, C. Wu, W. Li, Y. Yan, J. Bisquert, G. Garcia-Belmonte, K. Zhu, S. Priya, Impact of capacitive effect and ion migration on the hysteretic behavior of perovskite solar cells, J. Phys. Chem. Lett. 6 (23) (2015) 4693–4700.

[16] W. Tress, J.P. Correa Baena, M. Saliba, A. Abate, M. Graetzel, Inverted current–voltage hysteresis in mixed perovskite solar cells: polarization, energy barriers, and defect recombination, Adv. Energy Mater. 6 (19) (2016) 1600396.

[17] S.A. Moiz, A. Alahmadi, A.J. Aljohani, Design of silicon nanowire array for pedot: Pss-silicon nanowire-based hybrid solar cell, Energies 13 (15) (2020) 3797.

[18] P. Yu, J. Wu, S. Liu, J. Xiong, C. Jagadish, Z.M. Wang, Design and fabrication of silicon nanowires towards efficient solar cells, Nano Today 11 (6) (2016) 704–737.

[19] R. Rurali, Colloquium: structural, electronic, and transport properties of silicon nanowires, Rev. Mod. Phys. 82 (1) (2010) 427.

[20] E. Fakhri, M. Sultan, A. Manolescu, S. Ingvarsson, N. Plugaru, R. Plugaru, H. Svavarsson, Synthesis and photoluminescence study of silicon nanowires obtained by metal assisted chemical etching. 2021 International Semiconductor Conference (CAS), IEEE, 2021, pp. 147–150.

[21] H. Stanchu, A. Kuchuk, M. Barchuk, Y.I. Mazur, V. Kladko, Z.M. Wang, D. Rafaja, G. Salamo, Asymmetrical reciprocal space mapping using x-ray diffraction: a technique for structural characterization of GAN/ALNsuperlattices, CrystEngComm 19 (22) (2017) 2977–2982.

[22] V.M. Kaganer, B. Jenichen, O. Brandt, Elastic versus plastic strain relaxation in coalesced gan nanowires: an x-ray diffraction study, Phys. Rev. Appl. 6 (6) (2016) 064023.

[23] C. Romanitan, M. Kusko, M. Popescu, P. Varasteanu, A. Radoi, C. Pachiu, Unravelling the strain relaxation processes in silicon nanowire arrays by x-ray diffraction, J. Appl. Crystallogr. 52 (5) (2019) 1077–1086.

[24] S. Congli, H. Hao, F. Huanhuan, X. Jingjing, C. Yu, J. Yong, J. Zhifeng, S. Xiaosong, Synthesis of porous silicon nano-wires and the emission of red luminescence, Appl. Surf. Sci. 282 (2013) 259–263.

[25] L. Canham, Introductory lecture: origins and applications of efficient visible photoluminescence from silicon-based nanostructures, Faraday Discuss. 222 (2020) 10–81.

[26] D. Jung, H. Sohn, Y. Kim, Optical characterization of luminescent silicon nanowires, J. Korean Phys. Soc. 74 (2) (2019) 140–144.

[27] L. Lin, S. Guo, X. Sun, J. Feng, Y. Wang, Synthesis and photoluminescence properties of porous silicon nanowire arrays, Nanoscale Res. Lett. 5 (11) (2010) 1822–1828.

[28] S.A. Razek, M.A. Swillam, N.K. Allam, Vertically aligned crystalline silicon nanowires with controlled diameters for energy conversion applications: experimental and theoretical insights, J. Appl. Phys. 115 (19) (2014) 194305.

[29] M. Naffeti, P.A. Postigo, R. Chtourou, M.A. Zaïbi, Highly efficient silicon nanowire surface passivation by bismuth nano-coating for multifunctional bi@ sinws heterostructures, Nanomaterials 10 (8) (2020) 1434.

[30] I. Leontis, A. Othonos, A.G. Nassiopoulou, Structure, morphology, and photoluminescence of porous si nanowires: effect of different chemical treatments, Nanoscale Res Lett 8 (1) (2013) 1–7.

[31] H. Okayama, K. Fukami, R. Plugaru, T. Sakka, Y.H. Ogata, Ordering and disordering of macropores formed in prepatterned p-type silicon, J Electrochem Soc 157 (1) (2009) D54.

[32] C. Amri, H. Ezzaouia, R. Ouertani, Photoluminescence origin of lightly doped silicon nanowires treated with acid vapor etching, Chin. J. Phys. 63 (2020) 325–336.

[33] R.-C. Wang, C.-Y. Chao, W.-S. Su, Electrochemically controlled fabrication of lightly doped porous Si nanowire arrays with excellent antireflective and self-cleaning properties, Acta Mater. 60 (5) (2012) 2097–2103.

[34] M. Dawood, T. Liew, P. Lianto, M. Hong, S. Tripathy, J. Thong, W. Choi, Interference lithographically defined and catalytically etched, large-area silicon nanocones from nanowires, Nanotechnology 21 (20) (2010) 205305.

[35] S.M. Sze, K.K. Ng, Physics of Semiconductor Devices, third ed., John Wiley & Sons, Ltd., 2006, pp. 134–196.

[36] G.A. Nemnes, C. Besleaga, A.G. Tomulescu, I. Pintilie, L. Pintilie, K. Torfason, A. Manolescu, Dynamic electrical behavior of halide perovskite based solar cells, Sol. Energy Mater. Sol. Cells 159 (2017) 197–203.

[37] F. Thissandier, A. Le Comte, O. Crosnier, P. Gentile, G. Bidan, E. Hadji, T. Brousse, S. Sadki, Highly doped silicon nanowires based electrodes for micro-electrochemical capacitor applications, Electrochem. Commun. 25 (2012) 109–111.

[38] A. Rouis, N. Hizem, M. Hassen, A. Kalboussi, Electrical properties of silicon nanowires schottky barriers prepared by mace at different etching time, Silicon (2021).

[39] J. Rams, B. Mendez, G. Craciun, R. Plugaru, J. Piqueras, Cathodoluminescence enhancement in porous silicon cracked in vacuum, Appl. Phys. Lett. 74 (12) (1999) 1728–1730.

[40] Z. Chen, T.-Y. Lee, G. Bosman, Electrical band gap of porous silicon, Appl. Phys. Lett. 64 (25) (1994) 3446–3448.

[41] T. Van Buuren, T. Tiedje, J. Dahn, B. Way, Photoelectron spectroscopy measurements of the band gap in porous silicon, Appl. Phys. Lett. 63 (21) (1993) 2911–2913.

102

Bibliography

[1] H. Ö. Árnason, K. Torfason, A. Manolescu, and Á. Valfells, "Simulation of short pulse photoemission in a micro-diode with implications for optimal beam brightness," Jan. 2023, arXiv:2301.06123 [physics]. DOI: 10.48550/arXiv.2301.06123.

[2] M. T. Sultan, H. Ö. Árnason, M. Kateb, A. Manolescu, H. G. Svavarsson, and Á. Valfells, "Enhanced photoemission from surface modulated GaAs:Ge," en, *Nano Select*, vol. 2, no. 12, nano.202100012, May 2021, ISSN: 2688-4011, 2688-4011. DOI: 10.1002/nano.202100012.

[3] M. T. Sultan, H. Ö. Árnason, S. Ingvarsson, *et al.*, "Facile formation of self-assembled Ga droplets on GaAs (001) substrate," en, in *2021 International Semiconductor Conference (CAS)*, Romania: IEEE, Oct. 2021, pp. 35–38, ISBN: 978-1-66543-571-0. DOI: 10.1109/CAS52836.2021.9604129.

[4] E. Fakhri, R. Plugaru, M. T. Sultan, *et al.*, "Piezoresistance Characterization of Silicon Nanowires in Uniaxial and Isostatic Pressure Variation," en, *Sensors*, vol. 22, no. 17, p. 6340, Aug. 2022, ISSN: 1424-8220. DOI: 10.3390/s22176340.

[5] R. Plugaru, E. Fakhri, C. Romanitan, *et al.*, *Structure and electrical behavior of silicon nanowires prepared by MACE process*, en, Oct. 2022. DOI: 10.1016/j.surfin.2022.102167.

[6] J. R. R. Tolkien, *The Return of the King* (The Lord of the Rings), en, Fourth. Urwin Paperbacks, 1981, vol. 3, ISBN: 0-04-823187-8.

[7] G. Scalari, C. Walther, M. Fischer, *et al.*, "THz and sub-THz quantum cascade lasers," io, *Laser and Photonics Reviews*, vol. 3, no. 1-2, pp. 45–66, 2009, ISSN: 18638880. DOI: 10.1002/lpor.200810030.

[8] P. H. Siegel, "Terahertz technology," en, *IEEE Transactions on Microwave Theory and Techniques*, vol. 50, no. 3, pp. 910–928, 2002, ISSN: 00189480. DOI: 10.1109/22.989974.

[9] M. Tonouchi, "Cutting-edge terahertz technology," nl, *Nature Photonics*, vol. 1, no. 2, pp. 97–105, 2007, ISSN: 17494885. DOI: 10.1038/nphoton.2007.3.

[10]   C. R. Williams, S. R. Andrews, S. A. Maier, A. I. Fernández-Domínguez, L. Martín-Moreno, and F. J. García-Vidal, "Highly confined guiding of terahertz surface plasmon polaritons on structured metal surfaces," en, *Nature Photonics*, vol. 2, no. 3, pp. 175–179, 2008, ISSN: 17494885. DOI: 10.1038/nphoton.2007.301.

[11]   J. H. Booske, "Plasma physics and related challenges of millimeter-wave-to-terahertz and high power microwave generation," de, *Physics of Plasmas*, vol. 15, no. 5, pp. 1–16, 2008, ISSN: 1070664X. DOI: 10.1063/1.2838240.

[12]   J. Federici and L. Moeller, "Review of terahertz and subterahertz wireless communications," fr, *Journal of Applied Physics*, vol. 107, no. 11, p. 11 101, 2010, ISSN: 00218979. DOI: 10.1063/1.3386413.

[13]   J. H. Booske, R. J. Dobbs, C. D. Joye, *et al.*, "Vacuum electronic high power terahertz sources," en, *IEEE Transactions on Terahertz Science and Technology*, vol. 1, no. 1, pp. 54–75, 2011, ISSN: 2156342X. DOI: 10.1109/TTHZ.2011.2151610.

[14]   B. S. Williams, "Terahertz quantum-cascade lasers," en, *Nature Photonics*, vol. 1, no. 9, pp. 517–525, Sep. 2007, Number: 9 Publisher: Nature Publishing Group, ISSN: 1749-4893. DOI: 10.1038/nphoton.2007.166.

[15]   P. U. Jepsen, D. G. Cooke, and M. Koch, "Terahertz spectroscopy and imaging - Modern techniques and applications," fr, *Laser and Photonics Reviews*, vol. 5, no. 1, pp. 124–166, 2011, ISSN: 18638880. DOI: 10.1002/lpor.201000011.

[16]   P. H. Siegel, "Terahertz technology in biology and medicine," en, *IEEE Transactions on Microwave Theory and Techniques*, vol. 52, no. 10, pp. 2438–2447, 2004, ISSN: 00189480. DOI: 10.1109/TMTT.2004.835916.

[17]   C. D. Alwis, A. Kalla, Q.-V. Pham, *et al.*, "Survey on 6G Frontiers: Trends, Applications, Requirements, Technologies and Future Research," *IEEE Open Journal of the Communications Society*, vol. 2, pp. 836–886, 2021, Conference Name: IEEE Open Journal of the Communications Society, ISSN: 2644-125X. DOI: 10.1109/OJCOMS.2021.3071496.

[18]   M. S. Vitiello, G. Scalari, B. Williams, and P. D. Natale, "Quantum cascade lasers: 20 years of challenges," EN, *Optics Express*, vol. 23, no. 4, pp. 5167–5182, Feb. 2015, Publisher: Optica Publishing Group, ISSN: 1094-4087. DOI: 10.1364/OE.23.005167.

[19]   R. Symons, "Tubes: Still vital after all these years," *IEEE Spectrum*, vol. 35, no. 4, pp. 52–63, Apr. 1998, Conference Name: IEEE Spectrum, ISSN: 1939-9340. DOI: 10.1109/6.666962.

[20] R. J. Barker, N. C. Luhmann, J. H. Booske, and G. S. Nusinovich, *Modern Microwave and Millimeter-Wave Power Electronics*. Apr. 2005, Publication Title: Modern Microwave and Millimeter-Wave Power Electronics ADS Bibcode: 2005mmmp.book.....B.

[21] R. L. Ives, "Microfabrication of high-frequency vacuum electron devices," fr, *IEEE Transactions on Plasma Science*, vol. 32, no. 3 I, pp. 1277–1291, 2004, ISSN: 00933813. DOI: 10.1109/TPS.2004.827595.

[22] Y. M. Shin, L. R. Barnett, D. Gamzina, N. C. Luhmann, M. Field, and R. Borwick, "Terahertz vacuum electronic circuits fabricated by UV lithographic molding and deep reactive ion etching," en, *Applied Physics Letters*, vol. 95, no. 18, p. 181 505, 2009, ISSN: 00036951. DOI: 10.1063/1.3259823.

[23] S. Bhattacharjee, J. H. Booske, C. L. Kory, *et al.*, "Folded waveguide travelingwave tube sources for terahertz radiation," en, *IEEE Transactions on Plasma Science*, vol. 32, no. 3 I, pp. 1002–1014, 2004, ISSN: 00933813. DOI: 10.1109/TPS.2004.828886.

[24] R. F. Greene, *Vacuum Microelectronics*, W. Zhu, Ed. New York, USA: John Wiley & Sons, Inc., Oct. 1989, vol. 00, Publication Title: Vacuum, ISBN: 0-471-32244-X. DOI: 10.1002/0471224332.

[25] Á. Valfells, D. W. Feldman, M. Virgo, P. G. O'Shea, and Y. Y. Lau, "Effects of pulse-length and emitter area on virtual cathode formation in electron guns," *Physics of Plasmas*, vol. 9, no. 5, pp. 2377–2382, 2002, ISSN: 1070664X. DOI: 10.1063/1.1463065.

[26] P. Zhang, A. Valfells, L. K. Ang, J. W. Luginsland, and Y. Y. Lau, "100 Years of the Physics of Diodes," en, *Applied Physics Reviews*, vol. 4, no. 1, p. 11 304, 2017, ISBN: 1931-9401, ISSN: 19319401. DOI: 10.1063/1.4978231.

[27] G. Dorda, "Piezoresistance in quantized conduction bands in silicon inversion layers," *Journal of Applied Physics*, vol. 42, no. 5, pp. 2053–2060, 1971.

[28] C. S. Smith, "Piezoresistance effect in germanium and silicon," *Physics Review*, vol. 94, pp. 42–49, 1954.

[29] R. He and P. Yang, "Giant piezoresistance effect in silicon nanowires," *Nature nanotechnology*, vol. 1, no. 1, pp. 42–46, 2006.

[30] S. Zhang, L. Lou, and C. Lee, "Piezoresistive silicon nanowire based nanoelectromechanical system cantilever air flow sensor," *Applied Physics Letters*, vol. 100, no. 2, p. 023 111, 2012.

[31] W. Cheng, L. Yu, D. Kong, *et al.*, "Fast-response and low-hysteresis flexible pressure sensor based on silicon nanowires," *IEEE Electron Device Letters*, vol. 39, no. 7, pp. 1069–1072, 2018.

[32] T.-D. Nguyen and J. S. Lee, "Recent development of flexible tactile sensors and their applications," *Sensors*, vol. 22, no. 1, p. 50, 2021.

[33] C. Kim, H. Ahn, and T. Ji, "Flexible pressure sensors based on silicon nanowire array built by metal-assisted chemical etching," *IEEE Electron Device Letters*, vol. 41, no. 8, pp. 1233–1236, 2020.

[34] R. Ghosh, M. S. Song, J. Park, *et al.*, "Fabrication of piezoresistive si nanorod-based pressure sensor arrays: A promising candidate for portable breath monitoring devices," *Nano Energy*, vol. 80, p. 105 537, 2021.

[35] D. Shiri, Y. Kong, A. Buin, and M. P. 1. Anantram, "Strain induced change of bandgap and effective mass in silicon nanowires," *Applied Physics Letters*, vol. 93, p. 07 314, 2008.

[36] J. Zhang, Y. Zhao, Y. Ge, M. Li, L. Yang, and X. Mao, "Design optimization and fabrication of high-sensitivity soi pressure sensors with high signal-to-noise ratios based on silicon nanowire piezoresistors," *Micromachines*, vol. 7, no. 10, p. 187, 2016.

[37] A. Rowe, "Piezoresistance in silicon and its nanostructures," *Journal of Materials Research*, vol. 29, no. 6, pp. 731–744, 2014.

[38] P. Neuzil, C. C. Wong, and J. Reboud, "Electrically controlled giant piezoresistance in silicon nanowires," *Nano letters*, vol. 10, no. 4, pp. 1248–1252, 2010.

[39] A. B. Arons and M. B. Peppard, "Einstein's Proposal of the Photon Concepta Translation of the Annalen der Physik Paper of 1905," en, *American Journal of Physics*, vol. 33, no. 5, pp. 367–374, May 1965, ISSN: 0002-9505, 1943-2909. DOI: 10.1119/1.1971542.

[40] *On the Negative Radiation from Hot Platinum...* University Press, 1901.

[41] O. W. Richardson and J. J. Thomson, "XIII. The electrical conductivity imparted to a vacuum by hot conductors," *Philosophical Transactions of the Royal Society of London. Series A, Containing Papers of a Mathematical or Physical Character*, vol. 201, no. 331-345, pp. 497–549, Jan. 1903, Publisher: Royal Society. DOI: 10.1098/rsta.1903.0023.

[42] I. Langmuir, "The effect of space charge and residual gases on thermionic currents in high vacuum," *Physical Review*, vol. 2, no. 6, pp. 450–486, 1913.

[43] I. Langmuir and K. B. Blodgett, "Currents limited by space charge between coaxial cylinders," *Physical Review*, vol. 22, no. 4, 1923, ISSN: 0031899X. DOI: 10.1103/PhysRev.22.347.

[44] I. Langmuir and K. B. Blodgett, "Currents limited by space charge between concentric spheres," *Physical Review*, vol. 24, no. 1, 1924, ISSN: 0031899X. DOI: 10.1103/PhysRev.24.49.

[45] R. H. Fowler and L. Nordheim, "Electron emission in intense electric fields," *Proceedings of the Royal Society of London. Series A, Containing Papers of a Mathematical and Physical Character*, vol. 119, no. 781, pp. 173–181, May 1928, Publisher: Royal Society. DOI: 10.1098/rspa.1928.0091.

[46] R. H. Fowler, "The photo-electric threshold frequency and the thermionic work function," en, *Proceedings of the Royal Society of London. Series A, Containing Papers of a Mathematical and Physical Character*, vol. 118, no. 779, pp. 229–232, Mar. 1928, ISSN: 0950-1207, 2053-9150. DOI: 10.1098/rspa.1928.0047.

[47] A. Sommerfeld, "Zur Elektronentheorie der Metalle auf Grund der Fermischen Statistik," de, *Zeitschrift für Physik*, vol. 47, no. 1, pp. 1–32, Jan. 1928, ISSN: 0044-3328. DOI: 10.1007/BF01391052.

[48] R. H. Fowler, "The Analysis of Photoelectric Sensitivity Curves for Clean Metals at Various Temperatures," en, *Phys. Rev.*, vol. 38, no. 1, pp. 45–56, Jul. 1931, Publisher: American Physical Society, ISSN: 0031-899X. DOI: 10.1103/PhysRev.38.45.

[49] L. A. DuBridge, "A Further Experimental Test of Fowler's Theory of Photoelectric Emission," en, *Phys. Rev.*, vol. 39, no. 1, pp. 108–118, Jan. 1932, Publisher: American Physical Society, ISSN: 0031-899X. DOI: 10.1103/PhysRev.39.108.

[50] L. A. DuBridge and W. W. Roehr, "Photoelectric and Thermionic Properties of Palladium," en, *Phys. Rev.*, vol. 39, no. 1, pp. 99–107, Jan. 1932, ISSN: 0031-899X. DOI: 10.1103/PhysRev.39.99.

[51] L. A. DuBridge and W. W. Roehr, "The Thermionic and Photoelectric Work Functions of Molybdenum," en, *Phys. Rev.*, vol. 42, no. 1, pp. 52–57, Oct. 1932, ISSN: 0031-899X. DOI: 10.1103/PhysRev.42.52.

[52] L. A. DuBridge, "Theory of the Energy Distribution of Photoelectrons," en, *Phys. Rev.*, vol. 43, no. 9, pp. 727–741, May 1933, ISSN: 0031-899X. DOI: 10.1103/PhysRev.43.727.

[53] L. A. DuBridge and R. C. Hergenrother, "The Effect of Temperature on the Energy Distribution of Photoelectrons. I. Normal Energies," *Physical Review*, vol. 44, no. 11, pp. 861–865, Dec. 1933, Publisher: American Physical Society. DOI: 10.1103/PhysRev.44.861.

[54] W. W. Roehr, "The Effect of Temperature on the Energy Distribution of Photoelectrons. II. Total Energies," en, *Phys. Rev.*, vol. 44, no. 11, pp. 866–871, Dec. 1933, ISSN: 0031-899X. DOI: 10.1103/PhysRev.44.866.

[55] A. Kahn, "Fermi level, work function and vacuum level," en, *Materials Horizons*, vol. 3, no. 1, pp. 7–10, 2016, ISSN: 2051-6347, 2051-6355. DOI: 10.1039/C5MH00160A.

[56] K. L. Jensen, *Introduction to the physics of electron emission*, First edition. Hoboken, New Jersey: John Wiley & Sons, Inc, 2017, ISBN: 978-1-119-05189-3.

[57] Y. Y. Lau, "Simple Theory for the Two-Dimensional Child-Langmuir Law," en, *Physical Review Letters*, vol. 87, no. 27, pp. 278301–278301–3, 2001, ISBN: 0031-9007, 1079-7114, ISSN: 10797114. DOI: 10.1103/PhysRevLett.87.278301.

[58] L. K. Ang, T. J. T. Kwan, and Y. Y. Lau, "New Scaling of Child-Langmuir Law in the Quantum Regime," *Physical Review Letters*, vol. 91, no. 20, p. 208303, Nov. 2003, Publisher: American Physical Society. DOI: 10.1103/PhysRevLett.91.208303.

[59] W. S. Koh, L. K. Ang, and T. J. Kwan, "Three-dimensional ChildLangmuir law for uniform hot electron emission," en, *Physics of Plasmas*, vol. 12, no. 5, p. 053107, May 2005, ISBN: 1070-664X, 1089-7674, ISSN: 1070-664X, 1089-7674. DOI: 10.1063/1.1913612.

[60] L. K. Ang, W. S. Koh, Y. Y. Lau, and T. J. T. Kwan, "Space-charge-limited flows in the quantum regime," *Physics of Plasmas*, vol. 13, no. 5, p. 056701, May 2006, Publisher: American Institute of Physics, ISSN: 1070-664X. DOI: 10.1063/1.2174834.

[61] L. K. Ang and P. Zhang, "Ultrashort-Pulse Child-Langmuir Law in the Quantum and Relativistic Regimes," *Physical Review Letters*, vol. 98, no. 16, p. 164802, Apr. 2007, Publisher: American Physical Society. DOI: 10.1103/PhysRevLett.98.164802.

[62] J. W. Luginsland, Y. Y. Lau, R. J. Umstattd, and J. J. Watrous, "Beyond the Child-Langmuir law: A review of recent results on multidimensional space-charge-limited flow," en, *Physics of Plasmas*, vol. 9, no. 5, pp. 2371–2376, 2002, ISSN: 1070664X. DOI: 10.1063/1.1459453.

[63] J. B. Gunnarsson, K. Torfason, A. Manolescu, and A. Valfells, "Space-Charge Limited Current From a Finite Emitter in Nano- and Microdiodes," en, *IEEE Transactions on Electron Devices*, vol. 68, no. 1, pp. 342–346, Jan. 2021, Conference Name: IEEE Transactions on Electron Devices, ISSN: 0018-9383, 1557-9646. DOI: 10.1109/TED.2020.3037280.

[64] A. H. Zewail and J. M. Thomas, *4D electron microscopy: imaging in space and time*. London : Hackensack, NJ: Imperial College Press ; Distributed by World Scientific Pub, 2010, OCLC: ocn299716296, ISBN: 978-1-84816-390-4.

[65] S. Sun, X. Sun, D. Bartles, *et al.*, "Direct imaging of plasma waves using ultrafast electron microscopy," *Structural Dynamics*, vol. 7, no. 6, p. 064301, Nov. 2020, Publisher: American Institute of Physics. DOI: 10.1063/4.0000044.

[66] W. A. Barletta, J. Bisognano, J. N. Corlett, *et al.*, "Free electron lasers: Present status and future challenges," en, *Nuclear Instruments and Methods in Physics Research Section A: Accelerators, Spectrometers, Detectors and Associated Equipment*, vol. 618, no. 1, pp. 69–96, Jun. 2010, ISSN: 0168-9002. DOI: 10.1016/j.nima.2010.02.274.

[67] M. Reiser, P. O'Shea, S. Bernal, and R. Kishek, *Theory and Design of Charged Particle Beams: Second Edition*, en, 2nd, updated and expanded ed. New York, NY: Wiley, 2008, Publication Title: Theory and Design of Charged Particle Beams: Second Edition, ISBN: 978-3-527-40741-5. DOI: 10.1002/9783527622047.

[68] D. A. Edwards and M. J. Syphers, *An introduction to the physics of high energy accelerators*. John Wiley & Sons, Inc, 1993, ISBN: 978-0-471-55163-8.

[69] P. Zhang, Y. S. Ang, A. L. Garner, Á. Valfells, J. W. Luginsland, and L. K. Ang, "Spacecharge limited current in nanodiodes: Ballistic, collisional, and dynamical effects," en, *Journal of Applied Physics*, vol. 129, no. 10, p. 100 902, Mar. 2021, Publisher: American Institute of Physics, ISSN: 0021-8979, 1089-7550. DOI: 10.1063/5.0042355.

[70] I. V. Bazarov, B. M. Dunham, and C. K. Sinclair, "Maximum Achievable Beam Brightness from Photoinjectors," en, *Physical Review Letters*, vol. 102, no. 10, p. 104 801, Mar. 2009, ISSN: 0031-9007, 1079-7114. DOI: 10.1103/PhysRevLett.102.104801.

[71] M. Kuwahara, Y. Nambo, K. Aoki, *et al.*, "The Boersch effect in a picosecond pulsed electron beam emitted from a semiconductor photocathode," *Applied Physics Letters*, vol. 109, no. 1, p. 013 108, Jul. 2016, Publisher: American Institute of Physics, ISSN: 0003-6951. DOI: 10.1063/1.4955457.

[72] A. Sitek, K. Torfason, A. Manolescu, and Á. Valfells, "Space-Charge Effects in the Field-Assisted Thermionic Emission from Nonuniform Cathodes," *Physical Review Applied*, vol. 15, no. 1, p. 014 040, Jan. 2021, Publisher: American Physical Society. DOI: 10.1103/PhysRevApplied.15.014040.

[73] K. Torfason, A. Valfells, and A. Manolescu, "Molecular dynamics simulations of field emission from a prolate spheroidal tip," en, *Physics of Plasmas*, vol. 23, no. 12, p. 123 119, 2016, arXiv: 1608.06789 ISBN: 1070-664X, 1089-7674, ISSN: 10897674. DOI: 10.1063/1.4972821.

[74] M. Ilkov, "Space-charge dynamics in microdiodes," Ph.D. dissertation, 2015.

[75] H. Grubmüller, H. Heller, A. Windemuth, and K. Schulten, "Generalized Verlet Algorithm for Efficient Molecular Dynamics Simulations with Long-range Interactions," *Molecular Simulation*, vol. 6, no. 1-3, pp. 121–142, Mar. 1991, Publisher: Taylor & Francis, ISSN: 0892-7022. DOI: 10.1080/08927029108022142.

[76] E. Hairer, C. Lubich, and G. Wanner, "Geometric numerical integration illustrated by the StörmerVerlet method," en, *Acta Numerica*, vol. 12, pp. 399–450, May 2003, Publisher: Cambridge University Press, ISSN: 1474-0508, 0962-4929. DOI: 10.1017/S0962492902000144.

[77] D. Marx and J. Hutter, *Ab Initio Molecular Dynamics: Basic Theory and Advanced Methods*, en. Cambridge University Press, Apr. 2009, Google-Books-ID: VRZUw8Wk4CIC, ISBN: 978-1-139-47719-2.

[78] S. Ramo, "Currents Induced by Electron Motion," *Proceedings of the IRE*, vol. 27, no. 9, pp. 584–585, 1939, ISSN: 00968390. DOI: 10.1109/JRPROC.1939.228757.

[79] W. Shockley, "Currents to conductors induced by a moving point charge," *Journal of Applied Physics*, vol. 9, no. 10, pp. 635–636, Oct. 1938, Publisher: American Institute of PhysicsAIP, ISSN: 00218979. DOI: 10.1063/1.1710367.

[80] K. L. Jensen, "General formulation of thermal, field, and photoinduced electron emission," *Journal of Applied Physics*, vol. 102, no. 2, p. 024 911, Jul. 2007, Publisher: American Institute of Physics, ISSN: 0021-8979. DOI: 10.1063/1.2752122.

[81] R. J. Umstattd, C. G. Carr, C. L. Frenzen, J. W. Luginsland, and Y. Y. Lau, "A simple physical derivation of ChildLangmuir space-charge-limited emission using vacuum capacitance," *American Journal of Physics*, vol. 73, no. 2, pp. 160–163, Feb. 2005, Publisher: American Association of Physics Teachers, ISSN: 0002-9505. DOI: 10.1119/1.1781664.

[82] R. J. Umstattd and J. W. Luginsland, "Two-Dimensional Space-Charge-Limited Emission: Beam-Edge Characteristics and Applications," *Physical Review Letters*, vol. 87, no. 14, p. 145 002, Sep. 2001, Publisher: American Physical Society. DOI: 10.1103/PhysRevLett.87.145002.

[83] M. A. Lieberman and A. J. Lichtenberg, *Principles of plasma discharges and materials processing*. New York: Wiley, 1994, ISBN: 978-0-471-00577-3.

[84] M. T. Sultan, A. V. Maraloiu, I. Stavarache, *et al.*, "Fabrication and characterization of Si1-xGex nanocrystals in as-grown and annealed structures: A comparative study," en, *Beilstein Journal of Nanotechnology*, vol. 10, no. 1, pp. 1873–1882, Sep. 2019, Publisher: Beilstein-Institut, ISSN: 2190-4286. DOI: 10.3762/bjnano.10.182.

[85] H. Liu, Y. Jin, M. Lin, *et al.*, "Growth and in-plane undulations of GaAs/Ge superlattices on [001]-oriented Ge and GaAs substrates: Formation of regular 3D island-in-network nanostructures," *Journal of Materials Chemistry C*, vol. 6, no. 47, pp. 13 059–13 068, Dec. 2018, Publisher: Royal Society of Chemistry, ISSN: 20507526. DOI: 10.1039/c8tc04799e.

[86] Y. Cheng, C. Chia, Y. Chai, and D. Chi, "High quality Ge epitaxy on GaAs (100) grown by metal-organic chemical vapor deposition," en, *Thin Solid Films*, vol. 522, pp. 340–344, Nov. 2012, Publisher: Elsevier ISBN: 00406090, ISSN: 00406090. DOI: 10.1016/j.tsf.2012.08.044.

[87] C. Heyn, T. Bartsch, S. Sanguinetti, D. Jesson, and W. Hansen, "Dynamics of mass transport during nanohole drilling by local droplet etching," en, *Nanoscale Research Letters*, vol. 10, no. 1, p. 67, Dec. 2015, Publisher: Springer New York LLC, ISSN: 1931-7573, 1556-276X. DOI: 10.1186/s11671-015-0779-5.

[88] Z. M. Wang, B. L. Liang, K. A. Sablon, and G. J. Salamo, "Nanoholes fabricated by self-assembled gallium nanodrill on GaAs(100)," *Applied Physics Letters*, vol. 90, no. 11, p. 113 120, Mar. 2007, Publisher: American Institute of Physics, ISSN: 0003-6951. DOI: 10.1063/1.2713745.

[89] P. Alonso-González, D. Fuster, L. González, J. Martín-Sánchez, and Y. González, "Low density InAs quantum dots with control in energy emission and top surface location," en, *Applied Physics Letters*, vol. 93, no. 18, p. 183 106, Nov. 2008, ISBN: 1131202007, ISSN: 0003-6951, 1077-3118. DOI: 10.1063/1.3021070.

[90] R. Fornari, C. Frigeri, and R. Gleichmann, "Structural and electrical properties of n-type bulk gallium arsenide grown from non-stoichiometric melts," *Journal of Electronic Materials*, vol. 18, no. 2, pp. 185–189, Mar. 1989, Publisher: Springer-Verlag, ISSN: 03615235. DOI: 10.1007/BF02657406.

[91] H. Jung, H. Künzel, K. Ploog, and H. Kiinzel, "Influence of arsenic vapor species on electrical and optical properties of MBE grown GaAs," *Journal de Physique Colloques*, no. C5, p. 43, 1982. DOI: 10.1051/jphyscol:1982517ï.

[92] G.-R. Lin and C.-C. Hsu, "Optical transmission spectroscopy of semi-insulating GaAs substrate implanted by arsenic ions at different dosages," en, *Journal of Applied Physics*, vol. 89, no. 11, pp. 6536–6538, Jun. 2001, ISSN: 0021-8979, 1089-7550. DOI: 10.1063/1.1370088.

[93] E. Garwin, R. Kirby, C. Sinclair, and A. Roder, "Oxide effects on photoemission from high current GaAs photocathodes," *Vacuum*, vol. 31, no. 10-12, pp. 553–556, Oct. 1981, Publisher: Stanford University, Stanford, California 94305, ISSN: 0042207X. DOI: 10.1016/0042-207X(81)90063-4.

[94] N. Chanlek, J. D. Herbert, R. M. Jones, L. B. Jones, K. J. Middleman, and B. L. Militsyn, "The degradation of quantum efficiency in negative electron affinity GaAs photocathodes under gas exposure," en, *Journal of Physics D: Applied Physics*, vol. 47, no. 5, p. 55 110, Feb. 2014, Publisher: IOP Publishing, ISSN: 0022-3727, 1361-6463. DOI: 10.1088/0022-3727/47/5/055110.

[95] D. N. Butcher and B. J. Sealy, "The thermal oxidation of GaAs," *Journal of Physics D: Applied Physics*, vol. 11, no. 10, pp. 1451–1456, Jul. 1978, Publisher: IOP Publishing, ISSN: 00223727. DOI: 10.1088/0022-3727/11/10/012.

[96] W. F. Wang, K. Y. Cheng, and K. C. Hsieh, "Germanium diffusion with vapor-phase GeAs and oxygen co-incorporation in GaAs," en, *AIP Advances*, vol. 8, no. 1, p. 15 230, Jan. 2018, Publisher: American Institute of Physics Inc. ISBN: 2158-3226, ISSN: 21583226. DOI: 10.1063/1.5005979.

[97] W. Liu, S. Zhang, M. Stutzman, and M. Poelker, "Effects of ion bombardment on bulk GaAs photocathodes with different surface-cleavage planes," *Physical Review Accelerators and Beams*, vol. 19, no. 10, p. 103 402, Oct. 2016, Publisher: American Physical Society. DOI: 10.1103/PhysRevAccelBeams.19.103402.

[98] J. Biswas, E. Wang, M. Gaowei, W. Liu, O. Rahman, and J. T. Sadowski, "High quantum efficiency GaAs photocathodes activated with Cs, O2, and Te," *AIP Advances*, vol. 11, no. 2, p. 025 321, Feb. 2021, Publisher: American Institute of Physics. DOI: 10.1063/5.0026839.

[99] K.-Q. Peng, X. Wang, L. Li, Y. Hu, and S.-T. Lee, "Silicon nanowires for advanced energy conversion and storage," *Nano Today*, vol. 8, no. 1, pp. 75–97, 2013.

[100] H. R. Heris, M. Kateb, S. I. Erlingsson, and A. Manolescu, "Thermoelectric properties of tubular nanowires in the presence of a transverse magnetic field," *Nanotechnology*, vol. 31, no. 42, p. 424 006, 2020.

[101] H. R. Heris, M. Kateb, S. I. Erlingsson, and A. Manolescu, "Effects of transverse geometry on the thermal conductivity of si and ge nanowires," *Surfaces and Interfaces*, p. 101 834, 2022.

[102] X. Zhou, J. Hu, C. Li, D. Ma, C. Lee, and S. Lee, "Silicon nanowires as chemical sensors," *Chemical Physics Letters*, vol. 369, no. 1-2, pp. 220–224, 2003.

[103] K.-Q. Peng, X. Wang, and S.-T. Lee, "Gas sensing properties of single crystalline porous silicon nanowires," *Applied Physics Letters*, vol. 95, no. 24, p. 243 112, 2009.

[104] O. N. Tufte, P. D. Chapman, and D. Long, "Silicon diffused-element piezoresistive diaphragms," *Journal of Applied Physics*, vol. 33, 1962.

[105] M. Tortonese, R. C. Barrett, and C. F. Quate, "Atomic resolution with an atomic force microscope using piezoresistive detection," *Applied Physics Letters*, vol. 62, p. 834, 1993.

[106] K. Wee, G. Kang, J. Park, *et al.*, "Novel electrical detection of label-free disease marker proteins using piezoresistive self-sensing micro-cantilevers," *Biosensors and Bioelectronics*, vol. 20, pp. 1932–1938, 2005.

[107]   M. L. Lee, E. A. Fitzgerald, M. T. Bulsara, M. T. Currie, and A. Lochtefeld, "Strained Si, SiGe, and Ge channels for high-mobility metal-oxide-semiconductor field-effect transistors," *Journal of Applied Physics*, vol. 97, no. 1, p. 011 101, Jan. 2005, Publisher: American Institute of Physics, ISSN: 0021-8979. DOI: 10. 1063/1.1819976.

[108]   W. Liu, M. Lee, L. Ding, J. Liu, and Z. L. Wang, "Piezopotential Gated Nanowire-Nanotube Hybrid Field-Effect Transistor," *Nano Letters*, vol. 10, no. 8, pp. 3084–3089, Aug. 2010, Publisher: American Chemical Society, ISSN: 1530-6984. DOI: 10.1021/nl1017145.

[109]   D. Gao, Z. Yang, L. Zheng, and Z. Kun, "Piezoresistive effect of n-type < 111 >-oriented si nanowires under large tension/compression," *Nanotechnology*, vol. 28, p. 095 702, 2017.

[110]   V. Schmidt, J. V. Wittemann, S. Senz, and U. Gösele, "Silicon nanowires: A review on aspects of their growth and their electrical properties," *Advanced Materials*, vol. 21, no. 25-26, pp. 2681–2702, 2009.

[111]   Z. Huang, N. Geyer, P. Werner, J. de Boor, and U. Gösele, "Metal-Assisted Chemical Etching of Silicon: A Review: In memory of Prof. Ulrich Gösele," en, *Advanced Materials*, vol. 23, no. 2, pp. 285–308, Jan. 2011, ISBN: 09359648, ISSN: 09359648. DOI: 10.1002/adma.201001784.

[112]   X. Li, "Metal assisted chemical etching for high aspect ratio nanostructures: A review of characteristics and applications in photovoltaics," en, *Current Opinion in Solid State and Materials Science*, vol. 16, no. 2, pp. 71–81, 2012, ISBN: 13590286, ISSN: 13590286. DOI: 10.1016/j.cossms.2011.11.002.

[113]   M. Hasan, M. F. Huq, and Z. H. Mahmood, "A review on electronic and optical properties of silicon nanowire and its different growth techniques," en, *SpringerPlus*, vol. 2, no. 1, p. 151, Dec. 2013, ISSN: 2193-1801. DOI: 10.1186/2193-1801-2-151.

[114]   H. Han, Z. Huang, and W. Lee, "Metal-assisted chemical etching of silicon and nanotechnology applications," en, *Nano Today*, vol. 9, no. 3, pp. 271–304, Jun. 2014, ISSN: 17480132. DOI: 10.1016/j.nantod.2014.04.013.

[115]   D. Shi, Y. Chen, Z. Li, *et al.*, "Anisotropic charge transport enabling high-throughput and high-aspect-ratio wet etching of silicon carbide," *Small Methods*, p. 2 200 329, 2022.

[116]   G. Svavarsson H, H. Hallgrimsson B, M. Niraula, J. Lee K, and R. Magnusson, "Large arrays of ultra-high aspect ratio periodic silicon nanowires obtained via top-down route," *Applied Physics A-Materials Science and Processing*, vol. 122, 2016.

[117]   E. Fakhri, M. Sultan, A. Manolescu, *et al.*, "Synthesis and photoluminescence study of silicon nanowires obtained by metal assisted chemical etching," in *2021 International Semiconductor Conference (CAS)*, IEEE, 2021, pp. 147–150.

[118]   D. Siingh, V. Pant, and A. K. Kamra, "Measurements of positive ions and airEarth current density at Maitri, Antarctica," en, *Journal of Geophysical Research: Atmospheres*, vol. 112, no. D13, 2006JD008101, Jul. 2007, ISSN: 0148-0227, 2156-2202. DOI: 10.1029/2006JD008101.

Appendix A

Code

The programming code designed and used.

A.1 Main data processing script

Listing A.1: The main Python script used to concentate all the simulation runs for data processing.

```
1  import numpy as np
   import pandas as pd
3  import Vacuum
   import glob
5  import os
   import f90nml
7  from scipy.constants import pi, e, hbar, m_e, epsilon_0

9  # Define external calculation parameters
   pulse_width_multiplier = 16 # Input pulse length multiplier (int)
11
   # Create Dataset for input variables and calculated outputs
13 Main_dataset = pd.DataFrame({ 'Voltage' : [],
                                 'Box_dim' : [],
15                               'Time_step' : [],
                                 'Emission_mode' : [],
17                               'Emitter_dim' : [],
                                 'Emitter_type' : [],
19                               'Amplitude' : [],
                                 'Pulse_width' : [],
```

```
21                                         'Laser_energy' : [],
                                           'Laser_var' : [],
23                                         'Pulse_center' : [],
                                           'Brightness' : [],
25                                         'Emittance_x' : [],
                                           'Emittance_y' : [],
27                                         'Pulse_ratio' : [],
                                           'Max_ramo' : [],
29                                         'Total_charge' : [],
                                           'Outpulse_start': [],
31                                         'Outpulse_end' : [], })

33    path = os.chdir(folderpath)

35    for filepath in glob.glob(folderpath + test_case):
          print(filepath)
37        # Load in Vacuum−MD input file
          input_file = f90nml.read(filepath + '/input')
39        # Aquire Input voltage from input file
          input_voltage = input_file['input']['v_s'] # Voltage (float)
41        box_dimensions = input_file['input']['box_dim'] # Dimensions of diode (list[↪
              ↪float, float, float])
          time_step = input_file['input']['time_step'] # Time step of simulation (float)
43        emission_mode = input_file['input']['emission_mode'] # Type of emission (↪
              ↪int)
          emitter_dim = input_file['input']['emitters_dim'] # Emitter dimentions (list[↪
              ↪float, float, float])
45        emitter_type = input_file['input']['emitters_type'] # Emitter type (int)

47        # Open the laser input input file (Photoemission specific)
          with open(filepath + '/laser') as laser_file:
49            array = [[float(x) for x in line.split()] for line in laser_file]
              #decision_operators = int(array[0][0]), int(array[0][1]), int(array[0][2]) ↪
                  ↪# Program load operators ([1, 1, 2])
51            laser_energy = array[1][0] # Energy of the laser in eV (float)
              laser_variation = array[2][0] # Variation of laser energy in eV (float)
53            pulse_center = int(array[3][0]) # Center of pulse in steps (int)
              pulse_width = int(array[4][0]) # Width of the pulse in steps (Gaussian) (↪
                  ↪int)
55            pulse_amplitude = array[5][0] # Amplitude of the pulse (float)

57        # Load absorbed electrons file
```

```
      filename_absorbed_top = os.path.join(filepath, 'out/absorbed_top.dt')
59    data = np.loadtxt(filename_absorbed_top) # Read absorbed at cathode file
      absor_elec = data[:, 3] # Data column for absorbed electrons at the cathode
61    tot_elec = 0 # Temp var for total electron count in system (float64)
      max_elec = 0 # Temp var. for e count to locate max (float64)
63
      # Count the absorbed electrons at cathode
65    for k in range(len(absor_elec)):
          tot_elec = tot_elec + absor_elec[k]
67    tot_charge = tot_elec * e
      # Check when cathode pulse starts (first electron exits)
69    for g in range(len(data[:, 2])):
          if (data[g, 2] != 0):
71            out_pulse_start = data[g, 0]
              break
73    # Check when cathode pulse ends (last electron exits)
      for k in range(len(absor_elec)):
75        max_elec = max_elec + absor_elec[k]
          if (tot_elec == max_elec):
77            out_pulse_end = data[k, 0]
              break
79
      # Calculate the length of the outgoing (cathode) pulse with regards to incoming↩
          ↪ (anode) pulse. (float64)
81    out_pulse_ratio = (out_pulse_end − out_pulse_start) / (pulse_width * ↩
          ↪pulse_width_multiplier)

83    # Load emitted electron file
      filename_emitted = os.path.join(filepath, 'out/emitted.dt')
85    data = np.loadtxt(filename_emitted) # Read emitted electrons file
      emitted_elec = data[:, 3] # Data column for emitted electrons at the anode
87    tot_elec = 0 # Temp var for total electron count in system (float64)
      max_elec = 0 # Temp var. for e count to locate max (float64)
89
      # Count the absorbed electrons at cathode
91    for k in range(len(emitted_elec)):
          tot_elec = tot_elec + emitted_elec[k]
93    tot_charge = tot_elec * e
      # Check when anode pulse starts (first electron emitted)
95    for g in range(len(data[:, 2])):
          if (data[g, 2] != 0):
97            in_pulse_start = data[g, 0]
```

```
                    break
99      # Check when anode pulse ends (last electron emitted)
        for k in range(len(emitted_elec)):
101         max_elec = max_elec + emitted_elec[k]
            if (tot_elec == max_elec):
103             in_pulse_end = data[k, 0]
                break

105


107     # Density file
        filename = os.path.join(filepath, 'out/density_absorb_top.bin')

109

        # Binary file layout
111     # float64 (double precision numbers)
        # int32 (32bit integers)
113     dt = np.dtype([('x' , np.float64), ('y', np.float64) , ('vx', np.float64), ('vy', np.←↩
            ↪float64),
                                    ('vz', np.float64), ('emit', np.int32), ('sec', np.int32) , ('←↩
                                        ↪nrID', np.int32)])
115     # Old version (missing nrID)
        dt_old = np.dtype([('x' , np.float64), ('y', np.float64) , ('vx', np.float64), ('vy', ←↩
            ↪np.float64),
117                                 ('vz', np.float64), ('emit', np.int32), ('sec', np.int32) ])


119     # Memory map the file
        # mode=r (Read only)
121     # order=F (Fortran style array)
        emittance = np.array([])
123     sigma_w = np.array([])
        sigma_wp = np.array([])
125     theta_ell = np.array([])
        #w_theta = np.array([0.00, 0.10, 0.20, 0.30, 0.40, 0.50])
127     try:
            data_mem = np.memmap(filename, dtype=dt, mode='r', order='F') # ←↩
                ↪Particle ID was added
129     except:
            data_mem = np.memmap(filename, dtype=dt_old, mode='r', order='F'←↩
                ↪) # Pre − 2022 version

131

        # Read the data into dataframe
133     df = pd.DataFrame.from_records(data=data_mem, columns=data_mem.←↩
            ↪dtype.names)
```

```
135     df['v'] = np.sqrt(df['vx']**2 + df['vy']**2 + df['vz']**2)

137     df["x'"] = (df['vx']/df['vz'])/1.0E−3
        df['x'] = df['x']
139
        df["y'"] = (df['vy']/df['vz'])/1.0E−3
141     df['y'] = df['y']

143     df["r"] = np.sqrt(df["x"]**2 + df["y"]**2)
        df["r'"] = (np.sqrt(df['vx']**2 + df['vy']**2) / df['vz']) / 1.0E−3
145
        e_x, sw, swp, th = Vacuum.Calc_Emittance(df, "x", "x'")
147     e_y, _, _, _ = Vacuum.Calc_Emittance(df, "y", "y'")

149     sigma_w = sw
        sigma_wp = swp
151     theta_ell = th

153     #print('Emittance in x−direction {:6.2f} nm−mrad'.format(e_x))
        #print('Emittance in y−direction {:6.2f} nm−mrad'.format(e_y))
155
        # Read data for current
157     filename_ramo = os.path.join(filepath, 'out/ramo_current.dt') # Ramo ↩
            ↪current
        # Read the data into dataframe
159     df_cur = pd.read_csv(filepath_or_buffer=filename_ramo, index_col=1, ↩
            ↪delim_whitespace=True, \
                            header=None, names=['time', 'step', 'current', 'volt', '↩
                                ↪nrPart', 'nrElec', 'nrHole', 'avg_mob', '↩
                                ↪avg_speed', 'ramo_1', 'ramo_2'])
161
        cur = df_cur['current'].max() # Find the max Ramo current
163
        # Calculate brightness
165     brightness = 2 * cur / (np.pi**2 * e_x * e_y * 1.0E−12)

167     # Write this simulation run into dataframe
        temp_set = pd.DataFrame({'Voltage' : [input_voltage],
169                                 'Box_dim' : [box_dimensions],
                                    'Time_step' : [time_step],
171                                 'Emission_mode' : [emission_mode],
```

```
           'Emitter_dim' : [emitter_dim],
173        'Emitter_type' : [emitter_type],
           'Pulse_width' : [pulse_width],
175        'Amplitude' : [pulse_amplitude],
           'Laser_energy' : [laser_energy],
177        'Laser_var' : [laser_variation],
           'Pulse_center' : [pulse_center],
179        'Brightness' : [brightness],
           'Emittance_x' : [e_x],
181        'Emittance_y' : [e_y],
           'Pulse_ratio' : [out_pulse_ratio],
183        'Max_ramo' : [cur],
           'Total_charge' : [tot_charge],
185        'Inpulse_start' : [in_pulse_start],
           'Inpulse_end' : [in_pulse_end],
187        'Outpulse_start': [out_pulse_start],
           'Outpulse_end' : [out_pulse_end],
189        })

191    # Write the simulation run into the Main dataset
       Main_dataset = pd.concat([temp_set, Main_dataset])
```

A.2   Emittance in vacuum

Listing A.2: Code from Kristinn Torfason used to calculate the emittance.

```
1  import numpy as np
2  import pandas as pd
   from scipy.constants import pi, m_e, hbar, e, epsilon_0

4
   # Calculates the emittance
6  # Input is a pandas dataframe that has columns called x and x'.
   # It returns the Emittance, sigma_w, sigma_wp and theta
8  # emittance [units of x * x'] [nm−mrad]
   # sigma_w is the semi−major axis of the ellipse [units of x]
10 # sigma_wp is the semi−minor axis of the ellipse [units of x']
   # theta is the rotation of the ellipse [deg]
12 # See http://uspas.fnal.gov/materials/10MIT/Emittance.pdf
   # or J. Buon, "Beam phase space and emittance".
14 # See also USPAS notes Barletta, Spentzouris, Harms
   # https://uspas.fnal.gov/materials/10MIT/MIT−Fund.shtml
```

```
16  # https://uspas.fnal.gov/materials/10MIT/Emittance.pdf
    def Calc_Emittance(df_emitt, x, xp):
18      sigma_x = df_emitt[x].std(ddof=0) # \sigma_x, ddof=0 means use N as ↩
            ↪normalization
        sigma_xp = df_emitt[xp].std(ddof=0) # \sigma_{x^\prime}
20      cov_xxp = df_emitt.cov()[x][xp] # \sigma_x\sigma_{x^\prime}
        N = df_emitt[x].count()
22      r = df_emitt.corr(method='pearson')[x][xp]

24      #emittance = sigma_x*sigma_xp*np.sqrt(1.0−r**2)
        emittance = np.sqrt(abs(sigma_x**2*sigma_xp**2 − cov_xxp**2))
26
        sigma_w = np.sqrt(abs( 0.5*(sigma_x**2 + sigma_xp**2 + np.sqrt( abs((↩
            ↪sigma_x**2 − sigma_xp**2)**2 + (2.0*cov_xxp)**2 ))) ))
28      sigma_wp = np.sqrt(abs( 0.5*(sigma_x**2 + sigma_xp**2 − np.sqrt(abs( (↩
            ↪sigma_x**2 − sigma_xp**2)**2 + (2.0*cov_xxp)**2 )) )))

30      theta = 0.5*np.arctan2(2.0*cov_xxp, (sigma_x**2 − sigma_xp**2)) # in rad
        theta = theta * 180/np.pi # Convert from rad to deg
32
        return emittance, sigma_w, sigma_wp, theta
```

A.3   Photoemission from a circle

Listing A.3: Photoemission from a circular emitter, this is just the circular emission code, small part of the total code base that is due to be published soon.

```
1
    subroutine Do_Photo_Emission_Circle(step, emit)
3       integer, intent(in) :: step, emit
        integer :: nrElecEmit, nrTry
5       double precision, dimension(1:3) :: par_pos, par_vel, field
        double precision :: r_e, r_e2, r2, p_eV
7
        ! Get Energy distribution of the photons
9       p_eV = ptr_Get_Photo_Emission_Energy()
        par_pos = 0.0d0
11      nrTry = 0
        nrElecEmit = 0
13      nrEmitted_emitters(emit) = 0
```

```fortran
15      do while (nrTry <= MAX_EMISSION_TRY)
           ! Check if we have reached the max number of electrons to be emitted,
17         ! if we are using Gaussian limited emission.
           if ((nrElecEmit >= maxElecEmit) .and. (EmitGauss .eqv. .True.)) then
19            exit
           end if

21
           ! Check if we have reached the maximum number of electrons.
23         ! If this happends then the parameter MAX_PARTICLES (in mod_gobal)
           ! needs to be increased and the code recompiled.
25         if (nrElec == MAX_PARTICLES−1) then
              print *, 'WARNING:_Reached_maximum_number_of_electrons!!!'
27            exit
           end if

29
           ! Find a random spot on the cathode.
31         r_e = emitters_dim(1, emit) ! Radius of emitter
           r_e2 = r_e**2 ! Radius of emitter squared
33         r2 = r_e2 + 1.0d0 ! Must be larger then r_e2 for the do while loop to run
           do while (r2 > r_e2)
35            call random_number(par_pos(1:2)) ! Gives a random number [0,1]

37            par_pos(1:2) = 2.0d0*(par_pos(1:2) − 0.5d0)*r_e ! Range is −r_e to +↩
                 ↪r_e
              r2 = par_pos(1)**2 + par_pos(2)**2 ! Radius squared of our random ↩
                 ↪point
39         end do

41         nrTry = nrTry + 1 ! Add one more try
           par_pos(3) = 0.0d0 * length_scale ! Check in plane

43

45         if (w_theta_xy(par_pos, emit) <= p_eV) then

47            field = Calc_Field_at(par_pos)
              if (field(3) < 0.0d0) then
49               par_pos(3) = 1.0d0 * length_scale ! Above plane
                 field = Calc_Field_at(par_pos)

51
                 if (field(3) < 0.0d0) then
53                  par_pos(3) = 1.0d0 * length_scale ! Place above plane
```

```fortran
55          if (PHOTON_MODE == 1) then
               par_vel = 0.0d0
57          else if (PHOTON_MODE == 2) then
               par_vel(3) = sqrt((2 * ((p_eV − w_theta_xy(par_pos, emit))*↩
                  ↪q_0))/m_0) ! <−− Newtonian
59          else
               print *, "WARNING:_Unknown_photon_velocity_mode!"
61          end if

63          call Add_Particle(par_pos, par_vel, species_elec, step, emit, −1)

65          nrElecEmit = nrElecEmit + 1
            nrEmitted_emitters(emit) = nrEmitted_emitters(emit) + 1
67          nrTry = 0
          end if
69      end if
      end if

71
    end do

73
    posInit = posInit + nrElecEmit
75  nrEmitted = nrEmitted + nrElecEmit
  end subroutine Do_Photo_Emission_Circle
```

A.4   Gaussian distribution

Listing A.4: Gaussian distribution of the emission that is the input for the random Poisson distribution, the lambda A.7.

```fortran
1  double precision function Gauss_Emission(step)
2      integer, intent(in) :: step ! Current time step
      integer :: IFAIL
4      double precision :: b, c

6      b = 1.0d0 / ( 2.0d0 * pi * Gauss_pulse_width**2 )
      c = −1.0d0 * b * (step − Gauss_pulse_center)**2
8
      if (c < −500) then
10         Gauss_Emission = 0.0d0
      else
12         Gauss_Emission = Gauss_pulse_amplitude * exp(c)
```

```
        end if
14
        write (ud_gauss, "(i6,_tr2,_i6)", iostat=IFAIL) step, Gauss_Emission
16 end function Gauss_Emission
```

A.5   Incoming photon energy distribution

Listing A.5: Incoming photon energy is given a normal distribution with Box-Muller method A.6.

```fortran
1  ! Repurposed Maxwell−Boltzmann distribution for velocity generation
2  ! https://en.wikipedia.org/wiki/Maxwell%E2%80%93Boltzmann_distribution#↩
        ↪Distribution_for_the_velocity_vector
   !
4  ! Box−Muller method for normal distribution of photon energies
   ! Input is read from laser file with mean and standard deviation (std) in ↩
        ↪electronVolts (eV)
6  function Get_Laser_Energy()
      double precision :: Get_Laser_Energy
8     double precision, dimension(1:2) :: std
      double precision, dimension(1:2) :: mean
10    double precision, dimension(1:3) :: Set_Laser_Energy

12    mean = laser_energy
      std = laser_variation ! Standard deviation of the Maxwell−Boltzmann ↩
          ↪distribution
14
      ! Get normal distributed numbers.
16    ! The Box Muller method gives two numbers.
      ! We overwrite the second element in the array.
18    Set_Laser_Energy(1:2) = box_muller(mean, std)
      Set_Laser_Energy(2:3) = box_muller(mean, std)
20
      Get_Laser_Energy = abs(Set_Laser_Energy(3)) ! Positive velocity in the z−↩
          ↪direction
22 end function Get_Laser_Energy
```

A.6   Box-Muller method for normal distribution

Listing A.6: Box Muller method for normal distribution.

```
1  function box_muller(mean, std)
2     double precision, dimension(1:2) :: box_muller
      double precision, dimension(1:2), intent(in) :: mean, std
4     double precision :: w
      double precision, dimension(1:2) :: x, y

6
      do
8        call random_number(x)

10       x = 2.0d0∗x − 1.0d0
         w = x(1)∗∗2 + x(2)∗∗2
12
         if (w < 1.0d0) exit
14    end do

16    y = x∗sqrt( (−2.0d0 ∗ log( w ) ) / w )
      box_muller = y∗std + mean
18 end function box_muller
```

A.7 Random Poisson distribution

Listing A.7: Random Poisson distribution with mean lambda, Junhao, based on Knuth.

```
1  ! Random poission variable with mean lambda.
2  ! See
   ! https://en.wikipedia.org/wiki/Poisson_distribution#Generating_Poisson−↩
       ↪distributed_random_variables
4  ! From Wikipedia
   ! algorithm poisson random number (Junhao, based on Knuth):
6  integer function Rand_Poission(lambda)
      double precision, intent(in) :: lambda
8     double precision :: lambda_left, p, u
      integer :: k
10    double precision, parameter :: Poisson_Step = 500.0d0

12    lambda_left = lambda
      k = 0
14    p = 1.0d0
```

```fortran
16      do while (p >= 1.0d0)
           k = k + 1
18         call random_number(u)
           p = p*u
20         do while ((p < 1.0d0) .and. (lambda_left > 0.0d0))
              if (lambda_left > Poisson_Step) then
22               p = p * exp(Poisson_Step)
                 lambda_left = lambda_left − Poisson_Step
24            else
                 p = p * exp(lambda_left)
26               lambda_left = 0.0d0
              end if
28         end do
        end do
30
        Rand_Poission = k − 1
32  end function Rand_Poission
```